

# Lawrence Berkeley National Laboratory

## Recent Work

**Title**

SOOT AND RADIATION IN COMBUSTING BOUNDARY LAYERS

**Permalink**

<https://escholarship.org/uc/item/9cp2z1f4>

**Author**

Beier, R.A.

**Publication Date**

1981-12-01



# Lawrence Berkeley Laboratory

UNIVERSITY OF CALIFORNIA

## ENERGY & ENVIRONMENT DIVISION

RECEIVED  
LAWRENCE  
BERKELEY LABORATORY  
MAR 29 1982  
LIBRARY AND  
DOCUMENTS SECTION

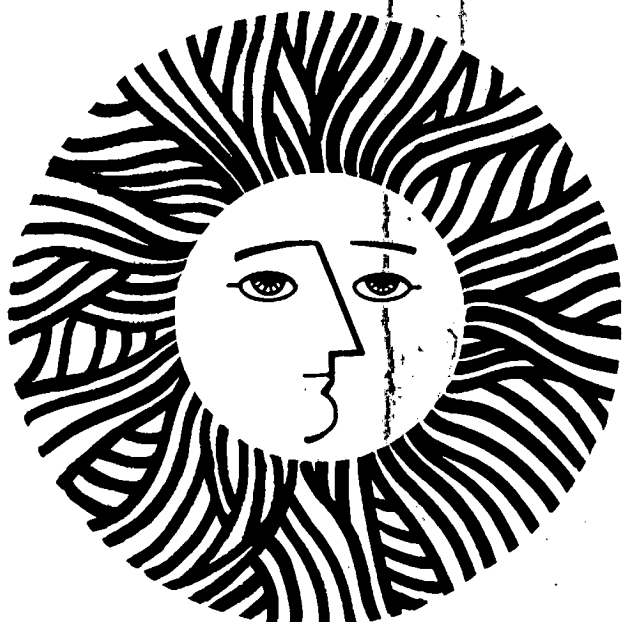
SOOT AND RADIATION IN COMBUSTING BOUNDARY LAYERS

Richard Alan Beier  
(Ph.D. thesis)

December 1981

**TWO-WEEK LOAN COPY**

*This is a Library Circulating Copy  
which may be borrowed for two weeks.  
For a personal retention copy, call  
Tech. Info. Division, Ext. 6782*



LBL-14011  
c.2

## DISCLAIMER

This document was prepared as an account of work sponsored by the United States Government. While this document is believed to contain correct information, neither the United States Government nor any agency thereof, nor the Regents of the University of California, nor any of their employees, makes any warranty, express or implied, or assumes any legal responsibility for the accuracy, completeness, or usefulness of any information, apparatus, product, or process disclosed, or represents that its use would not infringe privately owned rights. Reference herein to any specific commercial product, process, or service by its trade name, trademark, manufacturer, or otherwise, does not necessarily constitute or imply its endorsement, recommendation, or favoring by the United States Government or any agency thereof, or the Regents of the University of California. The views and opinions of authors expressed herein do not necessarily state or reflect those of the United States Government or any agency thereof or the Regents of the University of California.

SOOT AND RADIATION  
IN COMBUSTING BOUNDARY LAYERS

Richard Alan Beier

Ph.D. Thesis

December 1981

Energy and Environment Division  
Lawrence Berkeley Laboratory  
University of California  
Berkeley, CA 94720

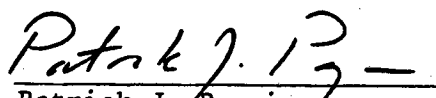
This work was supported by the U.S. Department of Energy under Contract No. W-7405-ENG-48 at the Lawrence Berkeley Laboratory of the University of California; and by the Center for Fire Research in the U.S.D.O.C. National Bureau of Standards under Grant No. NB 80-NAG-E6839.

# SOOT AND RADIATION IN COMBUSTING BOUNDARY LAYERS

Richard Alan Beier

Ph.D.

Mechanical Engineering

  
Patrick J. Pagni  
Chairman of Committee

## ABSTRACT

In most fires thermal radiation is the dominant mode of heat transfer. Carbon particles within the fire are responsible for most of this emitted radiation and hence warrant quantification. As a first step toward understanding thermal radiation in full scale fires, an experimental and theoretical study is presented for a laminar combustng boundary layer. Carbon particulate volume fraction profiles and approximate particle size distributions are experimentally determined in both free and forced flow for several hydrocarbon fuels and PMMA (polymethylmethacrylate). A multiwavelength laser transmission technique determines a most probable radius and a total particle concentration which are two unknown parameters in an assumed Gauss size distribution. A sooting region is observed on the fuel rich side of the main reaction zone. For free flow, all the flames are in air, but the free stream ambient oxygen mass fraction is a variable in forced flow. To study the effects of radiation heat transfer, a model is developed for a laminar

combusting boundary layer over a pyrolyzing fuel surface. An optically thin approximation simplifies the calculation of the radiant energy flux at the fuel surface.

For the free flames in air, the liquid fuel soot volume fractions,  $f_v$ , range from  $f_v \sim 10^{-7}$  for n-heptane, a paraffin, to  $f_v \sim 10^{-7}$  for toluene, an aromatic. The PMMA soot volume fractions,  $f_v \sim 5 \times 10^{-7}$ , are approximately the same as the values previously reported for pool fires. Soot volume fraction increases monotonically with ambient oxygen mass fraction,  $Y_{Ox,\infty}$  in the forced flow flames. For n-heptane and PMMA soot volume fractions increase to  $f_v \sim 5 \times 10^{-6}$  at  $Y_{Ox,\infty} = 0.50$ . For all fuels tested, a most probable radius between 20 nm and 80 nm is obtained which varies only slightly with oxygen mass fraction, streamwise position, or distance normal to the fuel surface.

The theoretical analysis yields nine dimensionless parameters, which control the mass flux rate at the pyrolyzing fuel surface. A comparison between theoretical and experimental mass pyrolysis rates shows good agreement for PMMA.

## ACKNOWLEDGEMENTS

I am indebted to Professor Patrick J. Pagni for his continuous support and guidance throughout my research program. Thanks are due to the other members of my thesis committee, Professors Ralph Greif and Robert B. Williamson, for reviewing this work.

The technical staff of Hesse Hall and the machine shop in the Mechanical Engineering Department provided assistance for the experimental work. I am grateful for the many discussions with other graduate students, especially Steven Bard, Charles Kinoshita, Clement Okoh, Chien-Pei Mao, Gary Hubbard, and David Lee.

My parents provided continuous support and understanding throughout my years at school.

I thank my wife, Carol, for her understanding, patience, and care. Her encouragement and friendship provide a stable support on which I depend. She shares in the successful completion of this work.

This work was supported by the U.S. Department of Energy under Contract No. W-7405-ENG-48 at the Lawrence Berkeley Laboratory of the University of California; and by the Center for Fire Research in the U.S.D.O.C. National Bureau of Standards under Grant No. NB 80-NAG-E6839.

## TABLE OF CONTENTS

	ACKNOWLEDGEMENTS.....	iii
	TABLE OF CONTENTS.....	v
	NOMENCLATURE.....	vii
CHAPTER 1	INTRODUCTION.....	1
CHAPTER 2	SOOT VOLUME FRACTIONS IN FREE FLOW.....	6
	2.1 Introduction.....	6
	2.2 Extinction Analysis.....	6
	2.3 Experimental Method.....	8
	2.4 Results and Discussion.....	15
	2.5 Conclusions.....	26
CHAPTER 3	SOOT VOLUME FRACTIONS IN FORCED FLOW.....	28
	3.1 Introduction.....	28
	3.2 Experimental Method.....	28
	3.3 Results and Discussion.....	35
	3.4 Conclusions.....	45
CHAPTER 4	BOUNDARY LAYER MODEL WITH RADIATION.....	48
	4.1 Introduction.....	48
	4.2 Forced Flow Combustion.....	49
	4.2.1 Analysis.....	49
	4.2.2 Results and Discussion.....	55
	4.3 Free Flow Combustion.....	64
	4.3.1 Analysis.....	64
	4.3.2 Results and Discussion.....	67
	4.4 Comparison With Experiment.....	70
	4.4.1 Evaluation of Absorption Coefficient..	70



4.4.2	Pyrolysis Rates.....	73
4.5	Conclusions.....	76
CHAPTER 5	CONCLUSIONS.....	79
5.1	Summary of Results.....	79
5.2	Future Work.....	80
REFERENCES	.....	82
APPENDIX A	EXTINCTION EFFICIENCY.....	88
APPENDIX B	ERROR ANALYSIS.....	94
APPENDIX C	FUEL PROPERTIES.....	96
FIGURE CAPTIONS	.....	98

## NOMENCLATURE

$B$	mass transfer number, $(Q_p Y_{p,ox,\infty} - h_w)/L_p$
$B_w$	radiosity at fuel surface
$B$	radiosity at boundary layer edge
$c_p$	mixture specific heat
$D$	diffusion coefficient
$D_c$	dimensionless heat of combustion, $Q_p Y_{p,ox,\infty}/h_w$
$e_b$	black body emissive power
$E_n(\tau)$	$n$ th exponential integral
$f$	similarity stream function in boundary layer
$f_v$	particulate carbon volume/flame volume
$g$	gravitational acceleration
$Gr_x$	Grashof number, $g(T_w - T_\infty)x^3/\nu_\infty^2 T_\infty$
$h$	enthalpy
$\Delta H_c$	heat of reaction per gm of fuel
$\Delta H_{vap}$	latent heat of vaporization
$I$	radiant intensity
$k$	thermal conductivity
$L$	beam pathlength through fire
$L_p$	effective latent heat of pyrolysis
$m$	complex index of refraction
$m_p$	local mass flux
$\dot{M}_i$	molecular weight of species $i$
$\dot{M}_p(x)$	total mass flux
$\dot{m}'''$	volumetric mass generation rate
$n$	real index of refraction

$nk$  imaginary index of refraction  
 $N_0$  total particle concentration  
 $N_R$  radiation parameter,  $k \kappa / \sigma T_\infty^3$   
 $N(r)dr$  particle concentration in the size range  $dr$  about  $r$   
 $Pr$  Prandtl number,  $\nu/\alpha$   
 $\dot{q}'''$  volumetric heat generation rate  
 $q_R$  radiation flux  
 $Q$  extinction efficiency  
 $Q_p$  heat of reaction per gm of oxygen  
 $Q_R$  dimensionless radiation flux,  $q_R / T^4$   
 $r$  particle radius  
 $r_p$  mass consumption number,  $Y_{ox,\infty} \nu_f M_f / Y_{fwr} \nu_{ox} M_{ox}$   
 $Re_x$  Reynolds number,  $u_\infty x / \nu_\infty$   
 $T$  temperature  
 $u$  x-direction velocity  
 $v$  y-direction velocity  
 $x$  streamwise direction coordinate  
 $y$  transverse direction coordinate  
 $Y_i$  mass fraction of species  $i$

Greek

$\epsilon$  emissivity  
 $\eta$  transformed normal coordinate  
 $\theta$  dimensionless temperature,  $T/T_\infty$   
 $\kappa$  absorption coefficient

$\lambda$	wavelength
$\mu$	viscosity
$\nu$	stoichiometric coefficient or kinematic viscosity
$\xi$	transformed streamwise coordinate
$\rho$	density
$\sigma$	Stefan-Boltzmann constant or standard deviation
$\tau$	optical thickness, $\kappa y$
$\psi$	stream function

#### Subscripts

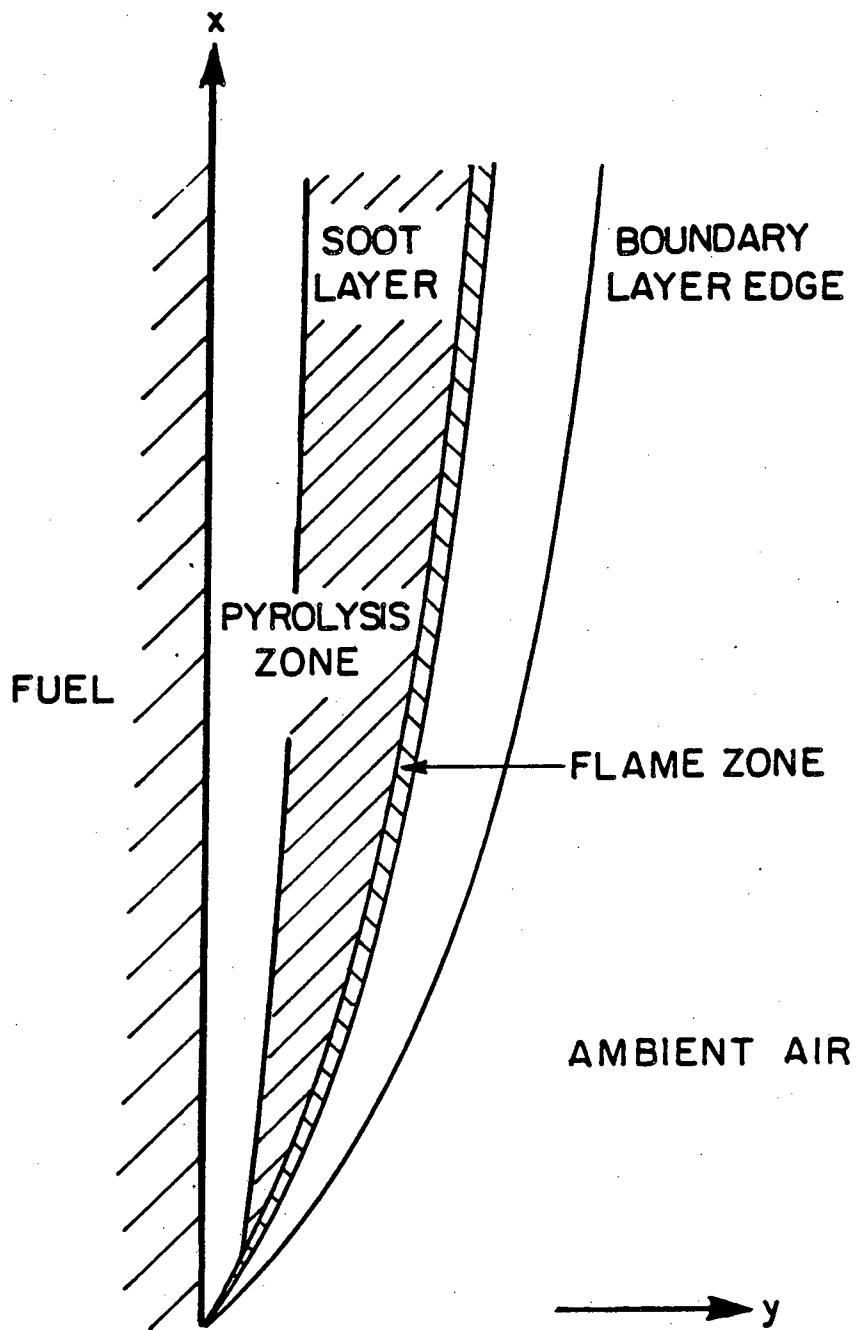
bl	boundary layer
e	excess
ex	external
f	fuel
fl	flame
ft	fuel in the transferred (pyrolyzed) material
i	first wavelength
j	second wavelength
l	liquid phase
m	mean
max	most probable, i.e. at maximum in $N(r)$
o	incident
ox	oxygen
p	pyrolyzed
w	fuel surface

## Chapter 1: INTRODUCTION

Thermal radiation is the dominant mode of heat transfer in full scale fires, where carbon particles within the flame are responsible for most of the emitted radiation. Experimental studies of soot in fires may provide insights to the complex processes of soot formation and oxidation. A steady, two dimensional, laminar, combusting boundary layer is attractive for a study of flame soot, because the fire can be easily probed by optical techniques and predicted by mathematical models. This work is an experimental and theoretical study of thermal radiation in combusting boundary layers for both free and forced flow. A multiwavelength laser transmission technique is used to determine volume fraction of soot and approximate size distributions. A model is developed for a combusting boundary layer with radiation, where measured values of soot volume fraction are used.

A schematic diagram of a combusting boundary layer is shown in Fig. 1-1. Since the main oxidation reactions are very fast relative to molecular diffusion rates of species and heat, oxidation of the fuel takes place in a narrow flame zone. Combustible gases, which are released at the fuel surface, pyrolyze as they approach the flame zone. Part of the carbon in the fuel is converted to carbon particulates, which are observed on the fuel rich side of the flame zone.

Minchin [1] and Clarke, Hunter, and Garner [2] did early studies of the effect of fuel type on soot formation in laminar diffusion flames. They increased the height of a flame on a small, circular



XBL 813-5397

Fig. 1-1

burner by increasing the fuel flow rate until the flame emitted soot at its tip. This height is called the smoke height or sooting height. For comparing different fuels, a lower sooting height indicates a greater amount of soot formation.

More recently, various experimental techniques have been used to study soot formation in flames. Glassman and Yaccarino [3,4] measured sooting heights to determine the effects of oxygen concentrations and temperature on sooting tendency. Kadota, Hiroyasu, and Farazandehmehr [5], and Chakraborty and Long [6,7] collected soot escaping from the combustion zone. Using probes to collect particles, Jagoda, Prado, and Lahaye [8] examined the soot under an electron microscope to find clusters or chain-like structures. Whether clusters of particles exist in the fire, or small particles form chains during the sampling process is not known. Unlike probe techniques, optical measurements do not disturb the system under study. D'Alessio et al [9,10] combined light scattering and extinction measurements to yield particle size and concentrations. Related experiments have been reported by Kent, Jander, and Wagner [11], Haynes, Jander, and Wagner [12,13], and Chang and Penner [14]. Since transmission measurements are easier to perform than scattering techniques, Pagni and Bard [15-19] developed a multiwavelength laser transmission technique, where the effects of particle nonsphericity on the transmitted intensity are less than the effects on scattering measurements [20].

Both premixed and diffusion flames have been studied in previous investigations of soot formation. Diffusion flames give more soot than premixed flames, because pyrolysis of the fuel and soot formation

reactions take place in a fuel-rich zone. In premixed flames, pyrolysis and soot formation reactions occur simultaneously with oxidation reactions. Rapid oxidation of the fuel in premixed flames may prevent formation of soot precursors or promote oxidation of precursors. Explanations of possible soot formation processes were reviewed by Palmer and Cullis [21], Wagner [22], and Bittner and Howard [23].

Previous measurements in pool fires by Bard and Pagni [17-19] determined an average soot volume fraction along a line of sight. Using a modified Schmidt Method technique, Markstein [24], and Santo and Tamanini [25] determined absorption-emission coefficients and volume fraction of soot in pool fires of PMMA. The spatial integration across the pool fire does not give detailed information about the structure of the sooting region. The present study determines the detailed structure of a soot layer in a combusting boundary layer.

The theoretical part of this report extends the work of previous studies, which neglect radiation in combusting boundary layers [26-32]. Many authors [33-39] have discussed the interaction of convection and radiation in an inert boundary layer. Tamamini [40] included radiation in his model of vertical wall fires, but he emphasized the modeling of turbulence. Kinoshita and Pagni [41] obtained a similarity solution for an opposed flow diffusion flame with radiation. Sibulkin, Kulkarni, and Annamalai [42] included radiation in their model of a burning vertical surface, but their approximation of local similarity is unnecessary. Han [43] obtained a



numerical solution for a forced flow radiative boundary layer by modifying the GENMIX computer code. Liu and Shih [44] added radiation to an analysis of boundary layer combustion, but their assumption of a constant mass fraction of fuel at the surface is not needed. Recently, Tien and Lee [45], and de Ris [46] reviewed previous work on thermal radiation from flames.

In the present study, the volume fraction and size of soot is determined by laser transmission measurements. Profiles at different streamwise positions are obtained in a combusting boundary layer for five liquid fuels and one solid fuel. In free flow, all the fires are burned in ambient air. For forced flow the experiments are performed in a small wind tunnel designed to produce a uniform flow of an oxidizing mixture of nitrogen and oxygen. The oxygen mass fraction is changed in the wind tunnel to study the dependence of soot volume and size on oxygen mass fraction.

A model is developed for a laminar combusting boundary layer with radiation. The analysis yields dimensionless groups, which measure the importance of thermal radiation. A comparison between theoretical pyrolysis rates and experimental values for PMMA gives good agreement.

## Chapter 2: SOOT VOLUME FRACTIONS IN FREE FLOW

### 2.1 Introduction

Since a small, burning, vertical wall provides a two dimensional combusting boundary layer, which has been previously modeled [26-32], this fire is chosen for a study of flame soot. In Fig. 1-1, a schematic diagram of a combusting boundary layer is shown. A layer on the fuel rich side of the blue flame zone is yellow, which indicates the presence of carbon particles. The width of the yellow soot layer increases with height. A multiwavelength laser transmission technique [15-19] is used to determine the detailed structure of the soot layer. The measurements specify soot volume fractions and approximate size distributions at different locations within the combusting boundary layer for five liquid fuels and one solid fuel.

### 2.2 Extinction Analysis

The multiwavelength laser transmission technique is based on the following extinction analysis. The transmitted intensity,  $I$ , of a monochromatic beam through a polydisperse aerosol is related to the initial intensity,  $I_0$  by

$$I(\lambda)/I_0(\lambda) = \exp(-\tau(\lambda)L) \quad (2-1)$$

where  $L$  is the beam pathlength. An aerosol spectral extinction coefficient,  $\tau$ , is given by

$$\tau(\lambda, m, r) = \int_0^{\infty} N(r)Q(\lambda, m, r)\pi r^2 dr \quad (2-2)$$

where  $Q$  is the particle extinction efficiency from the Mie scattering

theory [47] for spherical particles. Expressions for the extinction efficiency are given in Appendix A. Calculation of a spectral extinction coefficient requires knowledge of the optical properties of soot,  $m=n(1-ik)$ , and the size distribution,  $N(r)$ . The values of the optical properties which were derived by Lee and Tien [48] and listed by Bard and Pagni [18] are used. A Gauss size distribution with  $\sigma/r_m = 1/2$ ,

$$N(r)/N_o = (27r^3/2r_{max}^4) \exp(-3r/r_{max}) \quad (2-3)$$

is assumed, where  $r_{max}$  is the most probable radius, and  $N_o$  is the total particle concentration. The volume fraction of soot is defined by

$$f_v \equiv \frac{4}{3}\pi \int_0^\infty N(r)r^3 dr \quad (2-4)$$

which, with equation (2-3), gives

$$f_v = \frac{54\pi}{3^8} \Gamma(7) N_o r_{max}^3 = 18.62 N_o r_{max}^3 \quad (2-5)$$

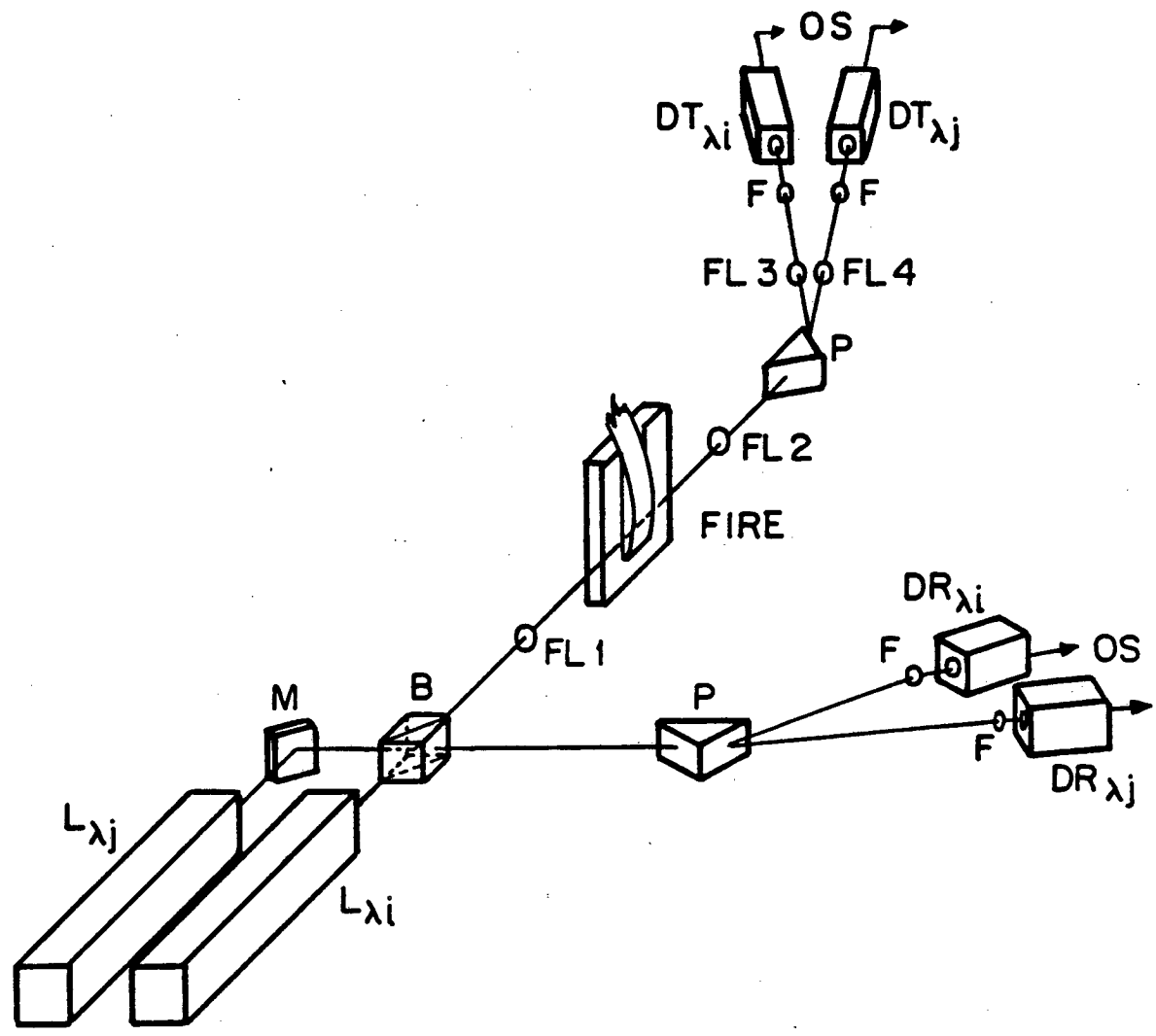
Measurements are made of the ratio of the transmitted and initial intensities,  $I/I_o$ , at two different wavelengths, superimposed over the same pathlength,  $L$ . Substituting these measured values into equation (2-1) gives two independent values of  $\tau$ , one at each wavelength. These two  $\tau$  values give two independent equations (2-2) to determine the two unknowns in the size distribution,  $N_o$  and  $r_{max}$  [15,17,18]. Details of these calculations to determine  $N_o$  and  $r_{max}$  are given in Appendix A. The volume fraction of soot is obtained from equation (2-5).

Since soot particles may agglomerate into larger clusters, Lee and Tien [49] studied how different shapes affect the radiative characteristics of a medium. With long chains approximated as cyclinders, they considered spherical and cylindrical particles as two limiting cases. From their calculations, particle shape is most important in the far infrared region. For the visible wavelengths of these transmission measurements and the near infrared region of most flame radiation, calculations based on spherical particles give satisfactory results.

Light extinction in the fire is attributed entirely to soot particles, but some absorption by gas phase species has been demonstrated in previous studies [13,50-52]. Recent fluorescence measurements by Bard and Pagni [16] indicate the gas-phase species absorb less than 1% of the incident laser power in laser transmission experiments for pool fires. In the present study, good agreement among results for different wavelength pairs indicate the gas-phase absorption is negligible in the soot layer. A weaker absorption not due to soot is found in a relatively cool, unburned region between the fuel surface and the soot layer. The extinction analysis in this region yields results which are inconsistent with the possible theoretical values of the extinction coefficient ratio listed in Appendix A for the optical properties of soot.

### 2.3 Experimental Method

The experimental setup, which is shown in Fig. 2-1, is similar to that described by Pagni and Bard [15,17-19]. Two lasers are used: a Spectra-Physics Argon Ion tunable laser model 165, operating at either



XBL813-5398

Fig. 2-1

$\lambda = 0.4579 \text{ um}$ ,  $0.4880 \text{ um}$ , or  $0.5145 \text{ um}$ , and a Spectra-Physics Helium Neon laser model 125, emitting at  $\lambda = 0.6328 \text{ um}$ . After a cube beam splitter superimposes the two beams from the lasers, the beams pass through the same physical space in the fire. A first simple lens reduces the diameter of the beams in the fire. After a second lens collects the transmitted light, an equilateral prism separates the two beams. Each beam passes through another focusing lens and a narrow band pass filter, before it strikes a laser power meter (Newport Research Corp., model 820). The beam splitter provides a second beam from each laser, which is monitored as a reference intensity by the same prism-detector system. A PDP-11/34 microcomputer stores the data, after the output signals from the detectors pass through a d.c. amplifier and a (Digital Equipment Corp.) AR11 16-channel, 10 bit, A/D converter. A digital timer, with an adjustable period, triggers the A/D converter to read the output signals of the detectors.

The liquid fuels and one solid fuel, PMMA (polymethylmethacrylate), are mounted in a small, vertical wall, which is bolted to a movable table. The inert wall is made of Marinite-XL (Johns-Manville Co.), and its width and height are 0.5 m. The wick, ceramic fiber board (Fiberfrax Hot Board, Carborundum Co.), has its front surface flush with the inert wall surface. With aluminum foil around the hidden surfaces of the wick, the inert wall does not absorb the liquid fuel.

Since the transmission of the laser beams varies greatly for the different fuels, wicks of different widths are used as listed in Table 2-1. The wicks are usually 15 cm or 7 cm wide, and they are 12 cm

Table 2-1. Summary of Peak Soot Volume Fractions and Size Distributions at  $x = 4$  cm.

Fuel	Sample Width (cm)	Wave-length Pair, i-j	Path-length L (cm)	Distance from Fuel Surface (mm)	$(I/I_o)_i$	$(I/I_o)_j$	$f_v \times 10^{-6}$	$r_{max}$ (nm)	$N_o \times 10^{-9}$ ( $cm^{-3}$ )
<u>Liquids</u>									
Toluene ( $C_7H_8$ )	3	1-4	3.3	3.2	0.0043	0.028	10	44	6.3
	3	2-4	3.2	3.5	0.0012	0.0096	13	45	7.2
Cyclohexene ( $C_6H_{10}$ )	7	1-4	8.2	4.6	0.039	0.17	2.1	32	3.5
	7	2-4	8.2	4.4	0.10	0.25	1.9	31	3.5
Iso-octane ( $C_8H_{18}$ )	3	1-4	3.7	4.8	0.52	0.69	1.0	36	1.2
	7	1-4	7.7	4.8	0.21	0.46	1.3	25	4.5
	15	1-4	16.0	4.8	0.063	0.24	1.1	27	3.0
	15	2-4	16.0	4.5	0.088	0.23	1.0	31	1.8
	15	3-4	16.0	4.8	0.11	0.23	1.1	27	3.0
Cyclohexane ( $C_6H_{12}$ )	7	1-4	7.9	4.1	0.37	0.58	0.70	33	1.1
	15	1-4	16.1	4.1	0.15	0.35	0.67	32	1.1
n-Heptane ( $C_7H_{16}$ )	7	1-4	8.3	4.0	0.54	0.73	0.43	28	1.0
	15	1-4	16.2	4.4	0.27	0.51	0.49	27	1.3
	15	2-4	16.2	4.6	0.39	0.55	0.36	35	0.46
<u>Solid</u>									
Polymethyl-methacrylate ( $C_5H_8O_2$ ) <sub>n</sub>	16	1-4	15.8	2.3	0.38	0.63	0.39	23	1.7

high, except those used for toluene are 6 cm high. The samples of PMMA are 15 cm high, 16 cm wide, and 1.27 cm thick. The diameter of the laser beam in the flame limits the spatial resolution of the transmission measurement. For pathlengths of 16 cm and 7 cm the maximum beam width between points of  $1/e^2$  intensity is less than 0.4 mm and 0.3 mm, respectively.

Since variations in temperature and species change the index of refraction in the direction normal to the fuel surface, the fire deflects the laser beam. The angular deflection of the beam in the combustng boundary layer is greater than the deflection from pool fires [15-19], due to the steeper gradients of the species and temperature profiles in the boundary layer. This angular deflection can change the physical pathlength of the beams through the prism and cause the beams to miss the detectors. Lens FL2 in Fig. 2-1 is used to minimize the beam movement relative to the prism and the detectors. The position of lens FL2 bisects the distance between the prism and the center of the fire, which is set at four times the focal length of lens FL2. This arrangement projects an image of the beam at the center of the fire onto the prism. Since the linear displacement of the beam is small at the center of the fire, the movement of the beam is small at the prism.

The deflection of the beam in the fire is measured for all the fuels. For liquid fuels the deflection does not decrease the spatial resolution significantly except near the inner edge of the soot layer when the width of the wick is 15 cm. Therefore, data near the inner boundary of the soot layer are obtained from measurements with shorter



pathlengths. Since the deflection of the beam is less for PMMA, a larger pathlength of 16 cm is used.

The distance between the superimposed laser beams and the fuel surface is changed by moving the fire horizontally. A complete scan of the fire is obtained by adjusting the height of the wall between traverses. After the fuel is ignited, a sheet of pyrex glass is placed in front of the fire about 0.25 m from the fuel surface to block disturbances from air movements in the room. For liquid fuels the supply of fuel in the wick gives a steady flame for about five minutes after a very short transient period. This steady period allows one horizontal scan, with increments of 0.4 mm, through the boundary layer each time the fire is ignited. At each position the outputs of the detectors are read 300 times within a 6 second interval. After each horizontal scan the fire is extinguished, the height of the wall is changed, and the wick is soaked with fuel before the fire is reignited.

For the liquid fuels the pathlength,  $L$ , is approximately 1 cm longer than the wick width. For PMMA beam pathlength is slightly less than the sample width, because near the sample edges the flame follows the round edges of the sample. The pathlength is measured by placing a scale directly in front of the flame at the laser beam location. End effects may be neglected for these large  $L$ . The measured values of  $I/I_0$  for the two different wavelengths and  $L$  are used in the extinction analysis to calculate  $r_{\max}$  and  $f_v$ . Data for more than one wavelength pair may be necessary to isolate the correct value of  $r_{\max}$  [15-19].

For PMMA the fuel regression rate affects the beam distance from the fuel surface. The regression rate is measured by blocking the laser beams partially with the fuel surface. If the vertical wall remains stationary, the surface of the pyrolyzing fuel slab moves and blocks a smaller part of the laser beams. The regression rate is the rate the vertical wall is moved to maintain a constant reading of transmitted intensity for the partially blocked beam. The regression rate is measured before and after each horizontal scan through the boundary layer. A new sample of PMMA is burned for the transmission measurements at each height.

Due to some unsteadiness in the fire, the positions of the soot layer and the flame zone fluctuate. Near the boundaries of the soot zone, a point at a fixed distance from the fuel surface spends only part of the time in the soot layer. Likewise, only a part of the pathlength of the laser beam through the fire may be in the soot layer at any time. Since the measured pathlength is the entire width of the fire, transmission measurements near a boundary may give too high a value of  $I/I_0$ , and therefore, a lower volume fraction of soot than the true value. At the outer soot layer boundary the portion of the beam in the soot layer is visible from light which is scattered by the soot. While the measurements are made, the positions are noted where only a fraction of the beam is in the soot layer. At the inner boundary an increase in the experimental standard deviations of the volume fraction of soot and the most probable radius occurs. On these bases data points are rejected where  $\sigma_{f_v}/f_v > 0.4$ . The increase in the length of the standard deviation bars in Figs. 2-2 through 2-8 at

the soot layer boundaries is largely due to these fluctuations.

#### 2.4 Results and Discussion

Profiles of the volume fraction of soot are shown in Fig. 2-2 for five liquid fuels and PMMA at a height of 4 cm above the leading edge of the fuel surface. Results from at least two different horizontal scans are shown for each fuel. Table 2-1 lists values of soot volume fractions, the most probable radius, and total particle concentrations at the peaks of these profiles. Since no significant change in the data occurs for wicks of different widths, errors due to the end effects are negligible. The volume fraction of soot for toluene, an aromatic compound, is exceptionally large. Previous studies of soot formation have found that aromatics have an unusually large sooting tendency [23]. The five liquid fuels were included in tests for sooting heights by Clarke, Hunter, and Garner [2]. Their ranking of the fuels for the amount of soot formation agrees with the data in Fig. 2-2.

Previous measurements in small pool fires [15-19,53] show the volume fraction of soot at 2 cm above the fuel surface for PMMA, iso-octane, and toluene are  $0.22 \times 10^{-6}$ ,  $0.46 \times 10^{-6}$ , and  $4.8 \times 10^{-6}$ , respectively. For pool fires, the results are average values across the fire, and they are between the maximum and minimum values of the profiles in the boundary layer.

Figures 2-3 through 2-6 present profiles of the volume fraction of soot at various heights from the leading edge of the fuel surface for the five liquid fuels. Experimental standard deviations of  $f_v$  are shown by bars, which were obtained from standard deviations in the

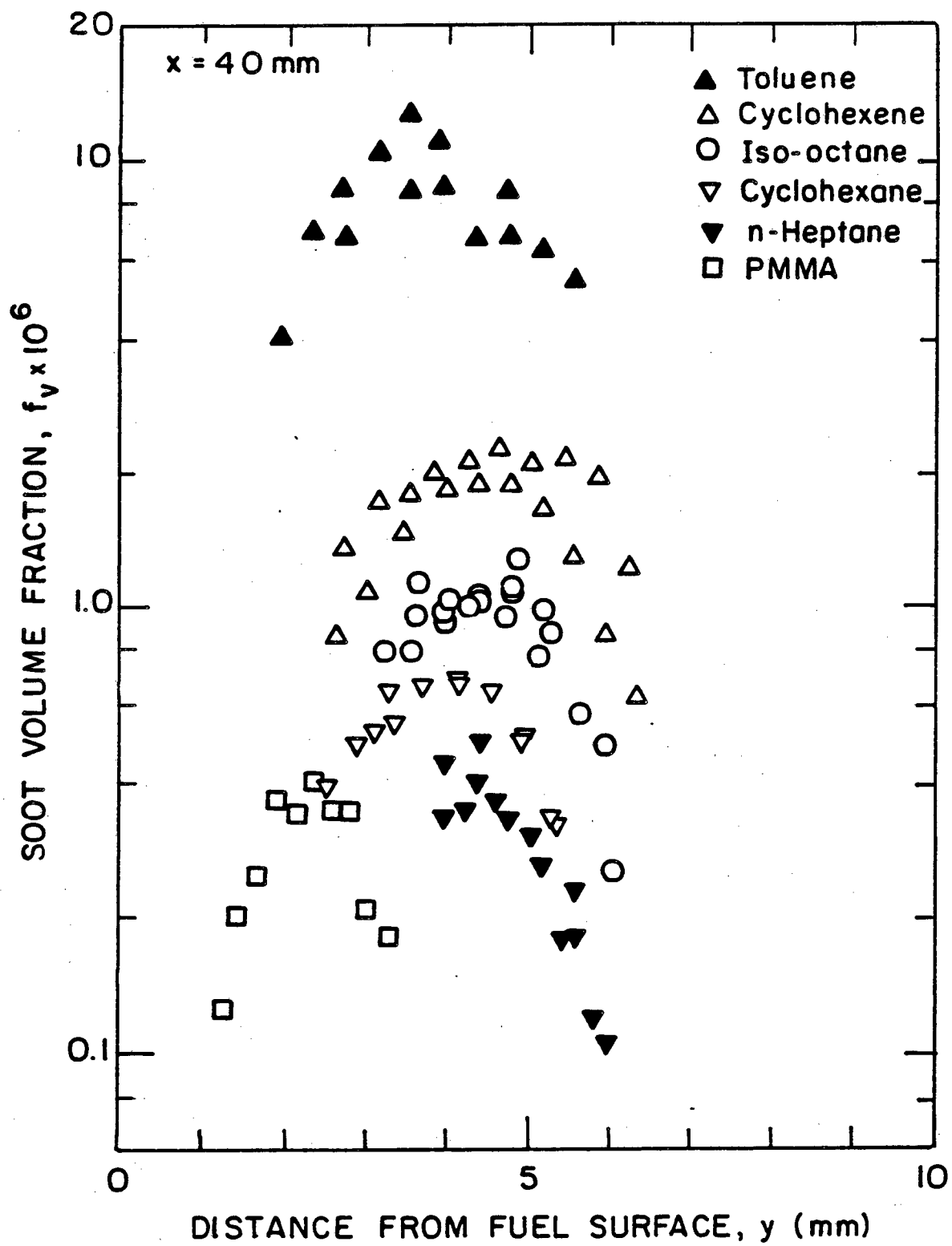
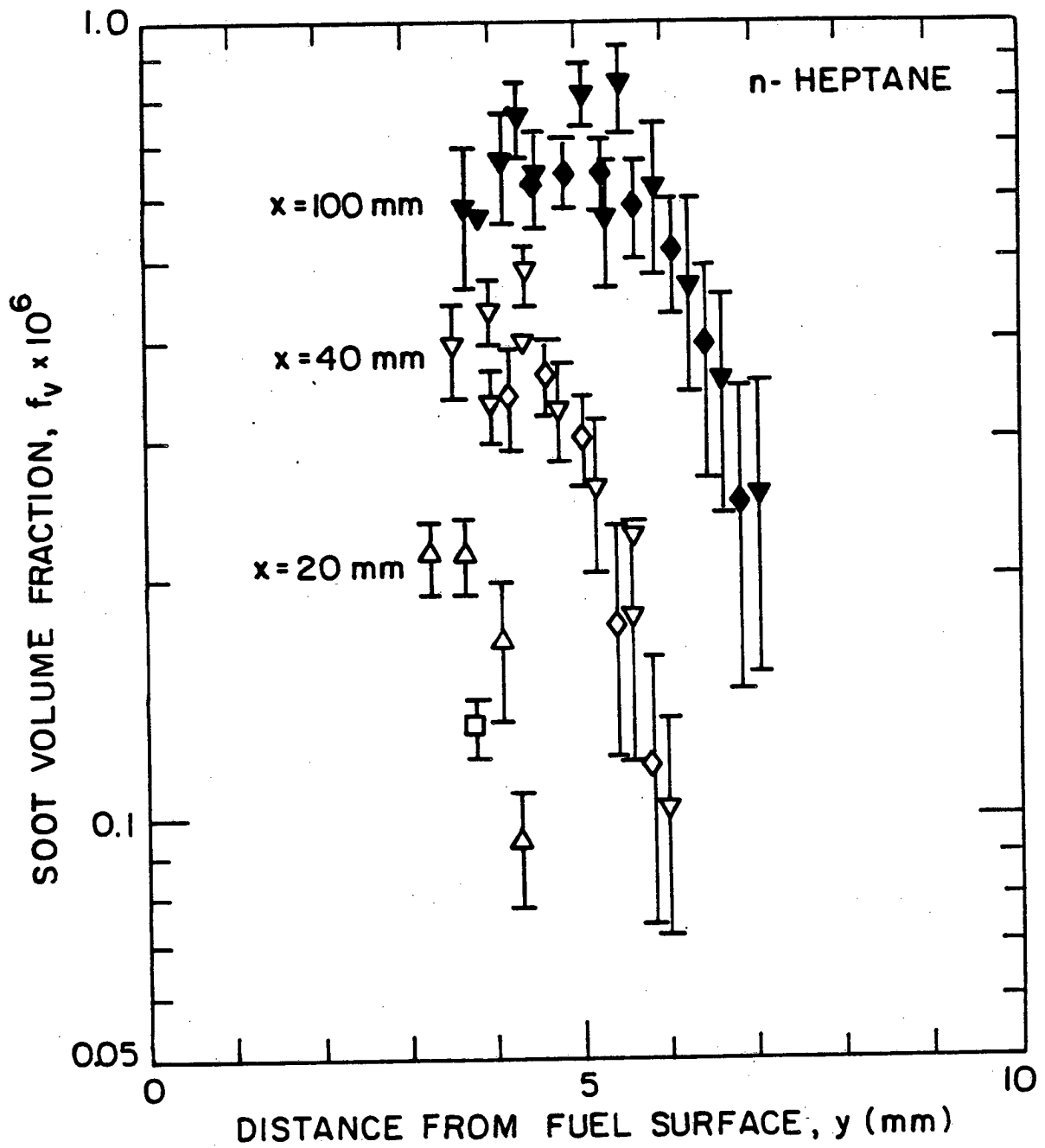


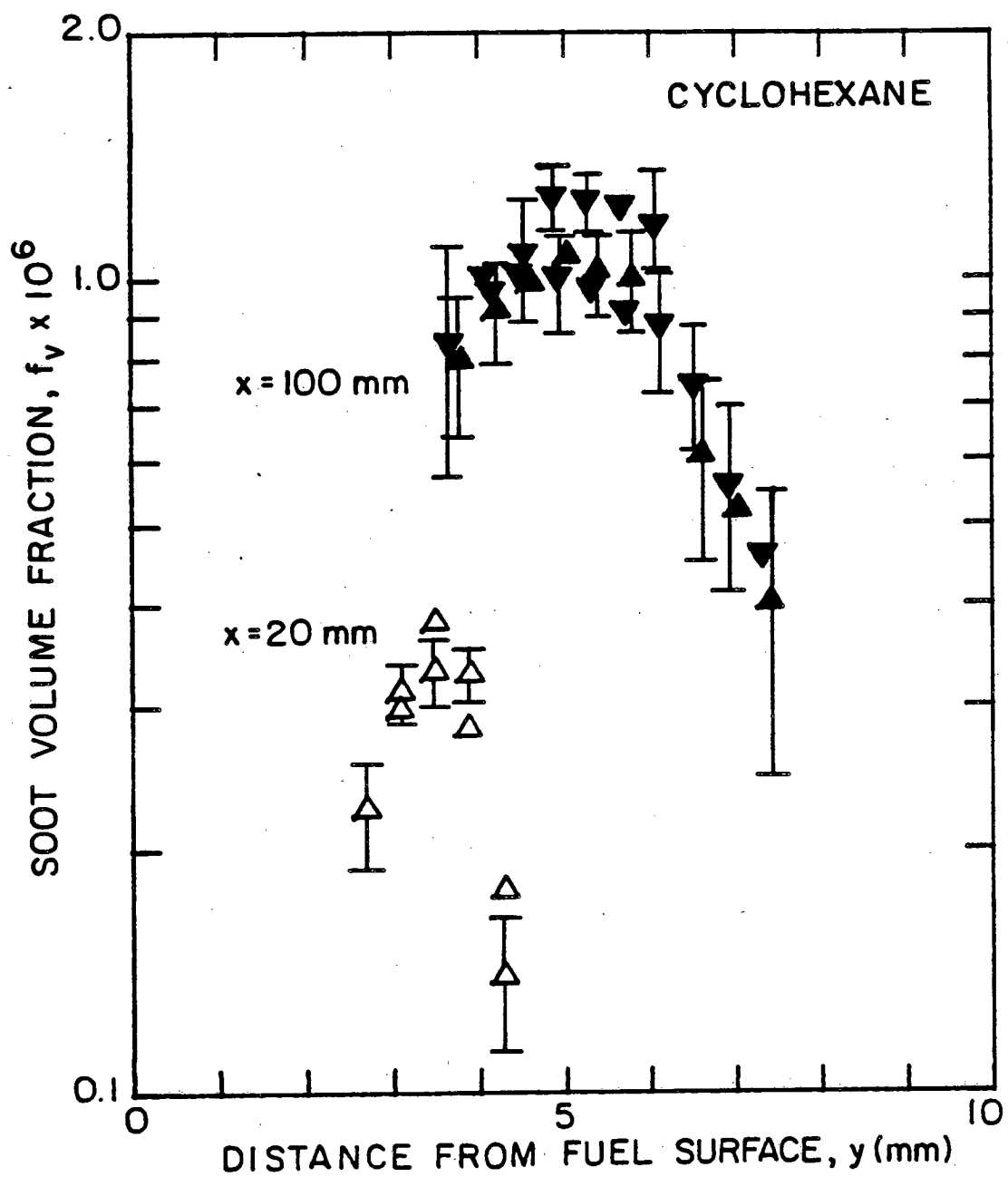
Fig. 2-2

XBL 813-5399



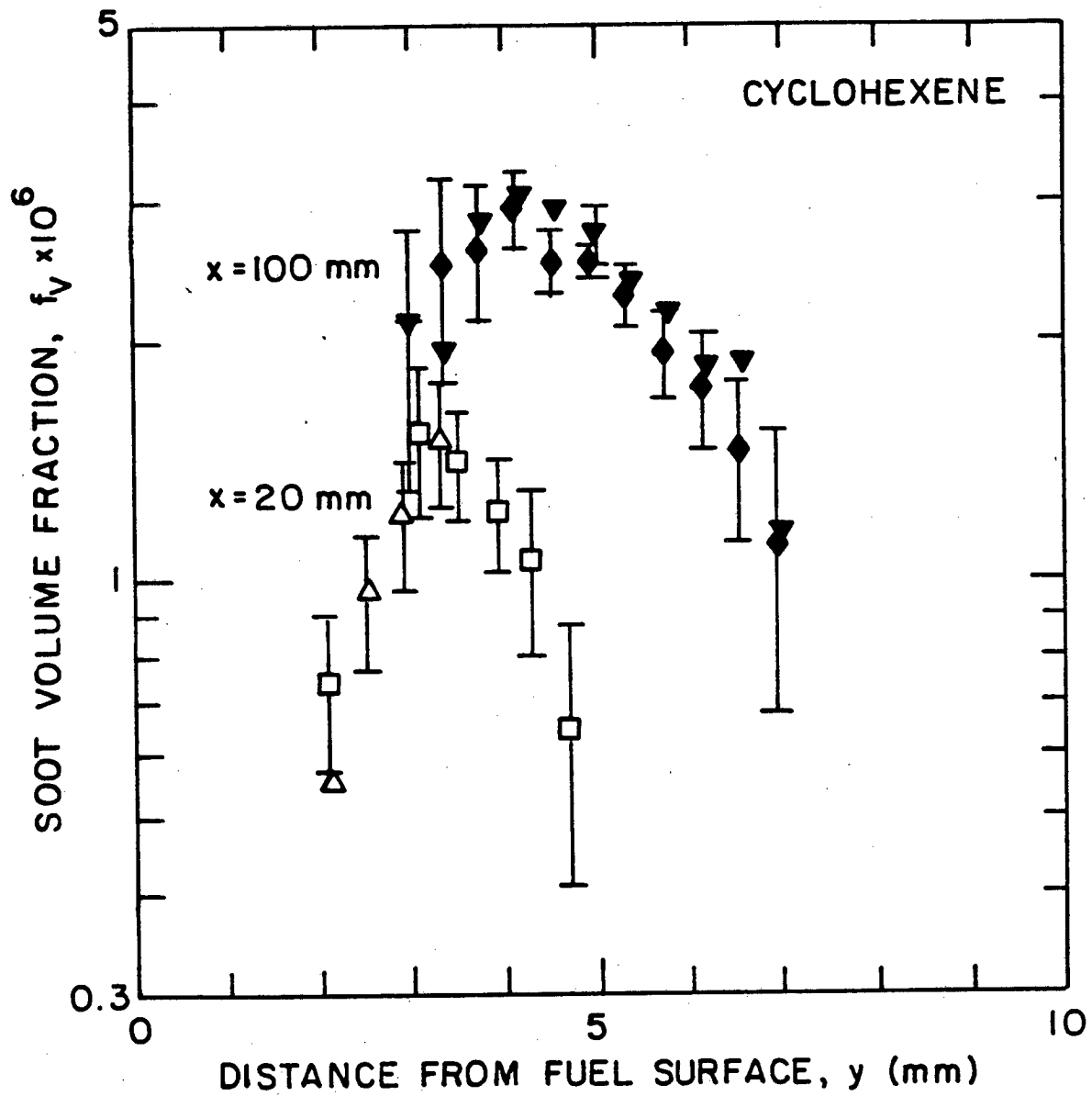
XBL 813-5400

Fig. 2-3



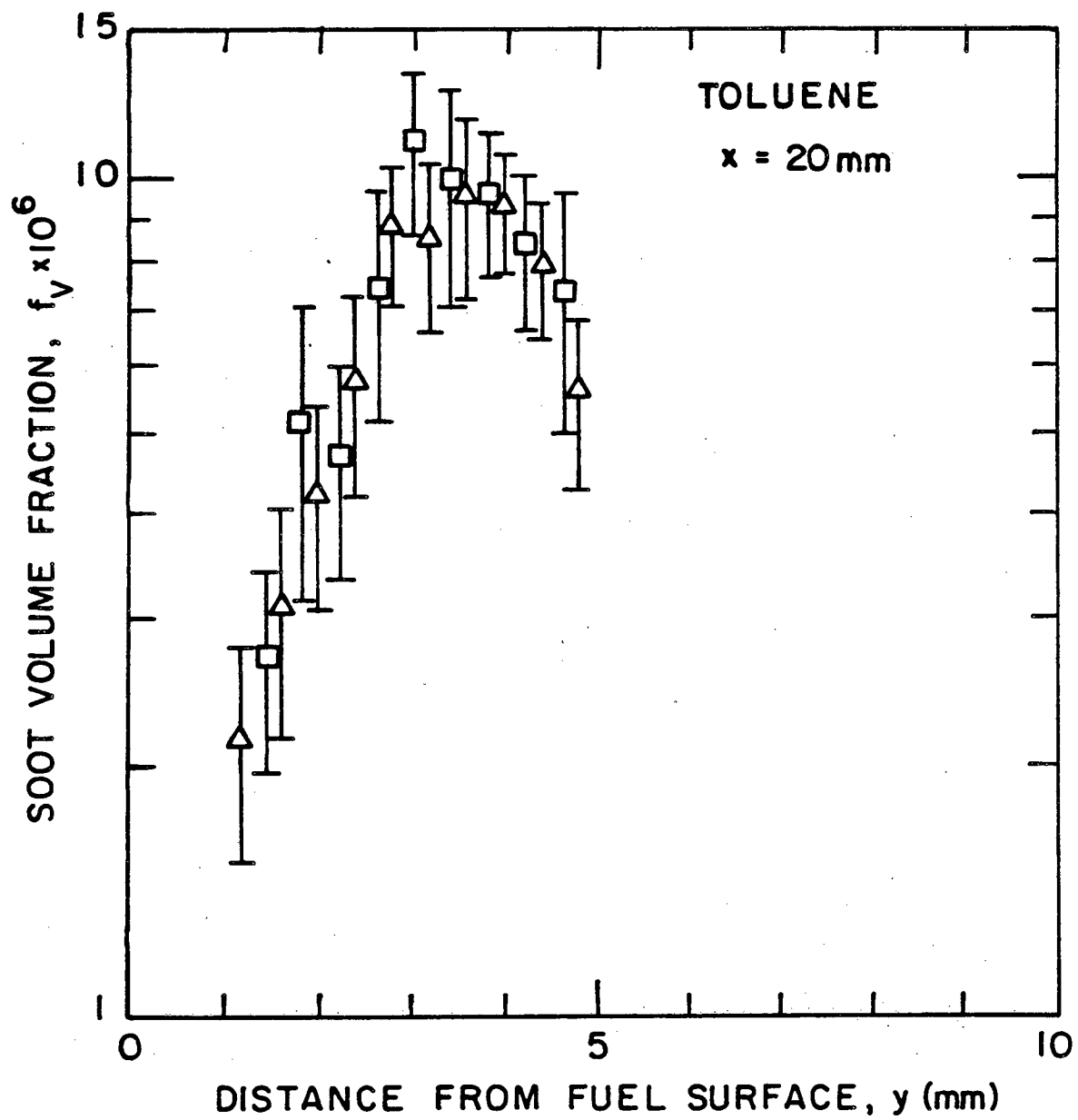
XBL 8111-12809

Fig. 2-4



XBL813-5401

Fig. 2-5



XBL 813-5402

Fig. 2-6



extinction coefficients by standard statistical techniques [17]. Bars are omitted where they would mask trends. The increase in the soot volume fraction for n-heptane is large between the heights of 2 cm and 4 cm, but the amount of increase diminishes with height. Unlike the results for n-heptane, the maximum soot volume fraction for toluene does not change significantly between the heights of 2 cm and 4 cm (compare Figs. 2-2 and 2-6). The variations of soot volume fraction with height for cyclohexene, iso-octane, and cyclohexane fall between the two limiting cases of n-heptane and toluene. As the height increases the outer edge of the soot layer follows the blue flame zone away from the fuel surface, and the width of the soot layer increases. At the lower heights the effects due to the opposing processes of formation and oxidation of soot are more apparent, causing sharply peaked  $f_v$  profiles. From Figs. 2-3 and 2-6 soot particulates are found closer to the fuel surface for toluene than n-heptane at a height of 2 cm. It is unclear if soot particles are formed closer to the wall for toluene, because convection of soot particles from upstream may transport particles to a location where they are not formed. The shapes of the profiles for cyclohexane and cyclohexene at a height of 2 cm fall between the two limiting cases of n-heptane and toluene. Although the position of the inner edge of the soot layer varies between fuels, the location of the outer edge is approximately the same for all the liquid fuels. Since the thermophysical properties of these hydrocarbon fuels are similar, as shown in Appendix C, the location of the flame zone is approximately the same. The peak of the profile shifts toward the fuel surface

relative to the edges of the soot layer with increasing height for cyclohexene and toluene.

In Fig. 2-7 the profiles of volume fraction of soot for PMMA are shown at heights of 4 cm and 10 cm above the leading edge of the fuel surface. The maximum in the profile increases only slightly with height. The distance of the flame zone from the fuel surface is less for PMMA than the liquid fuels, and the distance between the peak of the profile and the fuel surface remains approximately constant with height above 4 cm.

For all the fuels the most probable radius,  $r_{\max}$ , is between 20 nm and 50 nm, and the particle radii do not change significantly across the soot layer. Fig. 2-8 presents profiles of  $r_{\max}$  at 2 cm and 10 cm above the leading edge for cyclohexene. The slight increase of  $r_{\max}$  with height is typical for the fuels in this study. Similar results have been obtained in pool fires [19].

The total particle concentration,  $N_o$ , increases with height as shown in Fig. 2-9 for cyclohexene. Since the width of the soot layer also increases with height, the number of particles across the entire soot layer increases with height. The peaks in the particle concentration profiles correspond to peak soot volume fractions, because the particle radius is approximately constant across the layer.

The reproducibility of the final results for soot volume fractions agree with the uncertainty estimate of  $\pm 15\%$  from an error analysis in Appendix B. However, the scatter in the data for  $r_{\max}$  and  $N_o$  exceeds the uncertainty estimates of  $\pm 15\%$  and  $\pm 50\%$ ,

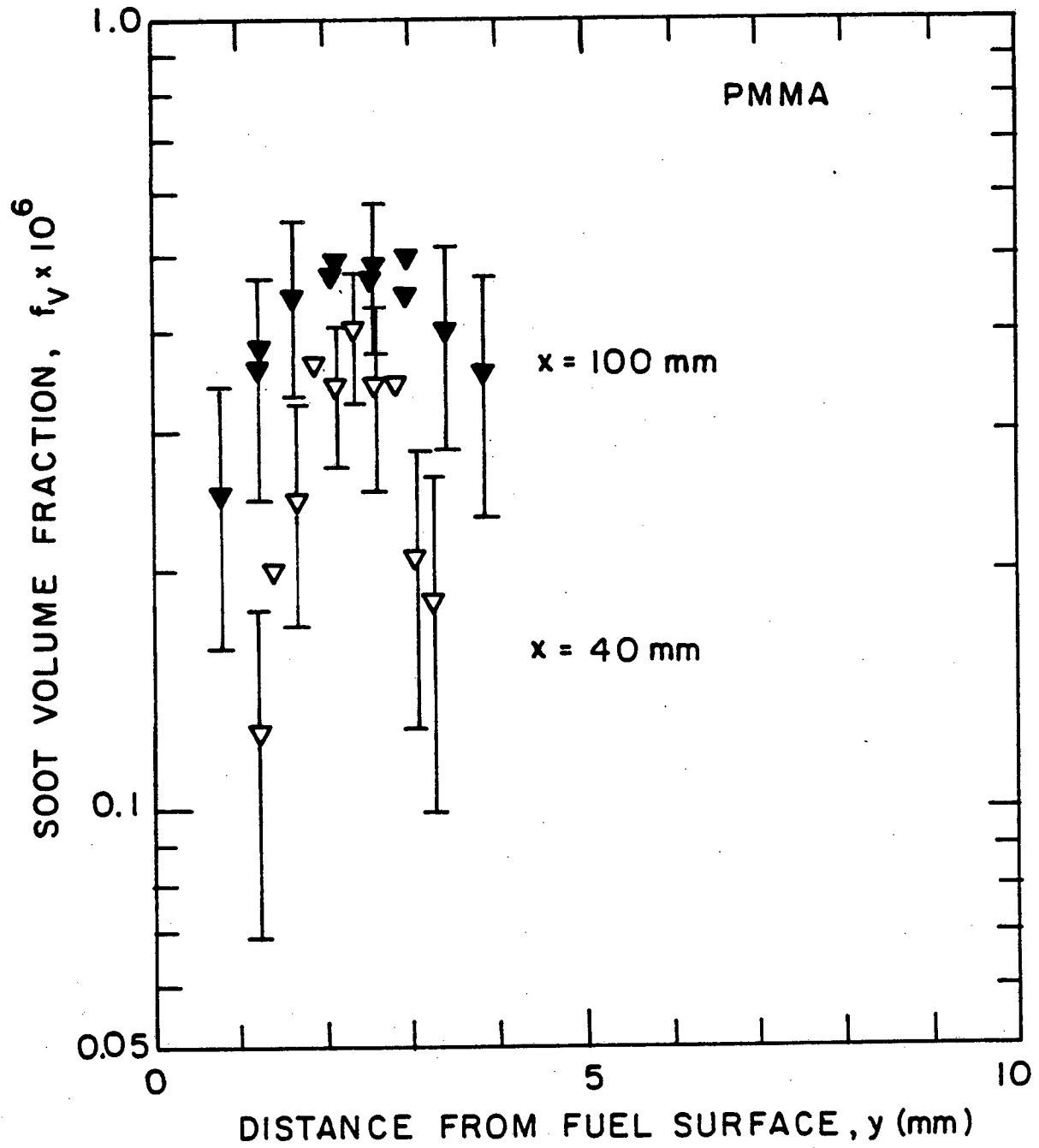
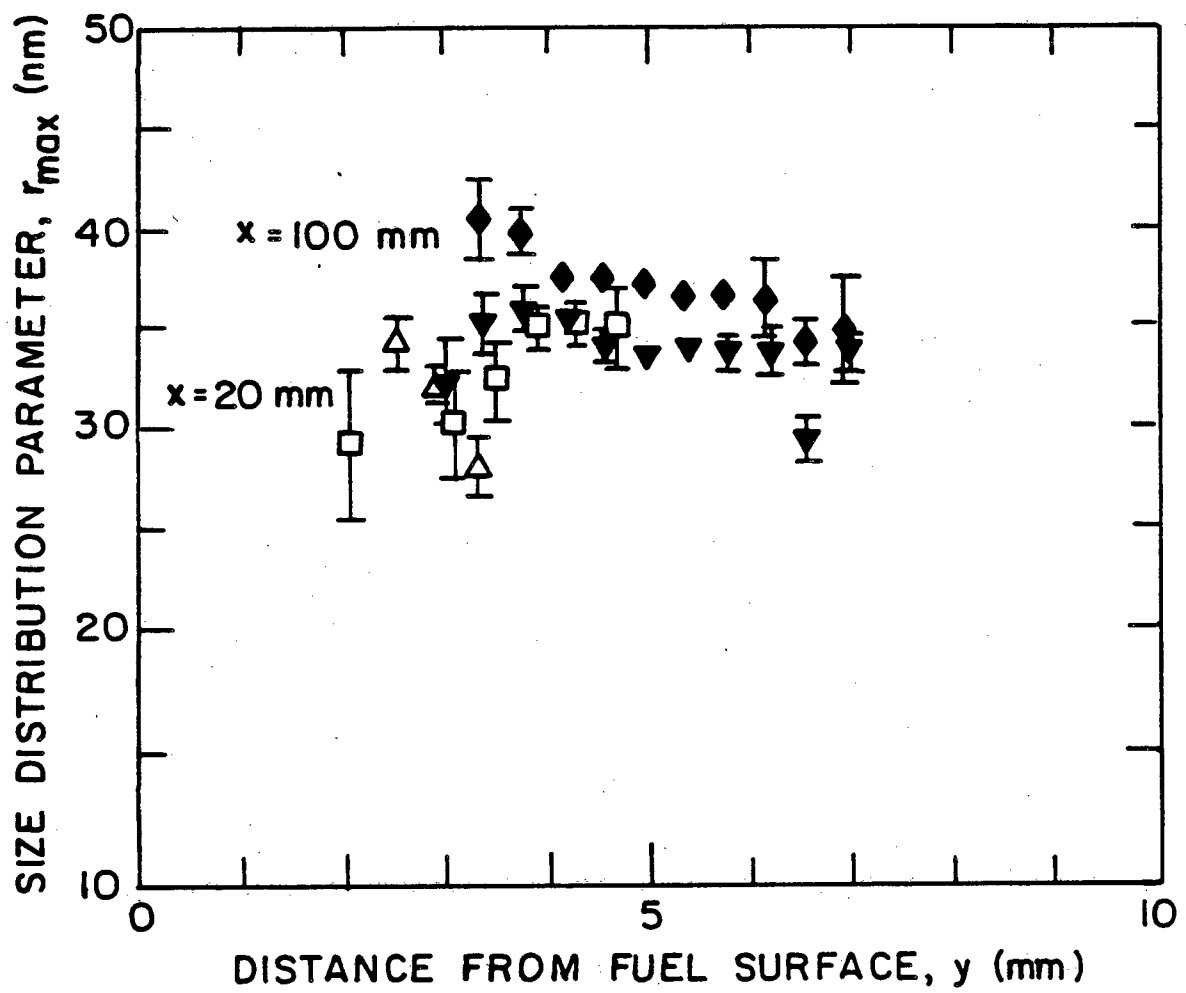


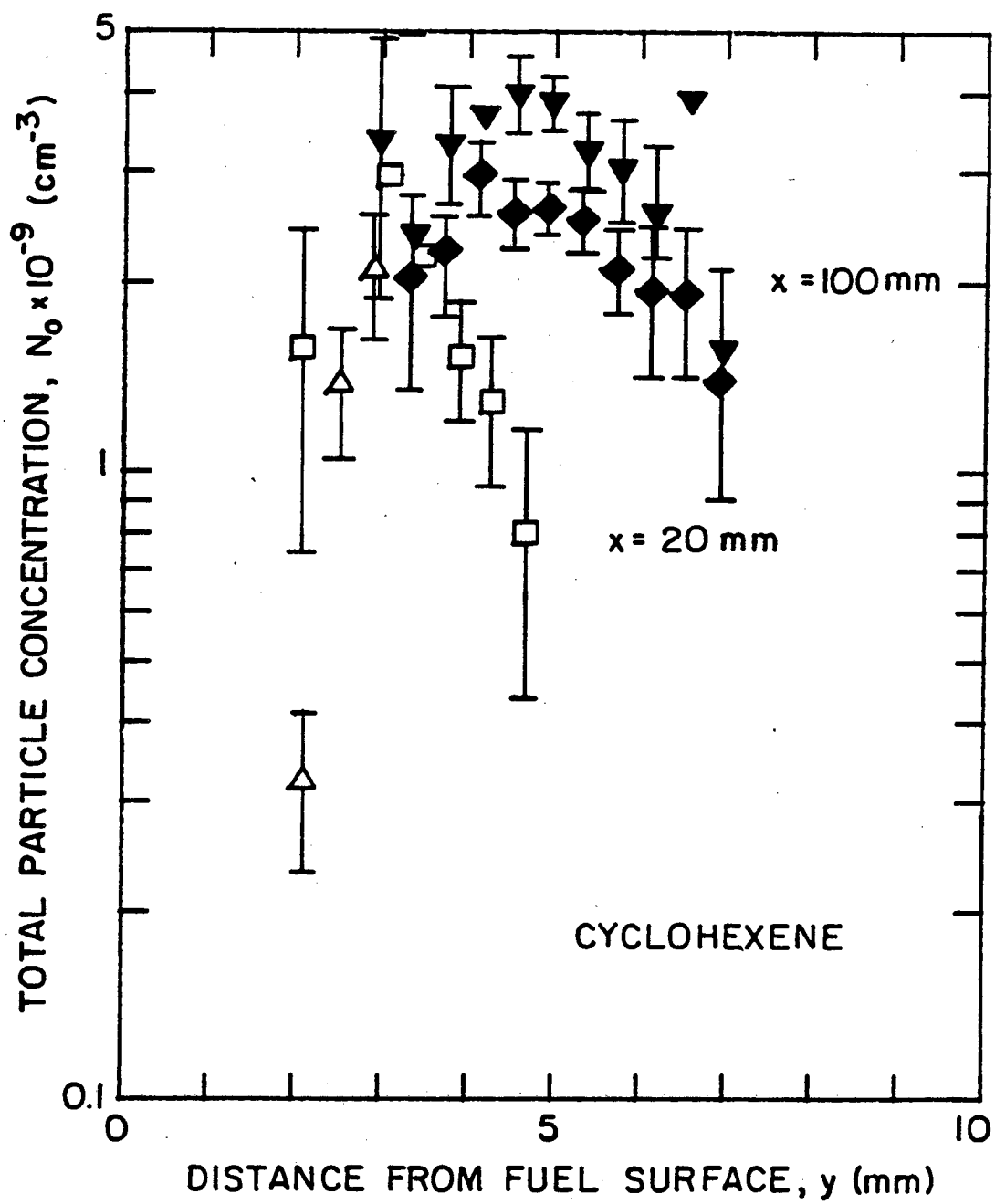
Fig. 2-7

XBL 813-5403



XBL813-5404

Fig. 2-8



XBL 8111-12810

Fig. 2-9

respectively. A possible cause of the lower precision is the laser beams are not absolutely superimposed. Since attenuation varies with position, a difference in relative position of the laser beams, will change their relative attenuations. For beam widths of less than 0.40 mm, estimates show the distance between the centers of the two beams is less than 0.02 mm for all the experiments. The effects due to this misalignment are greater in the combusting boundary layer than in pool fires [15-19], because the gradients in the  $f_v$  profiles are much steeper in the boundary layer. Although the attenuation of the laser beams is due to scattering and absorption,  $r_{\max}$  is determined by the relative amounts of scattered light at different wavelengths (see Fig. 3 of reference 18). Thus,  $r_{\max}$  is more sensitive to this misalignment than  $f_v$ , which depends on both absorption and scattering.

## 2.5 Conclusions

Soot volume fractions and size distributions have been measured in a well characterized combusting boundary layer in free flow for five liquid fuels and PMMA. A soot region is observed on the fuel side of the flame zone. The ranking of the fuels by soot volume fraction is preserved between small pool fires [15-19] and a laminar, combusting boundary layer. A previous ranking of the fuels by their sooting height [1] agrees with our measurements of soot volume fractions. In the laminar boundary layer the soot volume fraction increases with height for all fuels, but for fuels with a high soot volume fraction the variation with height is small. When the width of the soot layer is compared for different liquid fuels near the leading

edge, a more sooty fuel produces a wider soot layer; e.g. for n-heptane the soot region is narrow. The convection of particles downstream widens the soot layer until, at a height of 10 cm above the fuel leading edge, the width of the soot layer is approximately equal for all the liquid fuels. The particle radii increase only very slightly with downstream distance for all the fuels tested.

## Chapter 3: SOOT VOLUME FRACTIONS IN FORCED FLOW

### 3.1 Introduction

In a compartment fire, composition of the gas in the enclosure changes as oxygen is consumed and products of combustion are formed. The effect of oxygen mass fraction on soot volume fraction is important for calculations of radiative heat transfer. In this study, the dependence of soot volume fraction on the ambient mass fraction of oxygen is determined in a forced combusting boundary layer. An increase in the free stream oxygen mass fraction increases the flame temperature, which influences the rates of soot formation and oxidation.

Recently, Glassman and Yaccarino [4] measured sooting heights at various oxygen concentrations. Santo and Tamamini [25] used a modified Schmidt Method technique to measure the flame radiance of a pool fire against a variable background of black body radiation. These measurements allowed them to determine absorption-emission coefficients and trends in soot volume fraction for different ambient oxygen concentrations. While these previous studies give qualitative trends, the present study reports quantitative data at different oxygen concentrations.

### 3.2 Experimental Method

The experiments are performed in a wind tunnel designed to produce a uniform flow of an oxidizing mixture of nitrogen and oxygen above the fuel surface. The wind tunnel consists of a mixing chamber, contraction section, and test section as shown in Fig. 3-1. The



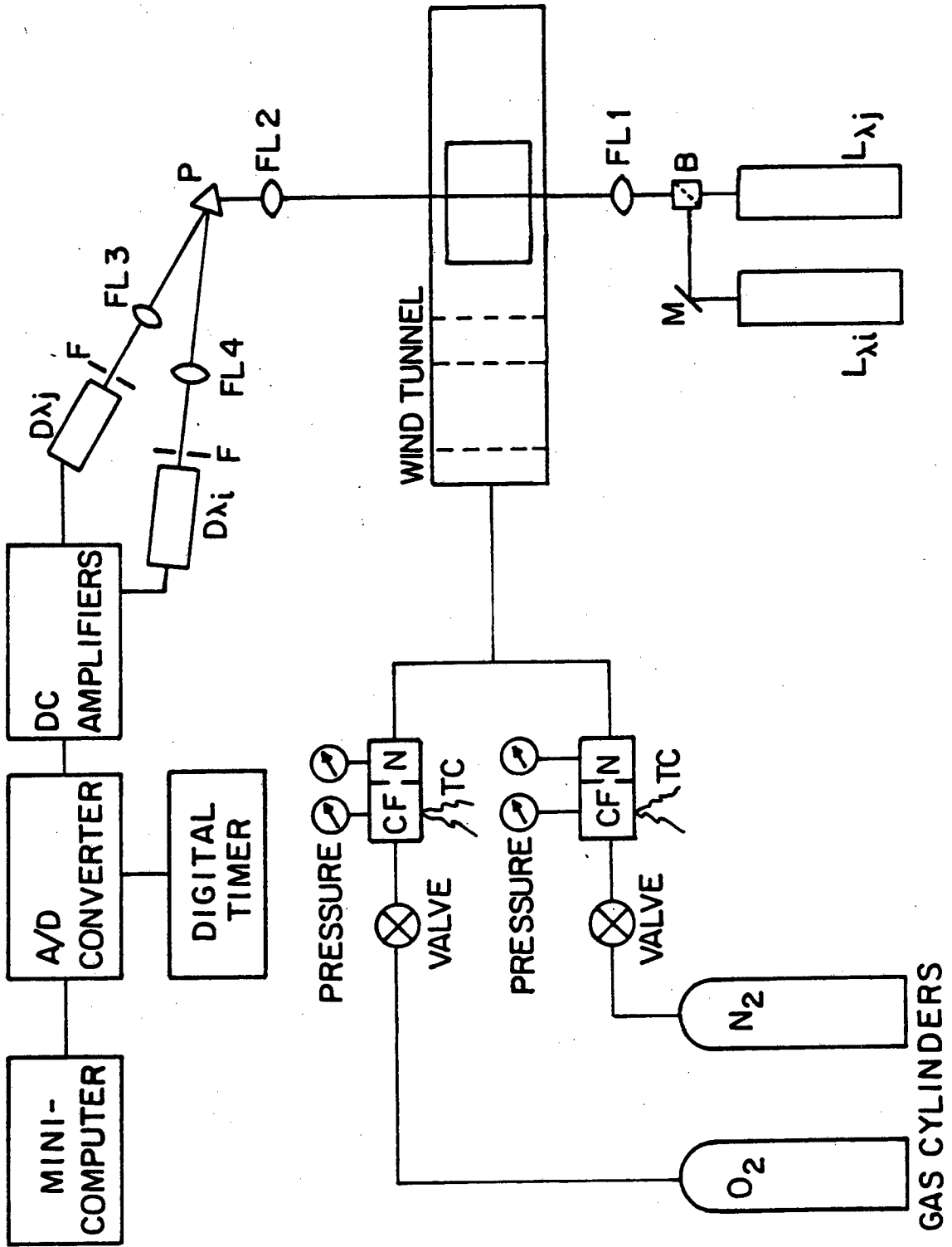


Fig. 3-1

XBL611-12611

mixing chamber is divided into sections by screens with one section packed with steel wool. A rapid contraction of two walls accelerates the flow and minimizes the thickness of the boundary layers on the walls at the entrance of the test section. With an area contraction ratio of 6, the shape of the contraction is similar to the one used by Brown and Roshko [54]. The contour of the contraction is defined by two circular arcs as shown in Fig. 3-2. The horizontal test section has a rectangular cross section, 18 cm wide and 5 cm high. The sides of the tunnel and the ceiling directly over the fuel surface are made of pyrex glass to provide visibility and access for optical measurements. The fuel wicks and solid fuel are placed flush in an inert floor, Marinite-XL (John-Manville Co.), 5 cm behind the exit of the contraction. The oxidizer flow is measured by a set of four critical flow nozzles for each of the component gases, oxygen and nitrogen. The nozzles are calibrated individually at operating conditions by a wet test meter. For each gas, the stagnant chamber pressure upstream of the critical flow nozzles is measured by a Bourdon tube gauge. A copper-constantan thermocouple upstream of the nozzles is used to measure the stagnant chamber temperature. The static pressure downstream of the nozzles is also monitored to insure choked operation of the nozzles.

For the laser transmission experiments, the optical system is the same as in the free flow experiments described in Chapter 2. Measurements in the free flow case demonstrated that the laser power output is sufficiently stable to make monitoring of the laser power output unnecessary.

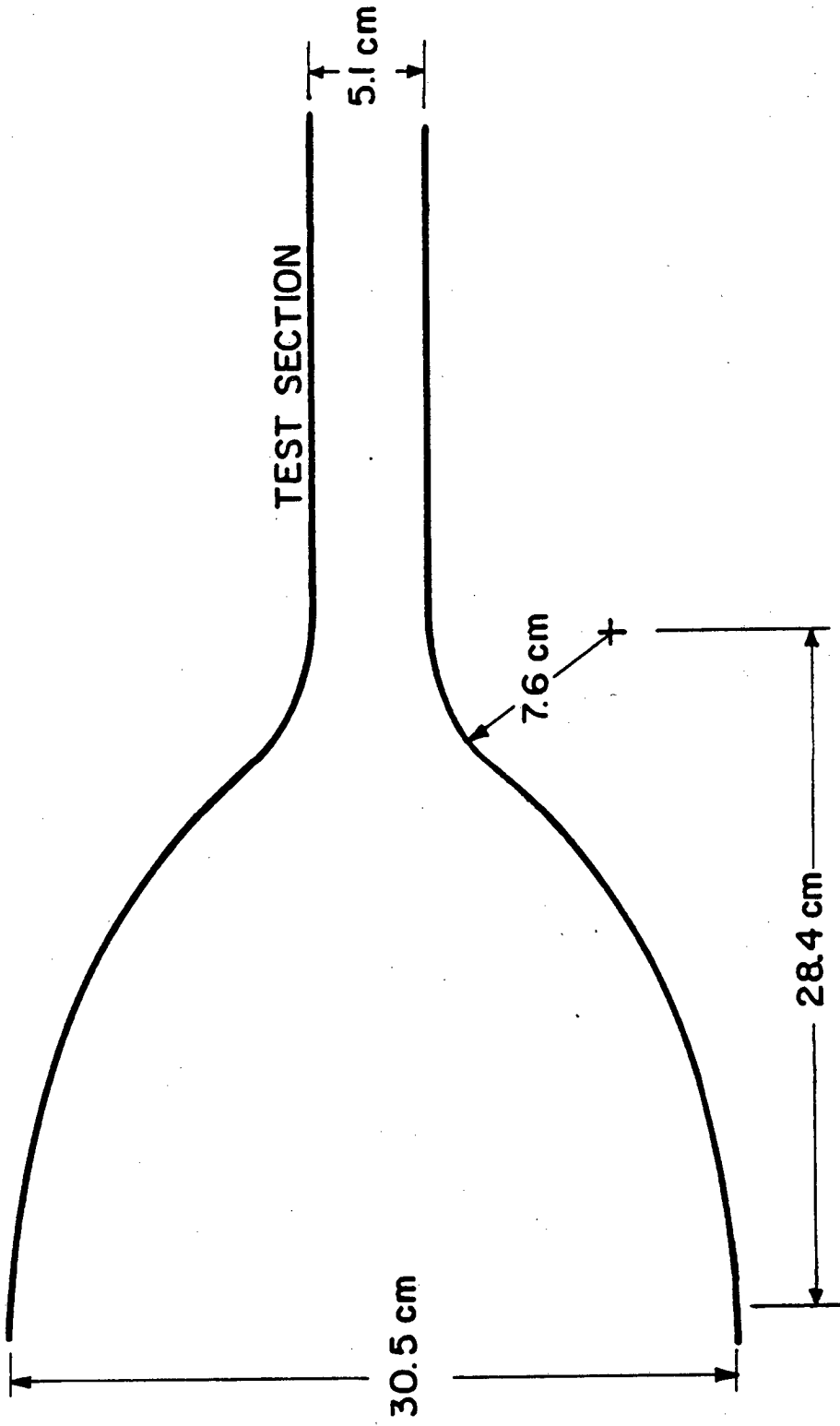


Fig. 3-2

XBL8111-12812

Since the transmitted intensity of the laser beams varies greatly for different fuels and oxygen mass fraction, wicks of different widths are used as listed in Table 3-1. The length of the wick is 12 cm except for toluene where the length is 8.4 cm. The samples of PMMA are usually 12 cm long, 12 cm wide, and 1.27 cm thick. The diameter of the laser beam limits the spatial resolution of the transmission measurements. For all pathlengths used the maximum beam width between points of  $1/e^2$  intensity is less than 0.3 mm. Since variations in temperature and species change the index of refraction in the direction normal to the fuel surface, the fire deflects the laser beam. However, the deflection does not decrease the spatial resolution with the lense system shown in Fig. 3-1.

The entire wind tunnel is placed on a moveable table, so the distance between the fuel surface and the superimposed laser beams can be changed by moving the wind tunnel vertically. A complete scan of the fire is obtained by moving the wind tunnel horizontally between traverses. After the mass flow rates of oxygen and nitrogen are set, the fuel is ignited. For the liquid fuels, the supply of fuel in the wick gives a steady fire for a time period between 3 to 5 minutes, depending on the oxygen mass fraction. This time period allows one vertical scan, with increments of 0.3 mm, through the boundary layer. At each position the outputs of the detectors are read 300 times by the data aquisition system within a 6 second interval. After each vertical scan the fire is extinguished, the horizontal position of the fuel is changed, and the wick is soaked with fuel, before the fire is reignited.

Table 3.1. Summary of Sample Geometries and Peak Soot Volume Fractions and Size Distributions at  $x = 4$  cm with  $u_\infty = 1.5$  m/s.

Fuel	$Y_{ox,\infty}$	Sample Width (cm)	Wave-length Pair, i-j	Path-length L (cm)	Distance from Fuel Surface (mm)	$(I/I_0)_i$	$(I/I_0)_j$	$f_v \times 10^{-6}$	$r_{max}$ (nm)	$N_o \times 10^{-9}$ (cm <sup>-3</sup> )
Toluene (C <sub>7</sub> H <sub>8</sub> )	0.25	1.7	2-4	2.6	2.7	0.0005	0.0011	22	79	2.4
Cyclohexene (C <sub>6</sub> H <sub>10</sub> )	0.23	7.0	2-4	8.3	3.8	0.088	0.20	1.7	40	1.5
	0.25	3.5	1-4	4.7	3.6	0.075	0.25	3.1	31	5.4
	0.25	3.5	1-4	4.7	3.1	0.084	0.27	3.0	30	5.9
	0.25	3.5	2-4	4.5	2.8	0.16	0.27	2.4	48	1.2
	0.25	1.7	2-4	3.1	2.8	0.28	0.43	2.5	39	2.2
	0.35	3.5	1-4	4.7	3.0	0.0016	0.017	7.5	44	4.8
0.35	3.5	2-4	4.5	3.2	0.010	0.038	6.1	48	2.9	
Iso-octane (C <sub>8</sub> H <sub>18</sub> )	0.25	7.0	2-4	8.3	3.2	0.20	0.32	1.1	49	0.52
Cyclohexane (C <sub>6</sub> H <sub>12</sub> )	0.25	7.0	2-4	8.3	3.8	0.38	0.45	0.78	64	0.16
	0.23	12.0	2-4	13.8	4.0	0.62	0.74	0.21	36	0.24
n-Heptane (C <sub>7</sub> H <sub>16</sub> )	0.25	7.0	2-4	8.4	3.7	0.61	0.68	0.37	56	0.11
	0.25	7.0	2-4	8.4	3.8	0.59	0.68	0.38	49	0.17
	0.35	7.0	1-4	8.7	3.5	0.053	0.20	1.9	32	3.2
	0.35	7.0	2-4	8.6	3.2	0.069	0.17	1.9	41	1.4
	0.50	7.0	2-4	8.1	2.9	0.015	0.048	3.1	50	1.3
	0.50	7.0	2-4	8.3	3.1	0.015	0.051	3.0	47	1.6
Polymethyl-methacrylate (C <sub>5</sub> H <sub>8</sub> O <sub>2</sub> ) <sub>n</sub>	0.25	12.0	2-4	12.0	2.6	0.48	0.58	0.37	49	0.17
	0.35	12.0	2-4	12.0	2.1	0.0096	0.043	3.0	42	1.6
	0.50	6.0	2-4	6.0	1.9	0.019	0.060	4.0	48	2.0

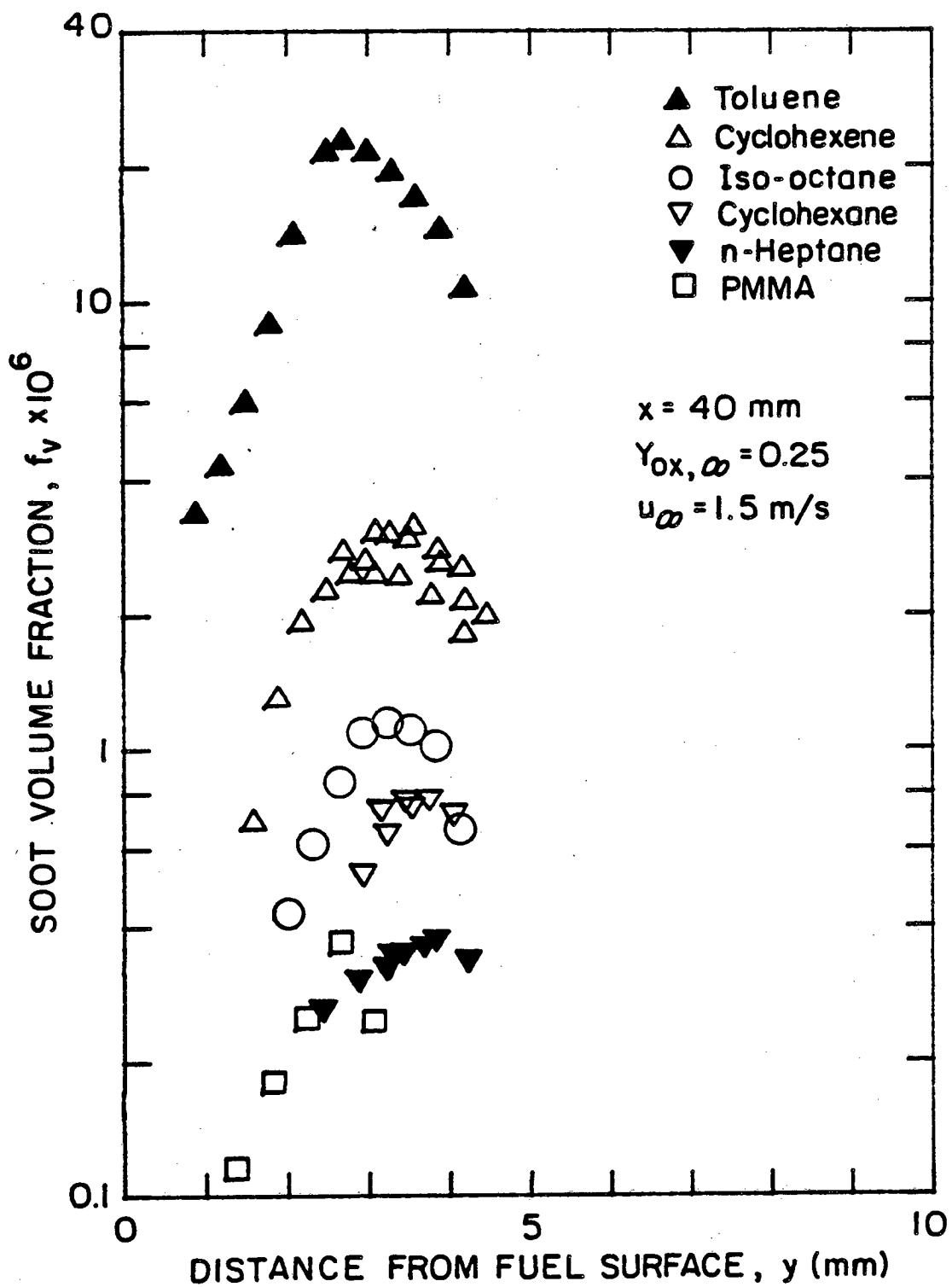
The pathlength,  $L$ , is measured after the fire is extinguished from the deposits of soot on the inert floor. On the side edges of the fire, the flame zone is in contact with the inert floor. Soot is deposited on the inert floor between the fuel surface and this line of flame contact. The width of the fire and the pathlength,  $L$ , are taken to be equal to the distance between the lines of flame contact on each side of the fuel surface. The pathlength is approximately 1 cm longer than the width of the wick. The measured values of  $I/I_0$  for two different wavelengths and  $L$  are used in the extinction analysis, which is discussed in Chapter 2, to calculate  $r_{\max}$  and  $f_v$ . Data for more than one wavelength pair are used to isolate the correct value of  $r_{\max}$  [15,17-19].

For PMMA the fuel regression rate affects the beam distance from the fuel surface. The regression rate is measured before and after each vertical scan through the boundary layer by blocking the laser beams partially with the fuel surface. If the floor of the wind tunnel remains stationary, the surface of the pyrolyzing fuel slab moves and blocks a smaller part of the laser beams. The regression rate is the rate the wind tunnel floor is moved to maintain a constant reading of transmitted intensity for the partially blocked beam. A new sample of PMMA is burned for the transmission measurements at each streamwise position.

### 3.3 Results and Discussion

Profiles of volume fraction of soot are shown in Fig. 3-3 for five liquid fuels and PMMA at a free stream velocity of 1.5 m/s and ambient oxygen mass fraction,  $Y_{Ox,\infty}$ , of 0.25. The standard deviations in the data are about the same as the size of the symbols in the graph. When the data are compared with the measurements in free flow and previous experiments [15-19,53], the ranking of fuels by soot volume fraction is preserved among small pool fires, and free and forced laminar boundary layers. Table 3-1 lists values of soot volume fractions, the most probable radius, and total particle concentrations at the peaks of these profiles. The five liquid hydrocarbon fuels have approximately the same thermal and physical properties, and adiabatic flame temperature. The large variation in soot volume fraction indicates the chemical structure of the fuel has a strong influence on soot formation. With wicks of 12 cm in length, measurements of burning time and mass of the wicks, before and after the burning, show the total pyrolysis rate at the fuel surface for toluene is 40% greater than that of n-heptane. The pyrolysis rates of the other liquid fuels are between these two extremes. For toluene, the largest soot volume fraction provides the largest radiative heat flux into the fuel surface, which causes the largest pyrolysis rate.

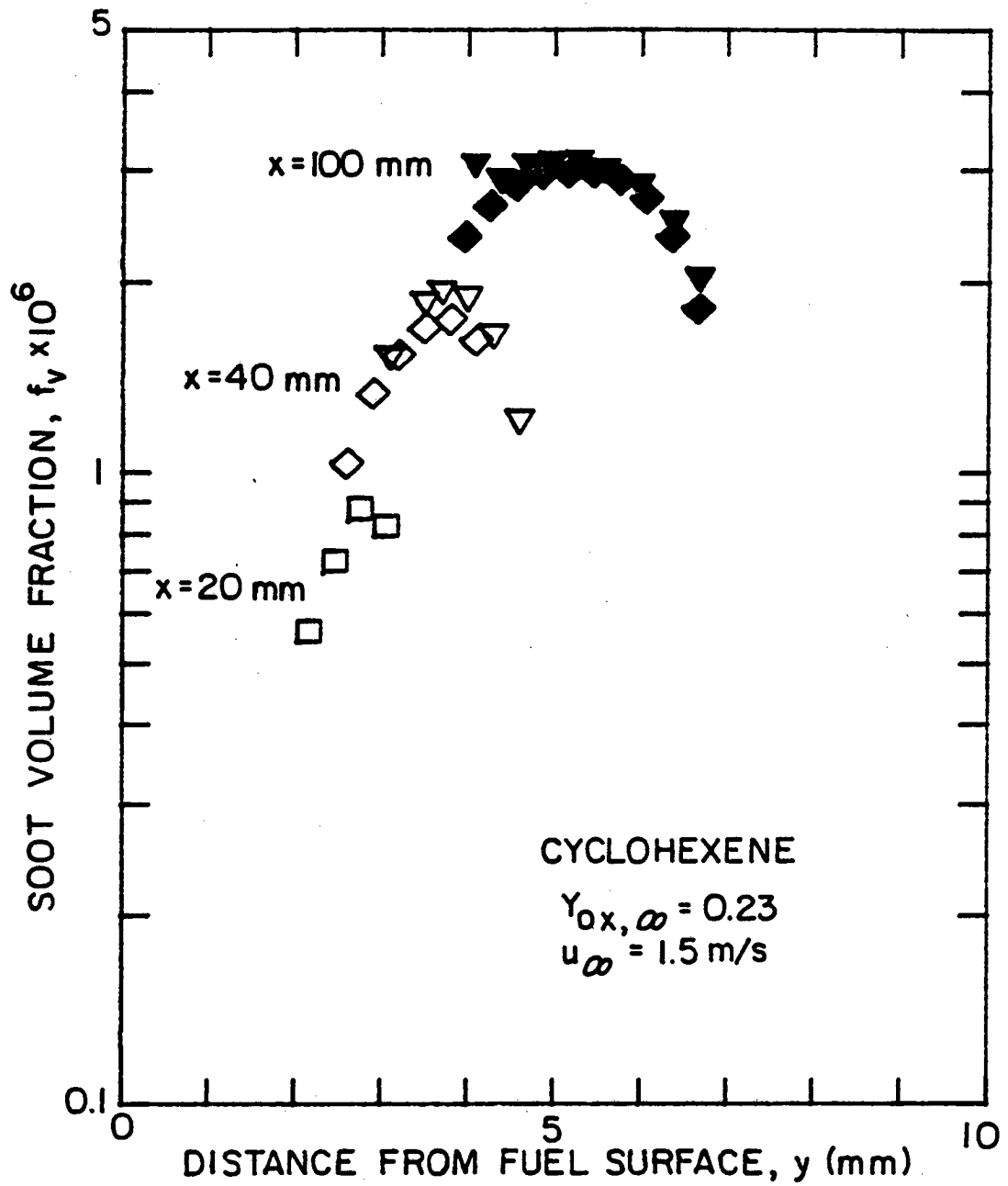
The soot volume fraction increases with downstream distance,  $x$ , for all fuels tested, but for fuels with a high soot volume fraction the variation with  $x$  is smaller. In Fig. 3-4, the profiles for cyclohexene indicate a larger variation in soot volume fraction with  $x$  than determined in the free flow case for  $Y_{Ox,\infty} = 0.23$ . The profiles



XBL 8111-12813

Fig. 3-3





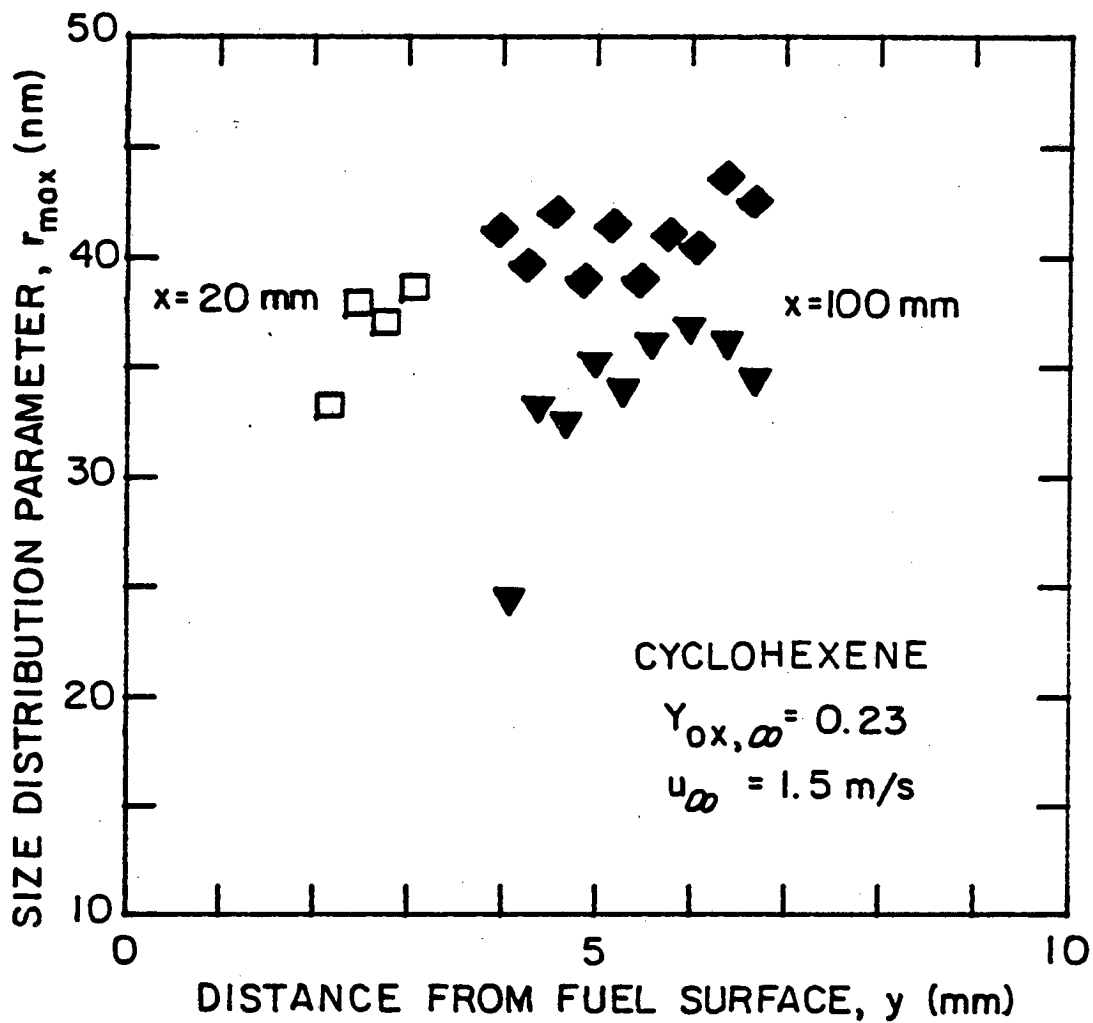
XBL 811F-12814

Fig. 3-4

are sharply peaked at  $x = 20$  and  $40$  mm due to the competing processes of formation and oxidation of soot. Convection of soot downstream tends to round the profile at  $x = 100$  mm. The outer edge of the soot layer follows the flame zone away from the fuel surface with increasing downstream position, and the width of the layer increases.

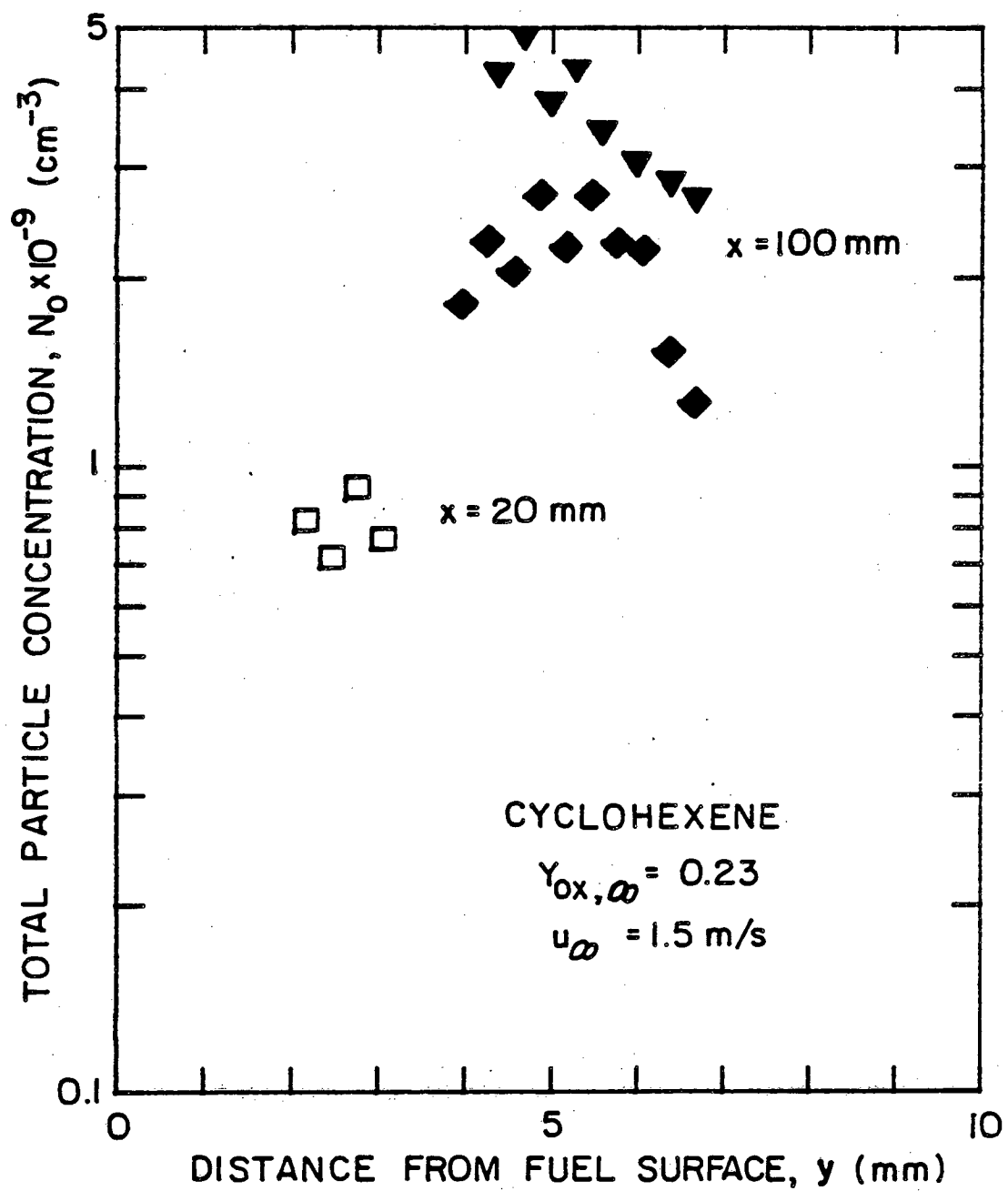
The particle radii do not change significantly across the soot layer as shown in Fig. 3-5. The most probable radius is between 20 nm and 80 nm for all the fuels at  $Y_{\text{ox},\infty} = 0.25$ . Since the particle sizes do not vary with downstream position, the particles apparently do not have sufficient time to agglomerate into larger clusters. The peaks in the particle concentration profiles correspond to peak soot volume fractions as seen by comparing Figs. 3-4 and 3-6.

The soot volume fraction increases with increasing oxygen mass fraction for all the fuels. In Fig. 3-7, results for n-heptane show a small change in the oxygen mass fraction from  $Y_{\text{ox},\infty} = 0.23$  to  $Y_{\text{ox},\infty} = 0.25$  gives a 60% increase in the peak of the volume fraction profile at  $x = 100$  mm. The results demonstrate the volume fraction is less sensitive at higher oxygen mass fractions, since a change from  $Y_{\text{ox},\infty} = 0.35$  to  $Y_{\text{ox},\infty} = 0.50$  gives only a 50% increase in the peak of the profile. As oxygen mass fraction increases, the outer edge of the soot layer moves with the flame toward the fuel surface. Thus, the width of the soot layer decreases. The increase in volume fraction of soot occurs for two reasons. Measurements of the burning time and the mass of the wick, before and after the burning, show the total pyrolysis rate at the fuel surface is doubled by increasing the oxygen mass fraction from  $Y_{\text{ox},\infty} = 0.23$  to  $Y_{\text{ox},\infty} = 0.50$  for a wick of 12 cm in



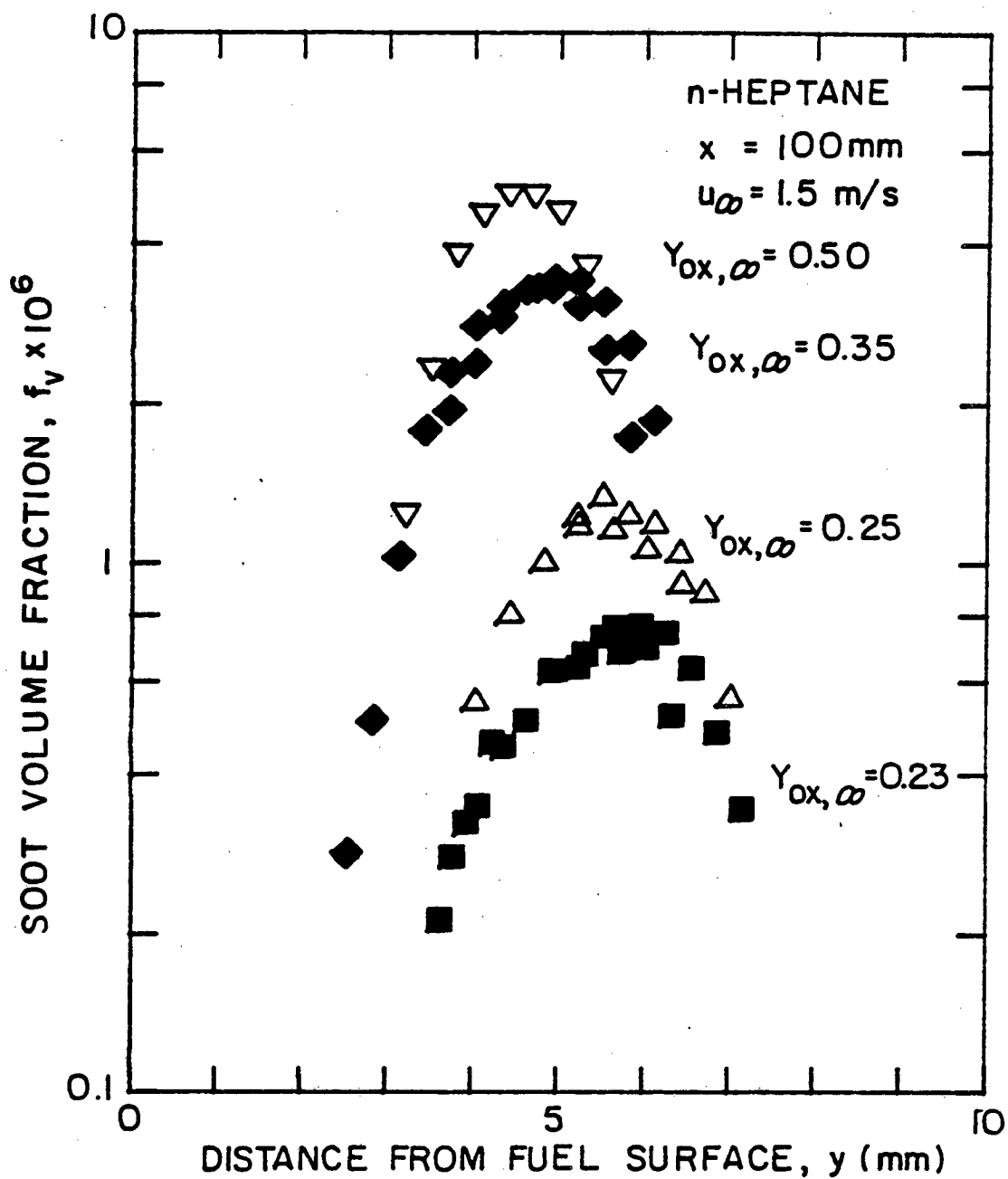
XBL8111-12815

Fig. 3-5



XBL8111-12816

Fig. 3-6



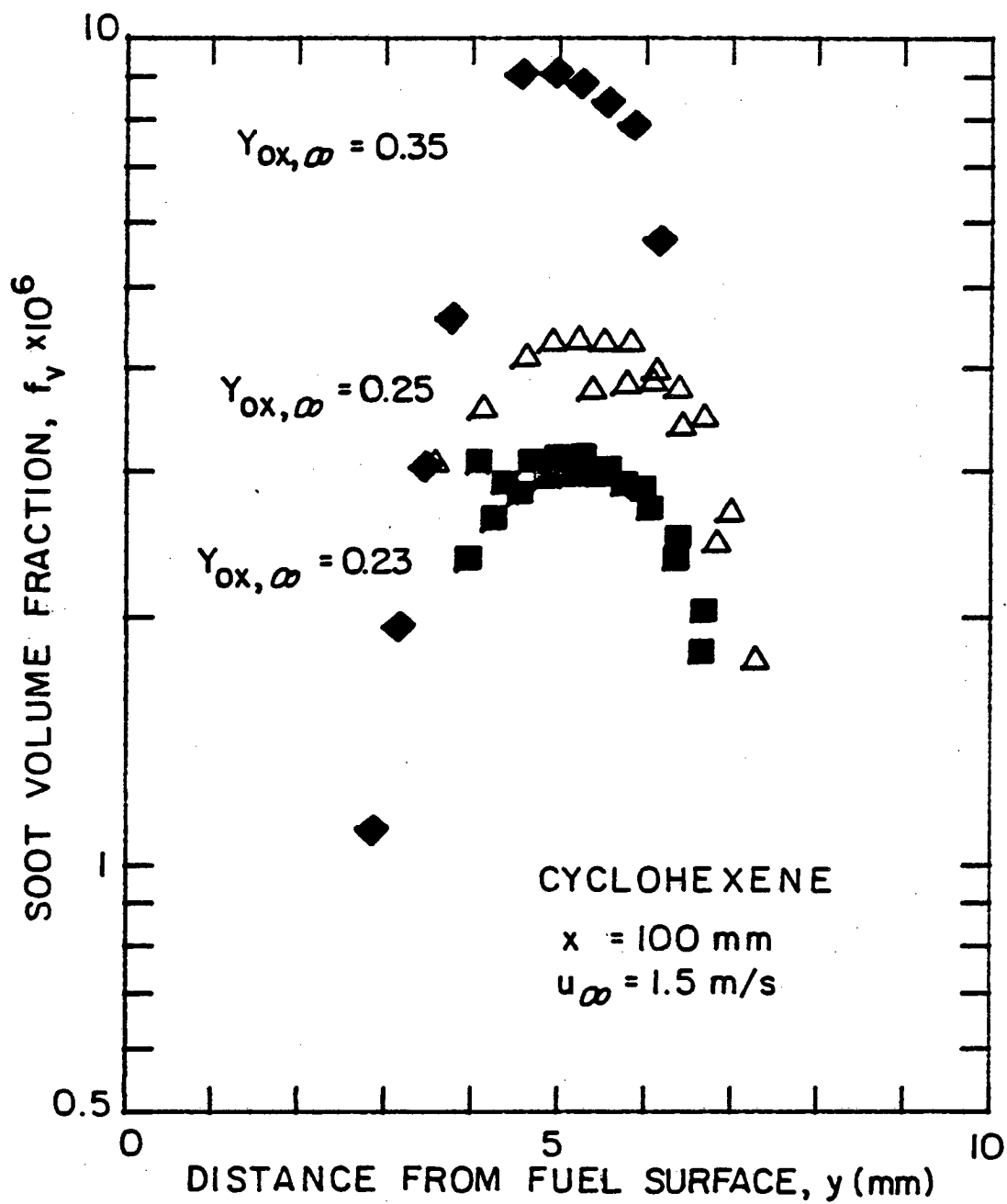
XBL 8111-12817

Fig. 3-7

length. Thus, more fuel feeds the soot formation process at the higher oxygen concentrations. Also, an increase in the flame temperature increases the rates of formation and oxidation of soot as noted by Glassman [3,4]. The large increase of soot volume fraction indicates the formation process prevails between these two competing processes. Similar results for cyclohexene are shown in Fig. 3-8.

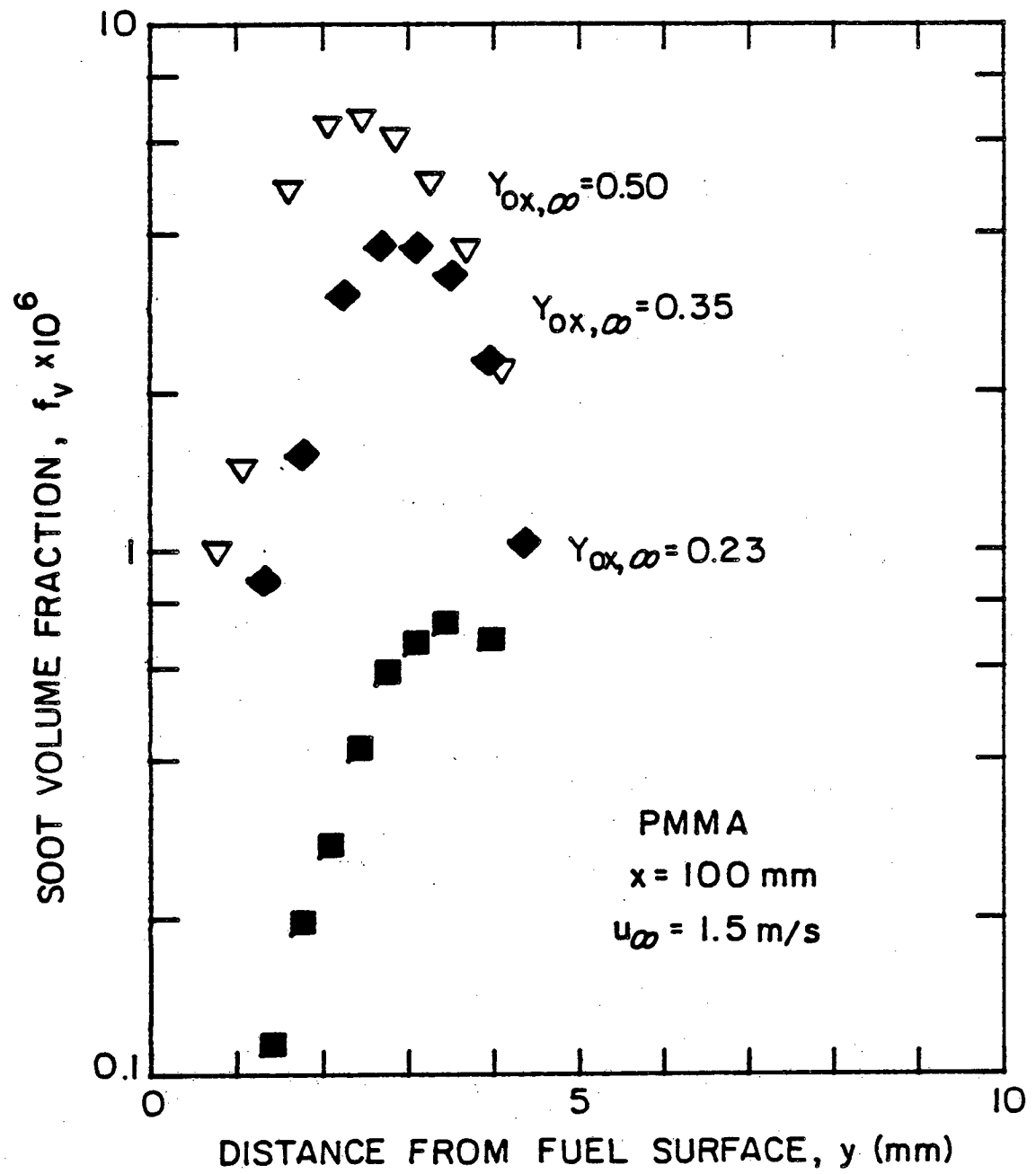
For PMMA the width of the soot layer changes less with oxygen mass fraction than for the liquid fuels as shown in Fig. 3-9. The distance from the fuel surface to soot onset is less for PMMA, and this distance is approximately unchanged with increasing oxygen mass fraction. Again, a large increase in the peak of the volume fraction profile is found with an increase in the oxygen mass fraction. The particle radii do not change significantly with oxygen mass fraction as shown by the results in Table 3-1. For PMMA pool fires, the measurements of Santo and Taminini [25] indicate the absorption coefficient increases with oxygen mass fraction, but the Schmidt temperature is only weakly influenced. They concluded that soot volume fraction increases with an increase in oxygen mass fraction for  $Y_{\text{ox},\infty}$  between 0.18 and 0.21 .

In previous studies some workers determined the tendency of a fuel to soot by measuring sooting heights, while others collected the soot escaping from the combustion zone. By measuring sooting heights for ethene, Glassman and Yaccarino [4] found that increasing the oxygen mass fraction decreases the sooting tendency at lower oxygen mass fractions, but at higher mass fractions increasing the oxygen mass fraction increases the sooting tendency. In separate studies,



XBL 8111-12818

Fig. 3-8



XBL8111-12819

Fig. 3-9

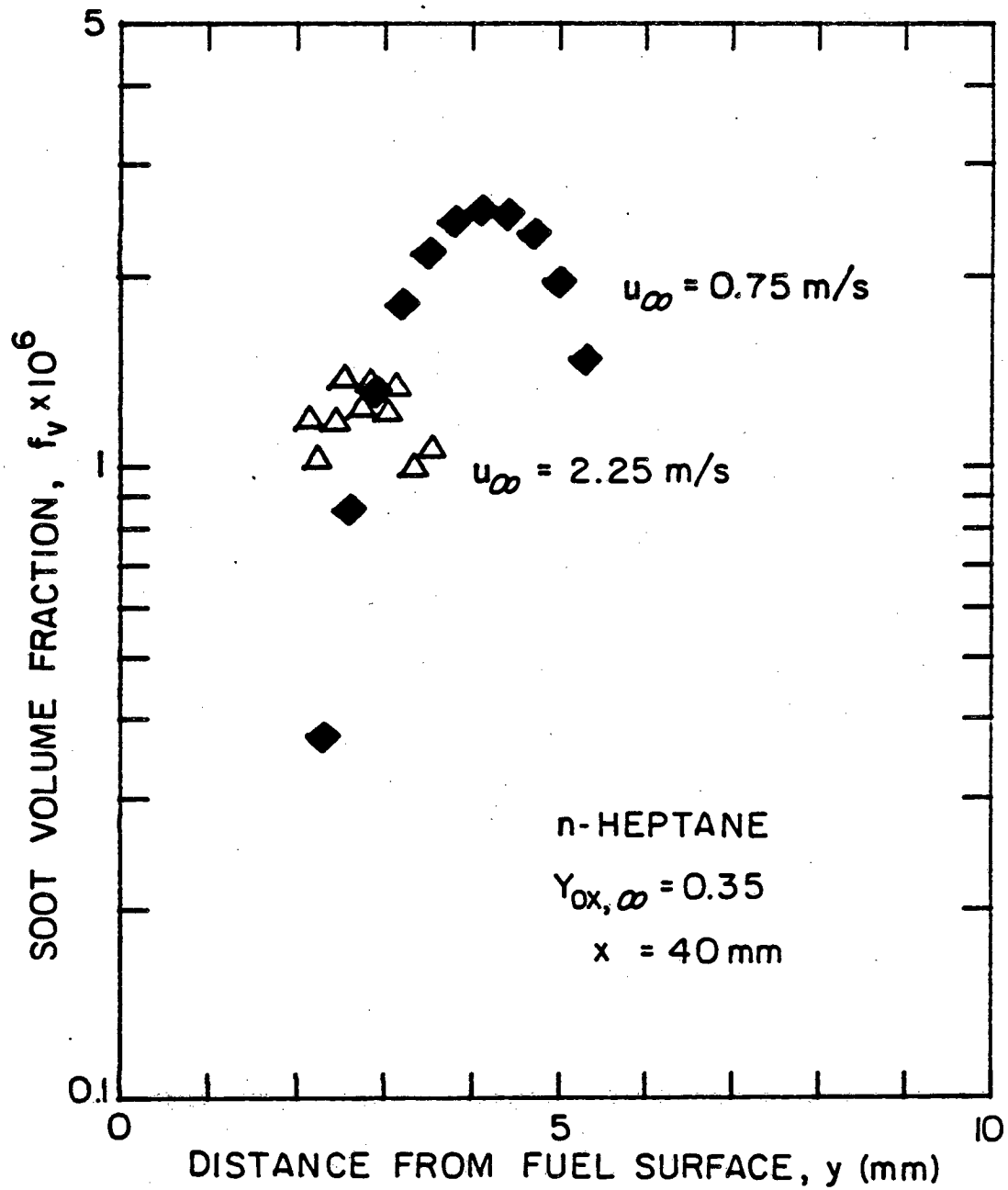


Kadota, Hiroyasu, and Farazandehmehr [5], and Chakraborty and Long [6,7] found opposite trends, when they measured the amount of soot leaving the combustion zone. These reports may seem to contradict each other. However, Glassman has explained the different trends by showing the two measurements give different results. In these previous studies, different fuels were used in diffusion flames with different geometries, so a direct comparison with this study is difficult.

The volume fraction of soot has a weaker dependence on the velocity of the free stream than oxygen mass fraction. In Fig. 3-10, the results for n-heptane are shown, where the free stream velocity,  $u_{\infty}$ , has been changed by a factor of three. The width of the soot layer decreases with increasing velocity as the flame zone moves closer to the fuel surface. Although the soot volume fraction decreases with increasing velocity, the flux of soot at a given downstream position should be used to make a meaningful comparison. The downstream flux of soot at streamwise position,  $\ell$ , gives a measure of the amount of soot formed but not oxidized between  $x = 0$  and  $x = \ell$ . For a calculation of the flux of soot particles, detailed velocity profiles are needed.

### 3.4 Conclusions

For different ambient oxygen mass fractions, soot volume fractions and size distributions have been determined in a forced flow boundary layer. A soot region is observed on the fuel rich side of the flame zone. The soot volume fraction and the width of the soot layer increase with downstream distance. Soot volume fraction



XBL8111-12820

Fig. 3-10

increases monotonically with mass fraction of oxygen, but volume fraction is less sensitive to changes in  $Y_{O_2, \infty}$  at higher oxygen mass fractions. The chemical structure of the fuel also has a large effect on soot volume fraction. The particle size does not change significantly across the soot layer, or with oxygen mass fraction or fuel type.

## Chapter 4: BOUNDARY LAYER MODEL WITH RADIATION

### 4.1 Introduction

To isolate the effects of radiation in fires from complexities of turbulent fluid motion, an analysis is made of a laminar, combusting boundary layer. A preliminary experiment with a vertical wall of PMMA (polymethylmethacrylate) shows that the effects of radiation are significant in the laminar region. The model includes an external radiant energy flux to represent a compartment fire where hot ceiling and walls also transfer radiant energy to the fuel surface.

In a steady, laminar, combusting boundary layer a pyrolysis zone separates a flame zone from the fuel surface as shown in Fig. 1-1. A soot layer is on the fuel rich side of the flame zone. Soot and radiating product gases are not present in the surrounding medium, because the boundary layer entrains air. Through the transparent ambient gas the combusting layer exchanges radiation with a distant black wall, which is maintained at a specified temperature. This investigation, which treats forced and free flows separately, examines the effects of radiation on the pyrolysis rate and the flux of combustible gases escaping downstream at the top of the fuel slab.

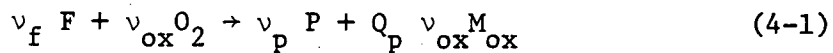
The formation and transport of soot are neglected, but this approach is justified, since the fraction of fuel carbon converted to soot is small for most fuels [17]. In this model the only effect of the soot particles is an increase of radiation heat transfer. Radiation in the streamwise direction is neglected, and a one dimensional radiant flux at the fuel surface is computed. An optically thin approximation simplifies the radiation terms in the

energy equation, and the equations are solved by numerical methods. From measurements of soot volume fraction in Chapters 2 and 3, the optical thickness of the soot layer is small even for very sooty fuels,  $\tau < 0.1$ . In the model a spectrally gray, homogeneous medium with a constant absorption coefficient throughout the boundary layer is assumed. The value of the absorption coefficient should be based on conditions near the flame zone, because most of the radiant energy from the combusting boundary layer is emitted near the flame zone.

## 4.2 Forced Flow Combustion

### 4.2.1 Analysis

As in the previous studies of a combusting boundary layer [26-32], assumptions include unity Lewis number, transport properties independent of composition, and no dissipation. A single step reaction for chemical changes is given by



The equations used to model the flow are the conservation equations for mass, momentum, enthalpy, and species

$$\frac{\partial(\rho u)}{\partial x} + \frac{\partial(\rho v)}{\partial x} = 0 \quad (4-2a)$$

$$\rho u \frac{\partial u}{\partial x} + \rho v \frac{\partial u}{\partial y} = \frac{\partial}{\partial y} \left( \mu \frac{\partial u}{\partial y} \right) \quad (4-2b)$$

$$\rho u \frac{\partial h}{\partial x} + \rho v \frac{\partial h}{\partial y} = \frac{\partial}{\partial y} \left( \frac{k}{c_p} \frac{\partial h}{\partial y} \right) + \dot{q}''' - \frac{\partial q_R}{\partial y} \quad (4-2c)$$

$$\rho u \frac{\partial Y_i}{\partial x} + \rho v \frac{\partial Y_i}{\partial y} = \frac{\partial}{\partial y} \left( \rho D \frac{\partial Y_i}{\partial y} \right) + \dot{m}_i''' \quad (4-2d)$$

where  $h = \int_{T_\infty}^T c_p dT$ . The one-dimensional radiative flux is given by

$$q_R = 2B_w E_3(\tau) - 2B_\delta E_3(\tau_\delta - \tau) + 2 \int_0^{\tau_\delta} \delta e_b(x, t) E_2(|\tau - t|) dt \quad (4-3a)$$

and its derivative is

$$-\frac{2q_R}{2y} = 2B_w E_2(\tau) + 2B_\delta E_2(\tau_\delta - \tau) + \int_0^{\tau_\delta} \delta e_b(x, t) E_1(|\tau - t|) dt - 4e_b(\tau) \quad (4-3b)$$

where  $\tau = \kappa y$ . In equation (4-3a) the first term,  $2B_w E_3(\tau)$ , is the radiant energy leaving the fuel surface, which is attenuated due to absorption by the medium. The remaining terms represent the incident energy from the distant wall and the combusting boundary layer. The first two terms in equation (4-3b) represent absorption in an elemental volume of energy originated at the fuel surface and the distant wall. The last term denotes energy emitted by the elemental volume. The boundary conditions are

$$\text{at } x = 0 \text{ or } y \rightarrow \infty, \quad u = u_\infty, \quad h = 0, \quad Y_{ox} = Y_{ox, \infty} \quad (4-4a)$$

$$\text{at } y = 0, \quad u = 0, \quad \dot{m}_p L_p = \frac{k}{c_p} \frac{\partial h}{\partial y} - q_R \quad (4-4b)$$

$$h = h_w, \quad \dot{m}_p = -\rho D \frac{\partial Y_f / \partial y}{Y_{ft} - Y_{fw}} \quad (4-4c)$$

The source terms  $\dot{m}_1'''$  and  $\dot{q}'''$  in equations (4-2c) and (4-2d) can be eliminated by defining the Shvab-Zeldovich variables

$$\gamma = -h/Q_p \nu_{ox} M_{ox} - Y_{ox} / \nu_{ox} M_{ox} \quad \text{and} \quad \beta = Y_f / \nu_f M_f - Y_{ox} / \nu_{ox} M_{ox} \quad (4-5)$$

$$\text{since} \quad \frac{\dot{q}'''}{Q_p \nu_{ox} M_{ox}} = - \frac{\dot{m}_f'''}{\nu_f M_f} = - \frac{\dot{m}_{ox}'''}{\nu_{ox} M_{ox}}$$

The fuel mass fraction changes along the wall, because the variation of radiation does not follow the same similarity form as the conduction heat transfer to the wall. Since we assume constant and equal specific heats for all species, the enthalpy at the wall and  $\gamma_w$  are constant in this analysis. Normalized Shvab-Zeldovich variables have the form

$$J_\gamma = \frac{\gamma - \gamma_\infty}{\gamma_w - \gamma_\infty} \quad \text{and} \quad J_\beta = \frac{\beta - \beta_\infty}{\beta_{wr} - \beta_\infty} \quad (4-6)$$

where  $\beta_{wr}$  indicates the value at the wall when radiation is neglected. For a given fuel the value of  $\beta_{wr}$  is known, since the mass fraction of fuel at the wall without radiation is given by

$$Y_{fwr} = [Y_{ft} B - Y_{ox,\infty} (\nu_f M_f / \nu_{ox} M_{ox})] / (1+B) \quad (4-7)$$

As in previous studies [27,28], the mass consumption number,

$$r_p = Y_{ox,\infty} \nu_f M_f / Y_{fwr} \nu_{ox} M_{ox} \quad (4-8)$$

represents the ratio of the relative available oxygen to the stoichiometrically required oxygen. From the definition of the enthalpy and equations (4-5) and (4-6), expressions for the enthalpy and dimensionless temperature are

$$h/h_w = D_c - (D_c - 1)J_\gamma, \quad y \leq y_{f1} \quad (4-9a)$$

$$h/h_w = - (D_c - 1)J_\gamma + D_c(1 + 1/r_p)J_\beta, \quad y \geq y_{f1}$$

$$\theta = 1 + (\theta_w - 1)(h/h_w) \quad (4-9b)$$

A relation between density and temperature is required and  $\rho T = \text{constant}$  is used.

The transformation from the  $(x, y)$  coordinates to a new system  $(\xi, \eta)$  is based on the similarity variables of the forced convective flame without radiation. The variables

$$\eta = \frac{\text{Re}_x^{1/2}}{2x} \int_0^y \rho/\rho_\infty dy \quad \text{and} \quad \xi = 2 \kappa x / \text{Re}_x^{1/2}$$

are introduced. Since the boundary layer thickness,  $\delta$ , is approximately proportional to  $x/\text{Re}_x^{1/2}$ ,  $\xi$  is proportional to its optical thickness. Equation (4-2a) is satisfied by introducing the stream function,  $\psi$ , as

$$\partial\psi/\partial y = \rho u / \rho_\infty, \quad \partial\psi/\partial x = -\rho v / \rho_\infty \quad (4-11)$$

The transformed stream function is taken to be

$$\psi = (\nu_\infty u_\infty x)^{1/2} f(\xi, \eta) \quad (4-12)$$

where the prime denotes a derivative with respect to  $\eta$ . If equations (4-2) and (4-4) are expressed in terms of the normalized Shvab-Zeldovich variables, the coordinate transformation yields



$$f''' + ff'' = \xi \left( f' \frac{\partial f}{\partial \xi} - f'' \frac{\partial f}{\partial \xi} \right) \quad (4-13a)$$

$$J_{\gamma}'' + \text{Pr}fJ_{\gamma}' = \text{Pr}\xi \left( f' \frac{\partial J_{\gamma}}{\partial \xi} - J_{\gamma}' \frac{\partial f}{\partial \xi} \right) - \frac{\xi^2 \theta}{N_R (\theta_w - 1) (D_c - 1)} \frac{\partial Q_R}{\partial \tau} \quad (4-13b)$$

$$J_{\beta}'' + \text{Pr}fJ_{\beta}' = \text{Pr}\xi \left( f' \frac{\partial J_{\beta}}{\partial \xi} - J_{\beta}' \frac{\partial f}{\partial \xi} \right) \quad (4-13c)$$

$$f'(\xi, 0) = 0, \quad J_{\gamma}'(\xi, 0) = 1 \quad (4-14a)$$

$$BJ_{\beta}'(\xi, 0) = \text{Pr} (B+1 - BJ_{\beta}(\xi, 0)) \left( f(\xi, 0) + \xi \frac{\partial f(\xi, 0)}{\partial \xi} \right) \quad (4-14b)$$

$$BJ_{\gamma}'(\xi, 0) = \text{Pr} \left( f(\xi, 0) + \xi \frac{\partial f(\xi, 0)}{\partial \xi} \right) - \frac{B\xi Q_R(\xi, 0)}{N_R (\theta_w - 1) (D_c - 1)} \quad (4-14c)$$

$$f'(\xi, \infty) = 2, \quad J_{\gamma}(\xi, 0) = 0, \quad J_{\beta}(\xi, 0) = 0 \quad (4-14d)$$

where  $N_R = \kappa k_{\infty} / \sigma T_{\infty}^3$  and  $\tau = \kappa y = \xi \int_0^{\eta} \rho / \rho_{\infty} d\eta$

The usual interpretation of  $N_R$  as the ratio of heat transfer by conduction to optically thick radiation does not apply, since the optical thickness of the boundary layer is small. However, the group  $N_R / \xi^2$  is a measure of the relative role of conduction versus optically thin radiation. The group  $N_R / \xi^2$  is rewritten as

$$\frac{N_R}{\xi^2} \sim \frac{k_{\infty} T_{\infty} / \delta}{4\kappa \sigma T_{\infty}^4 \delta}$$

where  $\delta \sim x / \text{Re}_x^{1/2}$ . The numerator corresponds to conduction, and the denominator represents the energy flux emitted by a one-dimensional medium without self-absorption.

The optically thin approximation neglects the absorption by the

medium of its own emitted radiation. This assumption is valid for  $\tau \ll 1$ . The exponential integrals,  $E_2(\tau)$  and  $E_3(\tau)$ , are approximated by

$$E_2(\tau) \approx 1 + O(\tau) \quad \text{and} \quad E_3(\tau) \approx \frac{1}{2} - \tau + O(\tau^2) \quad (4-15)$$

The substitution of equations (4-15) in equation (4-3a) yields

$$q_R(\xi, \tau) = B_w(1-2\tau) - B_\delta(1-2\tau_\delta + 2\tau) + 2 \int_0^\tau e_b(\xi, t) dt - 2 \int_{\tau_\delta}^{\tau_\delta} e_b(\xi, t) dt \quad (4-16)$$

Differentiation of equation (4-16) with respect to  $\tau$  gives

$$-\frac{\partial q_R}{\partial \tau} = 2B_w + 2B_\delta - 4e_b(\xi, \tau) \quad (4-17)$$

For gray diffuse surfaces the radiosity at the fuel slab and edge of the boundary layer are respectively

$$B_w = \sigma T_w^4 - (1-\epsilon_w) q_R(\xi, 0)/\epsilon_w \quad \text{and} \quad B_\delta = \sigma T_{ex}^4 \quad (4-18)$$

When equations (4-16) and (4-17) are substituted into equations (4-13) and (4-14), the problem is reduced to finding the solution of three coupled differential equations for  $f$ ,  $J_\gamma$ , and  $J_\beta$ .

From equation (4-12) the local and total pyrolysis rates in nondimensional form are

$$-\frac{2\dot{m}(x) \text{Re}^{1/2}}{\rho_\infty u_\infty} = f(\xi, 0) + \xi \frac{\partial f(\xi, 0)}{\partial \xi} \quad (4-19)$$

$$-\frac{\dot{M}_p(x) \text{Re}_x^{1/2}}{\rho_\infty u_\infty x} = f(\xi, 0) \quad (4-20)$$

where  $\dot{M}_p = \int_0^{x^*} \dot{m}_p(x) dx$ . The surface heat flux by conduction and the surface fuel mass fraction are obtained from equations (4-9) and (4-6) respectively

$$q_c = -\left(\frac{k}{c_p} \frac{\partial h}{\partial y}\right)_w = \rho_\infty u_\infty h_w \text{Re}_x^{-1/2} (D_c - 1) J'_Y(\xi, 0) / 2\text{Pr} \quad (4-21)$$

$$\frac{Y_{fw}}{Y_{fwr}} = (1+r_p) J_\beta(\xi, 0) - r_p \quad (4-22)$$

Thus,  $J'_Y(\xi, 0)$  represents a dimensionless conduction heat flux, and  $J_\beta(\xi, 0)$  indicates a surface mass fraction relative to  $Y_{fwr}$ . Equations (4-13) and (4-14) describe a combusting boundary layer without radiation at  $\xi = 0$ . Thus, the deviation of surface values and gradients with the streamwise coordinate indicates a change from the nonradiative solution.

#### 4.2.2 Results and Discussion

The equations are solved by finite difference methods. Two-point backward differences replace the  $\xi$ -derivative, i.e.  $\partial f / \partial \xi = (f_m - f_{m-1}) / \Delta \xi$ , to give a set of coupled ordinary equations at each streamwise station. An iterative, finite difference method developed by Newman [55] is used to solve this system of non-linear, ordinary differential equations. The boundary conditions at infinity are imposed at some finite location,  $\eta = \eta_\infty$ . After the equations are

linearized on the basis of a trial solution, the derivatives are replaced by finite central differences. The resulting set of linear algebraic equations can be readily solved, because the coefficient matrices have a tri-diagonal structure. In an iterative process, a new solution is used as the trial solution to obtain a second approximation, and the process is repeated. Solutions are computed for a Prandtl number of 0.73 and a wall emissivity of unity.

An increase in the distant wall temperature increases the nondimensional total pyrolysis rate, as shown in Fig. 4-1. With the distant wall at the ambient temperature,  $\theta_{ex} = 1$ ,  $-f(\xi, 0)$  decreases in the streamwise direction. The positive values of  $Q_R(\xi, 0)$  indicate the fuel surface loses more energy in its radiant interchange with the surroundings than the radiant energy it gains from the combusting boundary layer. The effects of hot surroundings on a compartment fire are simulated by increasing  $\theta_{ex}$ . If the temperature of the distant wall equals the temperature of the fuel surface,  $\theta_{ex} = 2$ , the net radiation heat transfer is toward the fuel surface ( $Q_R(\xi, 0)$  is negative), and  $-f(\xi, 0)$  increases with the streamwise coordinate. The radiation from the combusting layer to the fuel surface increases with  $\xi$  as the thickness of the boundary layer grows. Equations (4-13) and (4-14) describe a combusting boundary layer without radiation when  $\xi = 0$ . A nonradiative solution for  $-f(\xi, 0)$  is a horizontal line through the value at  $\xi = 0$ . In Fig. 4-1 the deviation of  $-f(\xi, 0)$  from a horizontal line indicates a change from the nonradiative solution. As shown in Fig. 4-2, the dimensionless surface heat flux by conduction,  $-J'_Y(\xi, 0)$ , decreases due to the higher pyrolysis rate

XBL 811-12821

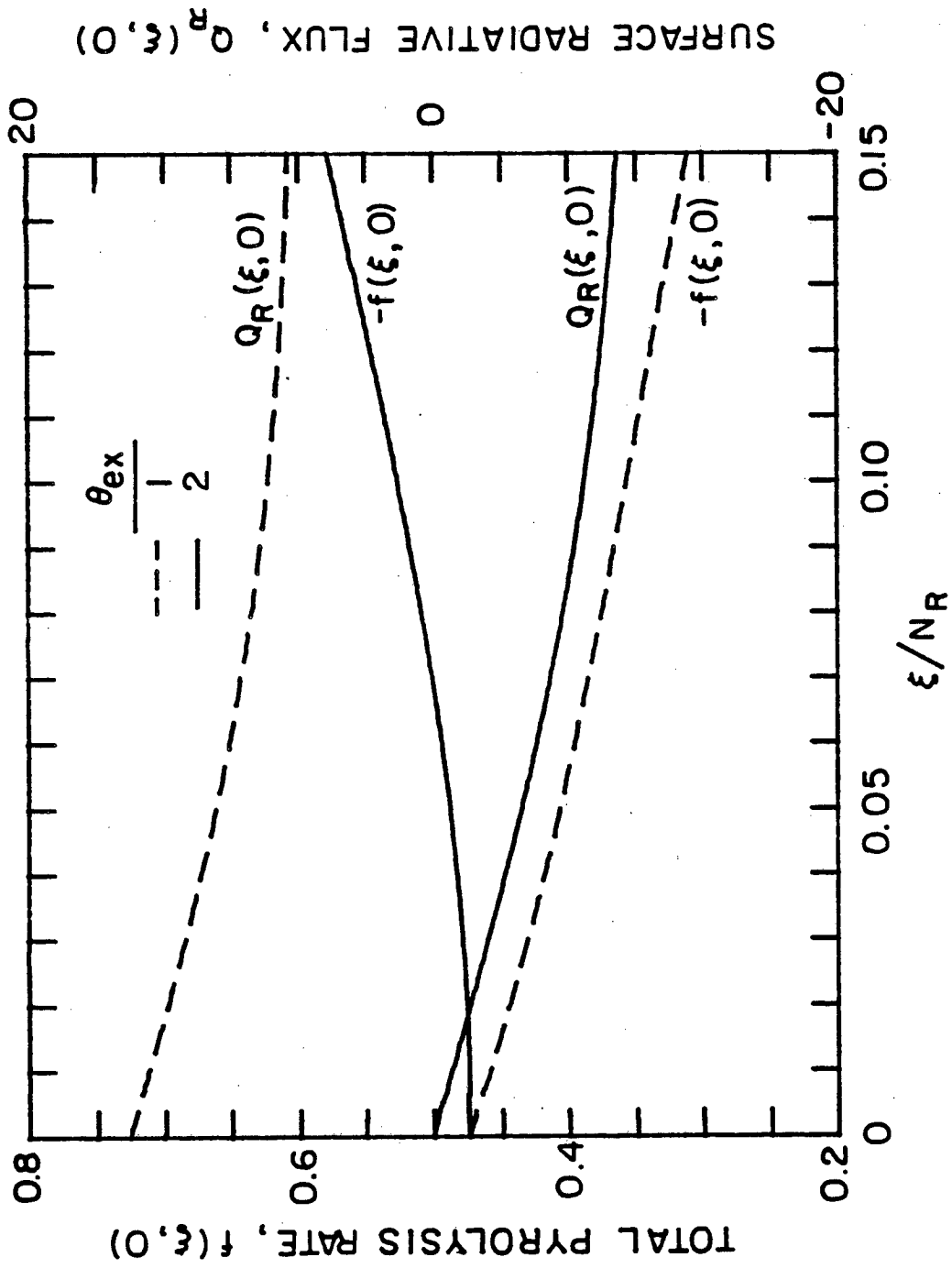


Fig. 4-1

XBL8111-12622

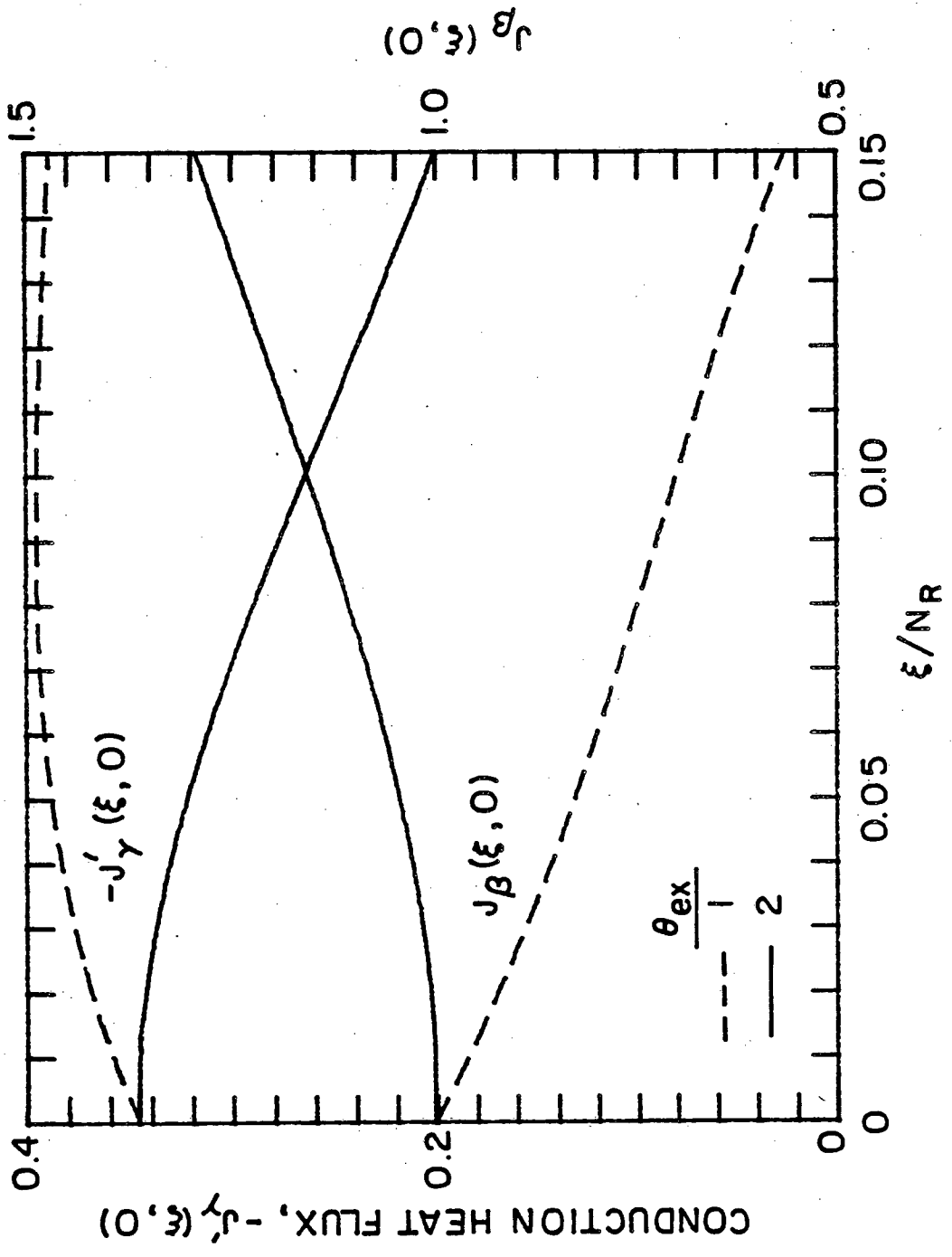
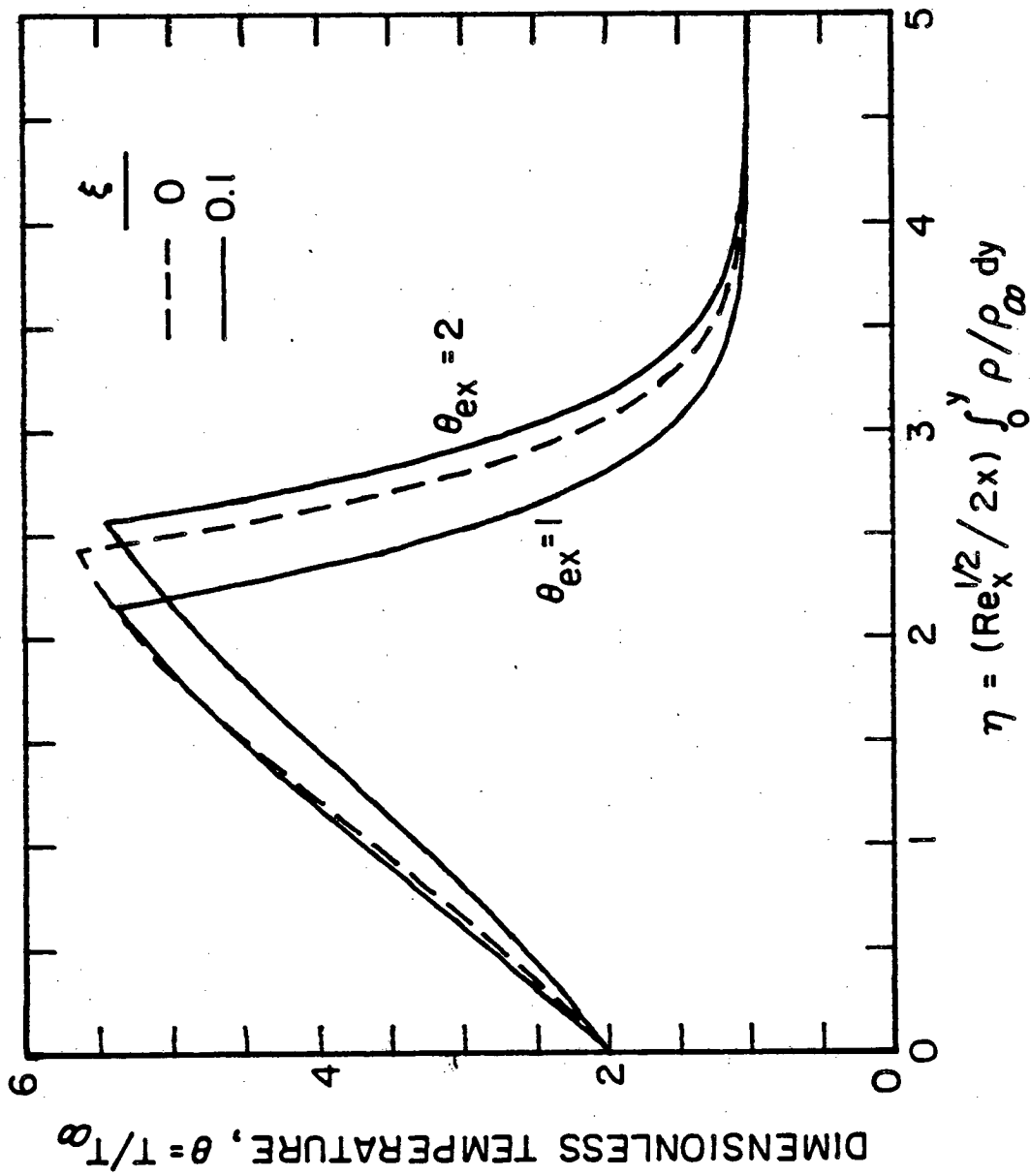


Fig. 4-2

associated with a net radiative flux into the fuel surface for  $\theta_{ex} = 2$ . The changes in the conduction surface heat flux oppose the effects of the net radiative flux. The curves of  $J_{\beta}(\xi, 0)$  represent the surface fuel mass fraction relative to  $Y_{fwr}$ .

As shown in Fig. 4-3, radiation from the flame decreases the flame temperature in the streamwise direction. The flame location moves inward for  $\theta_{ex} = 1$  and outward for  $\theta_{ex} = 2$ . The profiles at  $\xi = 0$  are the similarity solution without radiation. The movement of the flame can be explained as follows. The assumption of a single step reaction requires the fuel and oxygen to diffuse into the flame at relative rates determined by the stoichiometric ratio. In the streamwise direction  $Y_{fw}$  decreases for  $\theta_{ex} = 1$ , which gives a larger value of the relative available oxygen,  $Y_{ox,\infty} / Y_{fw}$ , to the stoichiometrically required oxygen. The flame location moves inward to compensate. In addition the decrease in the pyrolysis rate below the value corresponding to no radiation enhances the inward movement. A similar explanation applies for the outward movement with  $\theta_{ex} = 2$ .

For low values of  $D_c$  and  $N_R$  the dimensionless total pyrolysis rate,  $-f(\xi, 0)$ , decreases with  $\xi$ , because the net radiation heat transfer at the fuel surface is toward the surroundings ( $Q_R(\xi, 0)$  is positive), as shown in Fig. 4-4 and 4-5. The opposite trends are obtained for the higher values of  $D_c$  and  $N_R$ , where the net radiation heat transfer into the surface is the same order of magnitude as conduction heat flux. As the dimensionless heat of combustion,  $D_c$ , increases the flame temperature and flame radiation increase due to a larger heat release. A large value of  $N_R$  corresponds to a high value



XBL8III-12823

Fig. 4-3



XBL 6111-12824

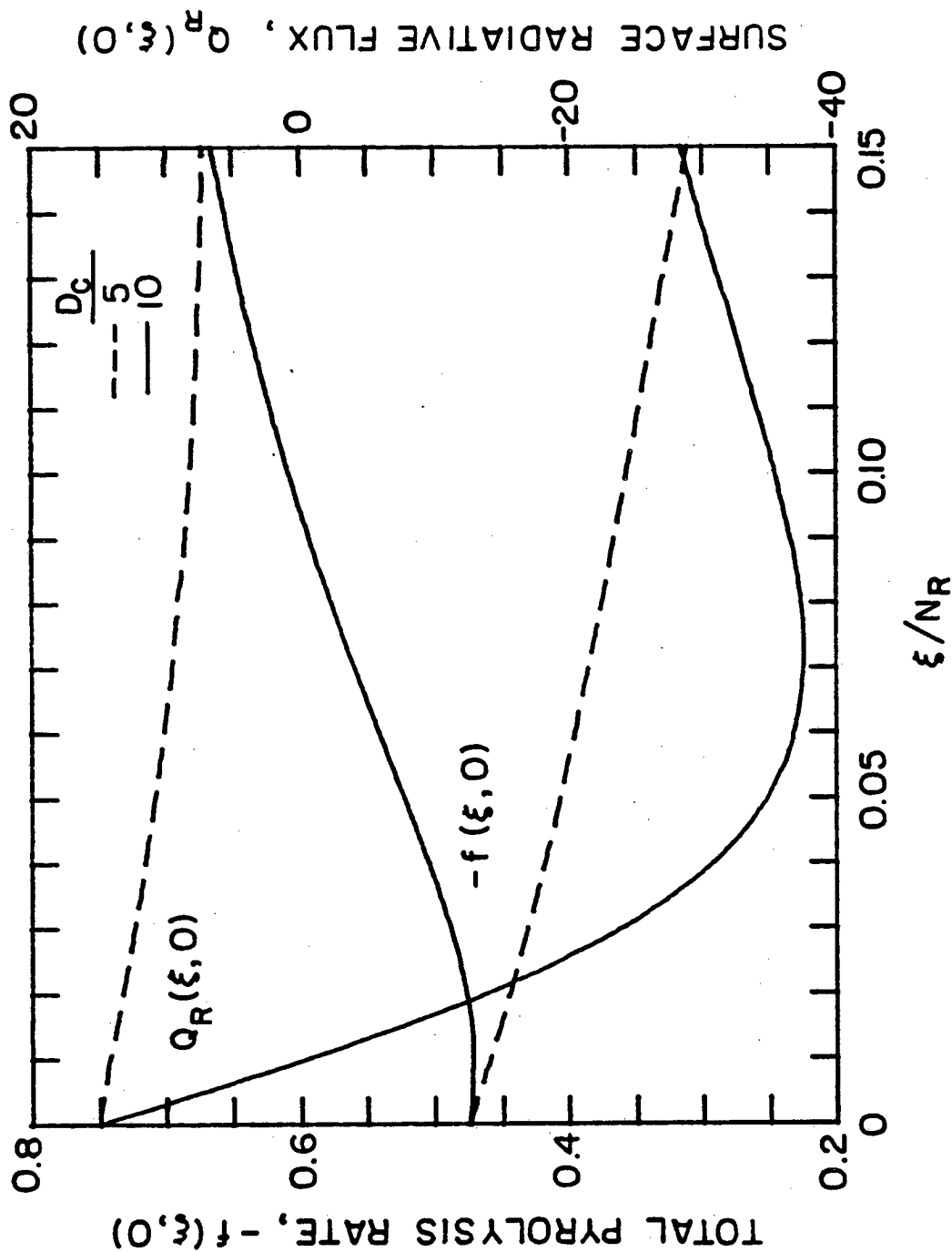


Fig. 4-4

XBL811-12825

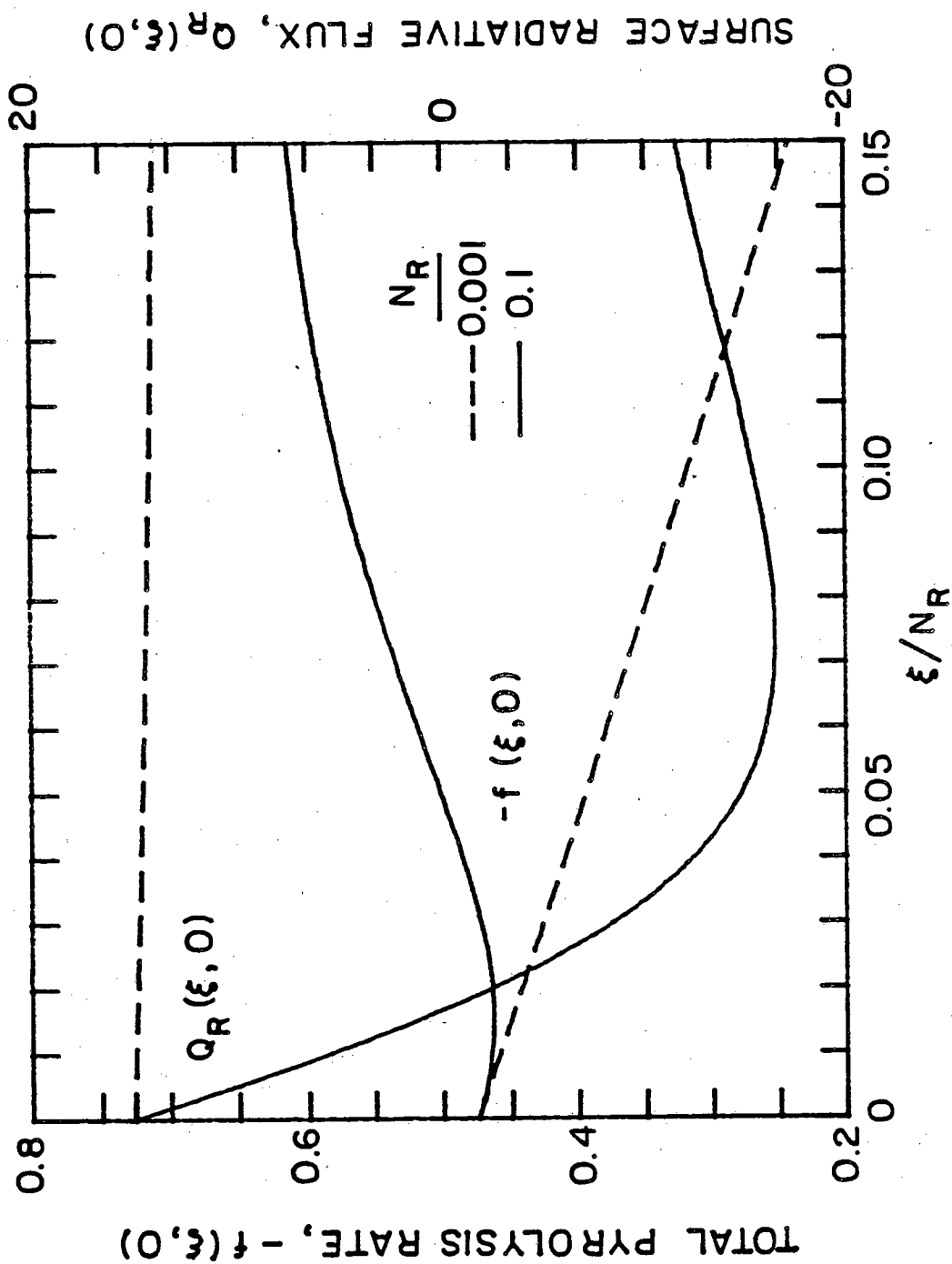


Fig. 4-5

of the absorption coefficient,  $\kappa$ , and a large amount of radiation from the flame. For large  $\xi$  the radiation from the combusting layer decreases due to the reduced flame temperature.

The optically thin approximation is even valid for high values of the absorption coefficient. If the coordinate transformation (4-10) is inverted, the optical thickness of the boundary layer is recovered as

$$\tau_{bl} = \kappa \delta = \xi \int_0^{\eta_\delta} \theta d\eta \quad (4-23)$$

The optical depth varied from very small values at the beginning of the slab to an order of 0.1 at the end for the highest value of  $N_R$ .

The parameters  $B$  and  $r_p$  affect the radiation heat transfer to the surface slightly. However,  $-f(\xi, 0)$  is strongly dependent on the value of  $B$  as found in the nonradiative solution.

The effects of radiation on excess pyrolyzate, combustible gases which are not consumed in the flames that produced them, are significant. The excess pyrolyzate is obtained by calculating the downstream flux of the fuel between the slab and the flame

$$\dot{M}_e(x) = \int_0^y f_1 (\rho u Y_f)_x dy \quad (4-24)$$

Transforming equation (4-24) to the  $(\xi, \eta)$  coordinate system and normalizing on  $\dot{M}_p(x)$  in equation (4-20) yields the unburned fraction of the total pyrolyzate from 0 to  $\xi$ ,

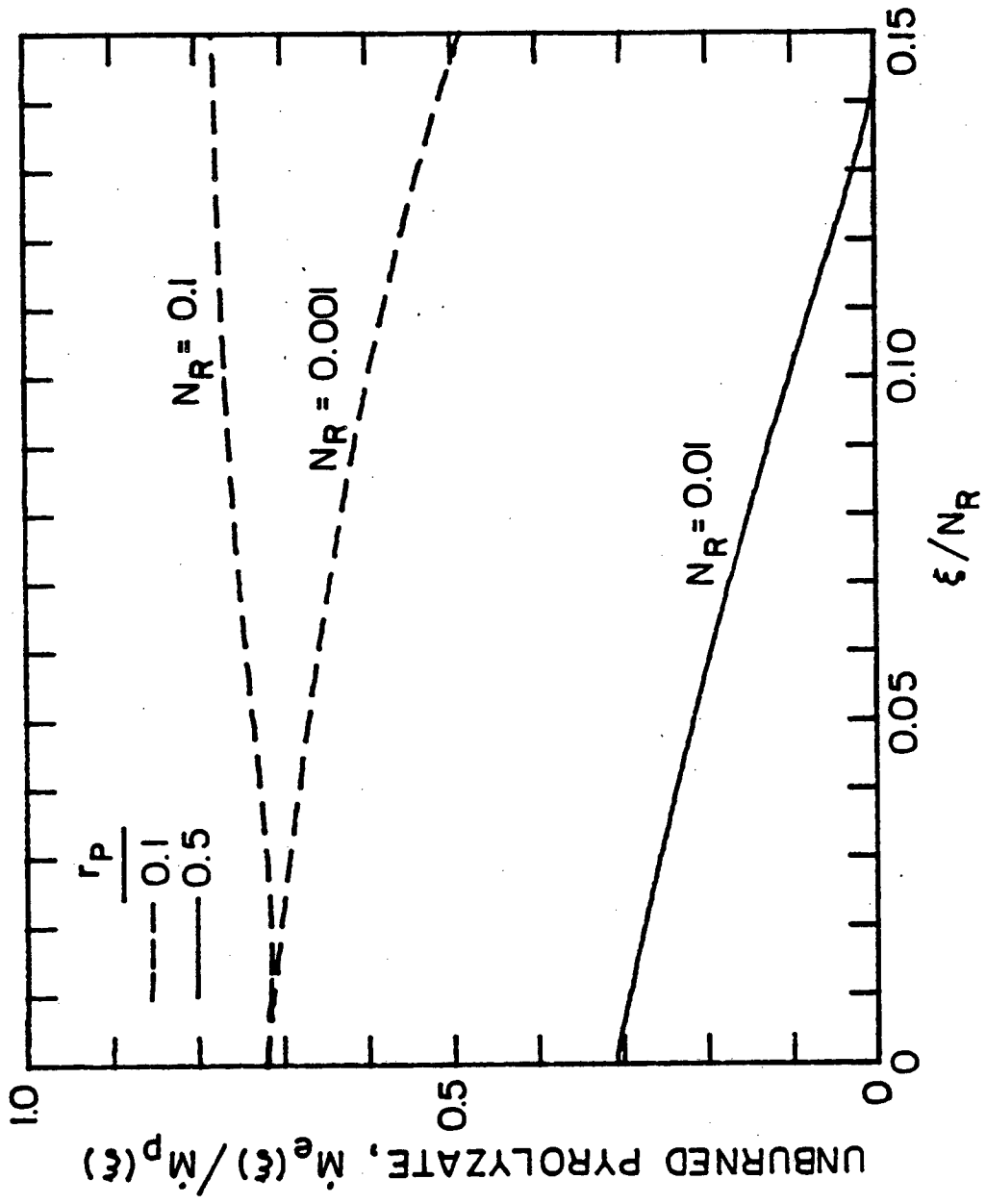
$$\frac{\dot{M}_e(\xi)}{\dot{M}_p(\xi)} = \frac{B}{B+r_p+1} \left[ -r_p + \frac{r_p f(\xi, \eta_{fl})}{f(\xi, 0)} - \frac{1+r_p}{f(\xi, 0)} \int_0^{\eta_{fl}} f' J_Y d\eta \right] \quad (4-25)$$

In previous studies [27,28] the dominant parameter affecting the excess fraction of total pyrolyzate was the mass consumption number,  $r_p$ . This strong dependence on  $r_p$  applies with the inclusion of radiation from the results shown in Fig. 4-6. The excess fraction varies with  $\xi$ , since  $Y_{fw}$  and the flame location changes as previously explained for the temperature profiles in Fig. 4-3. For the higher value of  $N_R$  the mass fraction of fuel at the wall increases with the streamwise coordinate and the flame location moves away from the surface. The excess fraction increases, since it contains the integral of the fuel-velocity product between the fuel surface and the flame location. The opposite trends appear for the lower values of  $N_R$ . Similarly, the excess fraction increases with increasing  $D_c$  or  $\theta_{ex}$ . As in previous studies [27,28], an increase in the excess fraction occurs with an increase in  $B$ .

### 4.3 Free Flow Combustion

#### 4.3.1 Analysis

The only change in the conservation equations (4-2) is the addition of the buoyancy term in the momentum equation to describe a laminar combusting boundary layer in free flow. The boundary conditions remain unchanged, except for the value of velocity at the edge of the boundary layer, which is rewritten as  $u(\xi, 0) = 0$ .



XBL 811-12826

Fig. 4-6

The transformation variables,  $\xi$  and  $\eta$ , and the transformed stream function are chosen as

$$\eta = (Gr_x^{1/4}/2^{1/2}x) \int_0^y \rho/\rho_\infty dy \quad (4-26)$$

$$\xi = 2^{1/2} \kappa x Gr_x^{-1/4} \quad (4-27)$$

$$\psi = 2^{3/2} v_\infty Gr_x^{1/4} f(\xi, \eta) \quad (4-28)$$

Since the boundary layer thickness,  $\delta$ , is proportional to  $x/Gr_x^{1/4}$  if radiation is neglected,  $\xi$  is again proportional to the optical thickness of the boundary layer. The conservation equations and the boundary conditions in this new coordinate system are

$$f''' + 3ff'' - 2(f')^2 + \frac{\theta-1}{\theta_w-1} = \xi \left( f' \frac{\partial f'}{\partial \xi} - f'' \frac{\partial f}{\partial \xi} \right) \quad (4-29a)$$

$$J_\gamma'' + 3PrfJ_\gamma' = Pr\xi \left( f' \frac{\partial J_\gamma}{\partial \xi} - J_\gamma' \frac{\partial f}{\partial \xi} \right) - \frac{\xi^2 \theta}{N_R(\theta_w-1)(D_c-1)} \frac{\partial Q_R}{\partial \tau} \quad (4-29b)$$

$$J_\beta'' + 3PrfJ_\beta' = Pr\xi \left( f' \frac{\partial J_\beta}{\partial \xi} - J_\beta' \frac{\partial f}{\partial \xi} \right) \quad (4-29c)$$

$$f'(\xi, 0) = 0, \quad J_\gamma(\xi, 0) = 1 \quad (4-30a)$$

$$BJ_\gamma'(\xi, 0) = Pr \left( 3f(\xi, 0) + \frac{\partial f(\xi, 0)}{\partial \xi} \right) - \frac{B \xi Q_R(\xi, 0)}{N_R(\theta_w-1)(D_c-1)} \quad (4-30b)$$

$$BJ_\beta'(\xi, 0) = Pr \left( 3f(\xi, 0) + \xi \frac{\partial f(\xi, 0)}{\partial \xi} \right) (B+1-BJ_\gamma(\xi, 0)) \quad (4-30c)$$

$$u(\xi, \infty) = 0, \quad J_\gamma(\xi, \infty) = 0, \quad J_\beta(\xi, \infty) = 0 \quad (4-30d)$$

The equations contain the same number of parameters that appear in

forced flow:  $B$ ,  $r_p$ ,  $D_c$ ,  $N_R$ ,  $\xi$ ,  $Pr$ ,  $\theta_{ex}$ ,  $\theta_w$ , and  $\epsilon_w$ .

The following expressions for the local pyrolysis rate, total pyrolysis rate, and conduction heat flux at the surface replace equations (4-19) through (4-21) for free flow:

$$\frac{-2^{1/2} \dot{m}_p(x) Gr_x^{-1/4} x}{\rho_\infty v_\infty} = 3f(\xi, 0) + \xi \frac{\partial f(\xi, 0)}{\partial \xi} \quad (4-31)$$

$$\frac{-\dot{M}_p(x) Gr_x^{-1/4}}{2^{3/2} \rho_\infty v_\infty} = f(\xi, 0) \quad (4-32)$$

$$q_c = -\left( \frac{k}{c_p} \frac{\partial h}{\partial y} \right)_w = \rho_\infty D_\infty Gr_x^{1/4} (D_c - 1) J'_\gamma(\xi, 0)/x \quad (4-33)$$

Equations (4-22), (4-23), and (4-25) are still valid for the surface fuel mass fraction, optical thickness, and the excess pyrolyzate.

#### 4.3.2 Results and Discussion

The free flow solution is more sensitive to changes in  $D_c$  than forced flow, because the vertical velocity in free flow depends on the temperature profile. In free flow a change in the flame temperature causes a change in the fluid motion. An increase in  $D_c$  raises the flame temperature, which increases the buoyancy forces and thus the upward fluid velocity. Since the increase in fluid motion enhances the heat transfer to the fuel surface, a larger increase in the pyrolysis rate occurs, as shown in Fig. 4-7. The values of  $-f(\xi, 0)$  represents the nonradiative, similarity solution, and depend weakly on  $D_c$  unlike forced flow.

In Fig. 4-8 the dimensionless pyrolysis rate,  $-f(\xi, 0)$ , decreases in the streamwise direction over the entire range of  $N_R$  unlike the

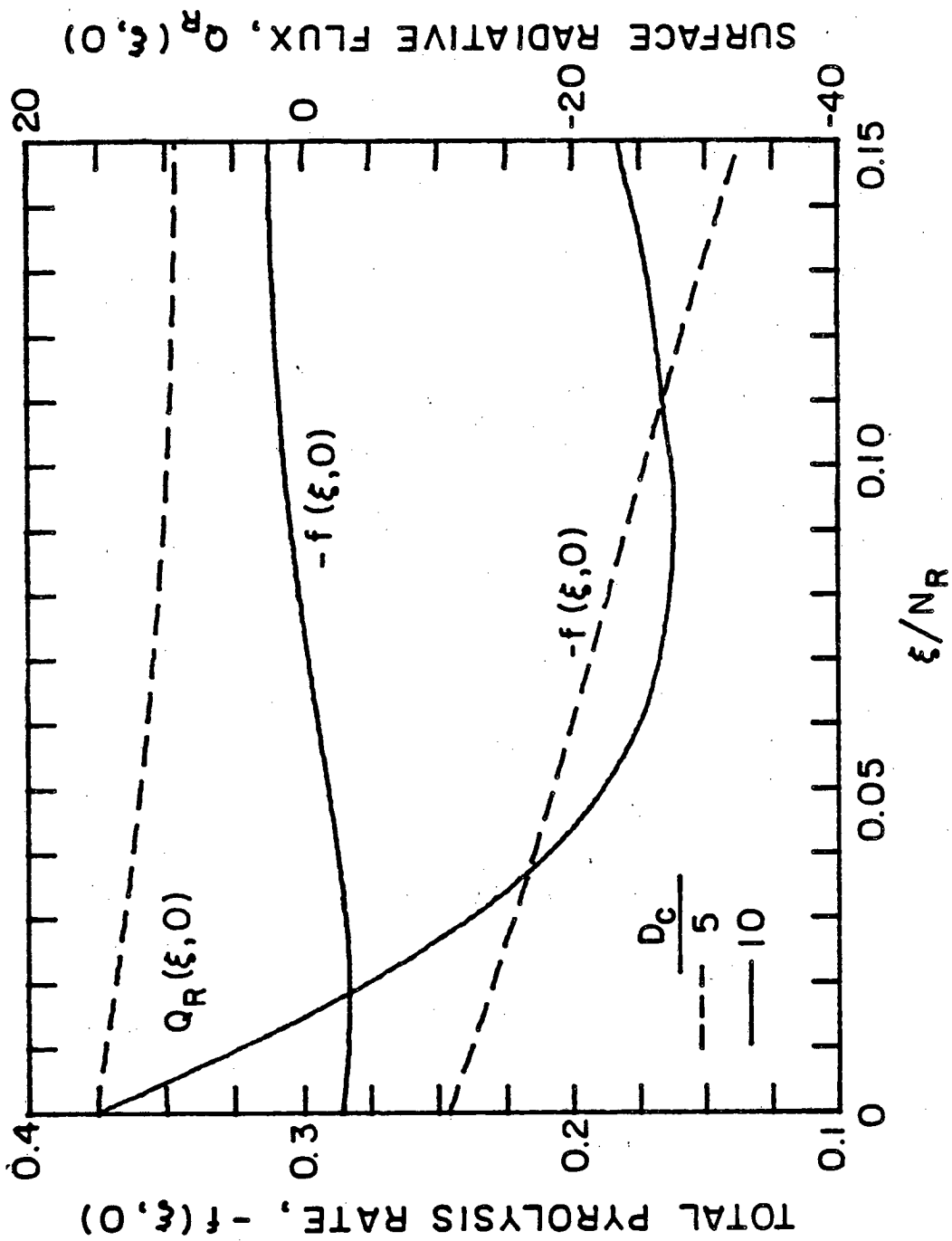
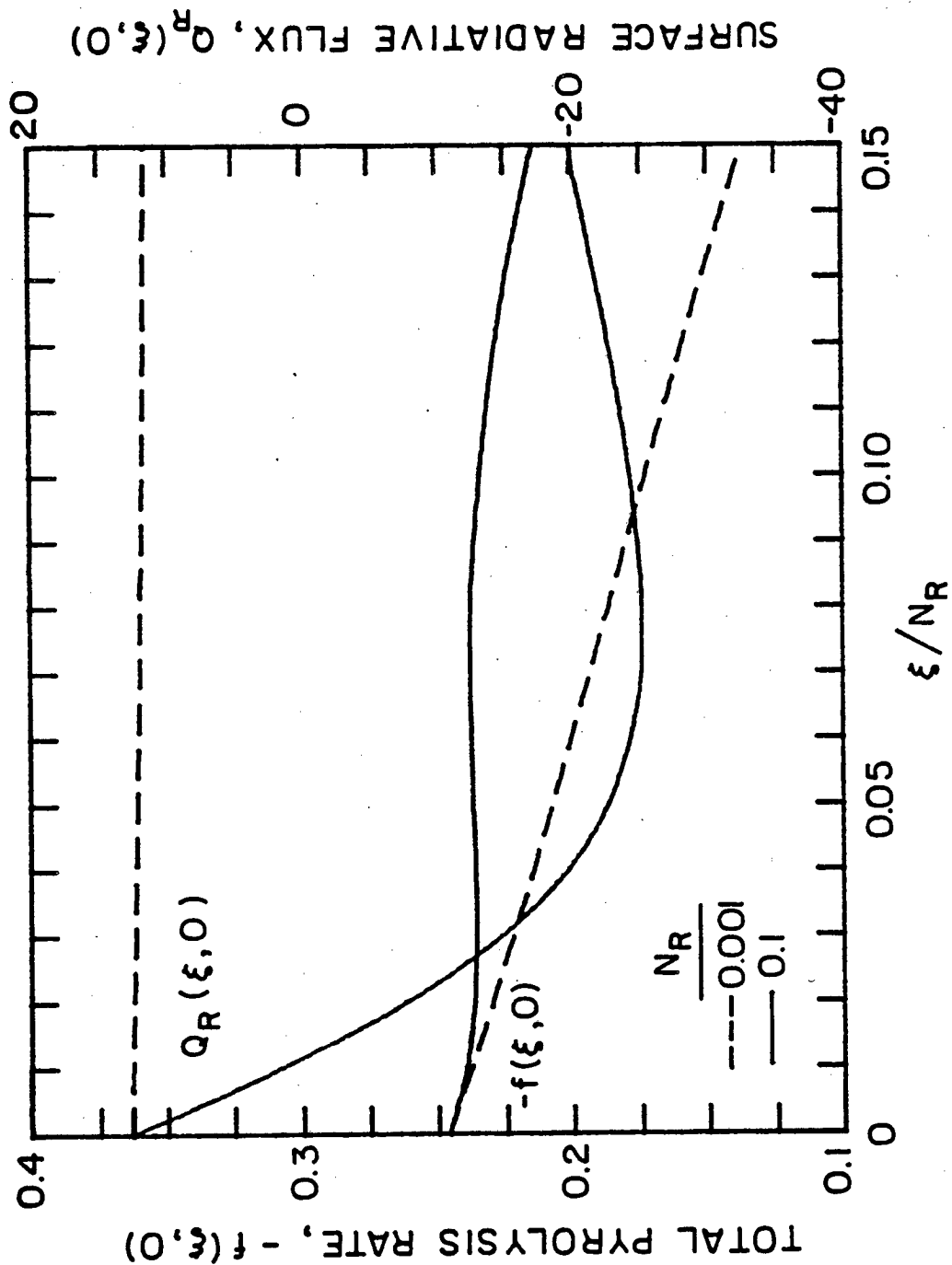


Fig. 4-7

XBL 8111-12827





XBL 8111-12828

Fig. 4-8

results for forced flow in Fig. 4-5. Again the coupling between the velocity and temperature changes the solution. An increase in  $N_R$ , which corresponds to an increase in the absorption coefficient, increases the radiation from the flame and thereby lowers the flame temperature. With the decrease in flame temperature, the upward fluid velocity and the conduction heat transfer to the fuel surface are reduced. Thus an increase in  $N_R$  gives a smaller increase in the pyrolysis rate than the result in forced flow.

Without radiation the excess fraction of total pyrolyzate is larger for free flow than forced flow [27]. This result applies with the inclusion of radiation as seen by comparing Figs. 4-9 (free flow) and 4-6 (forced flow). The external radiant flux,  $N_R$  and  $D_c$  influence the excess fraction as in forced flow.

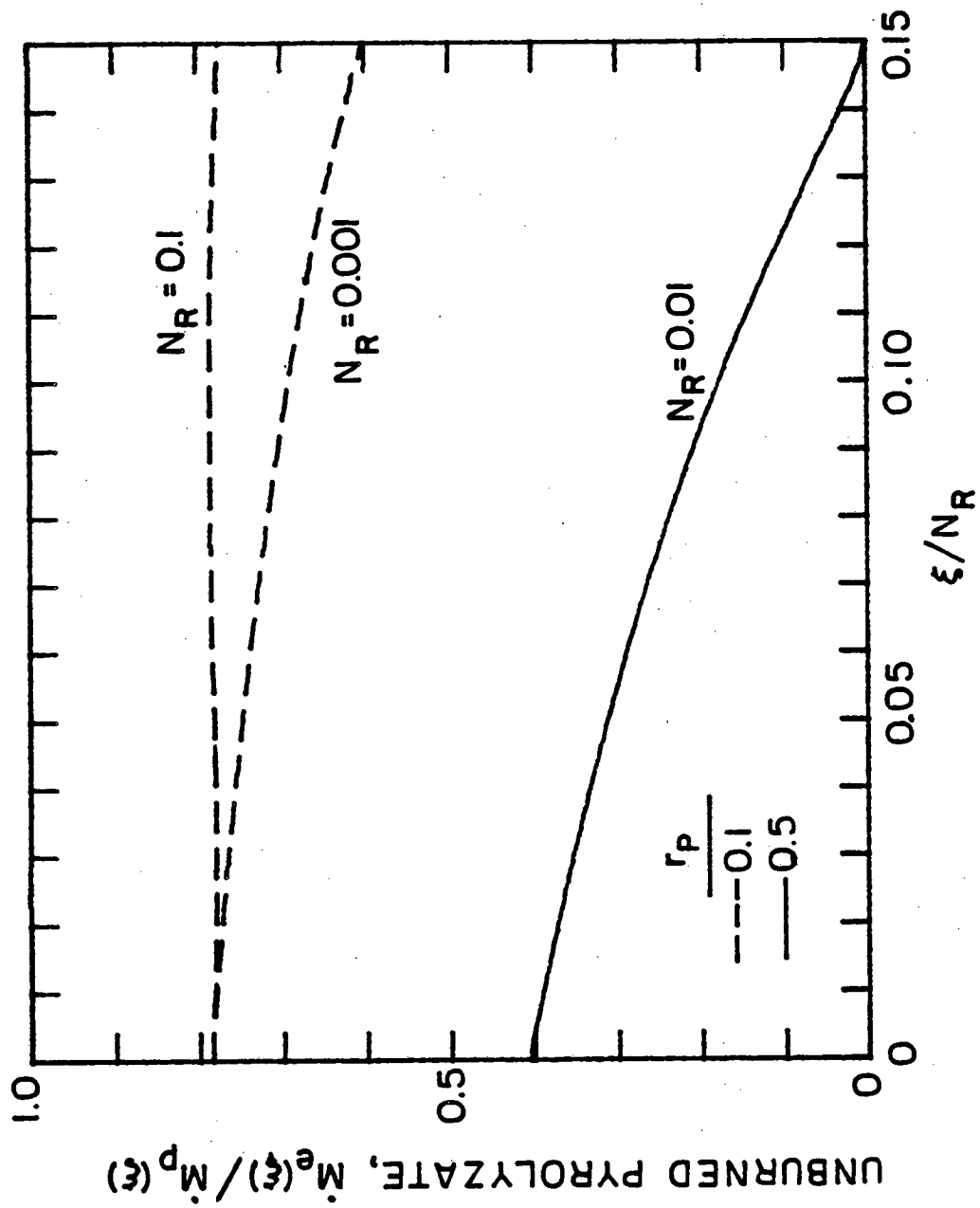
#### 4.4 Comparison With Experiment

##### 4.4.1 Evaluation of the Absorption Coefficient

The primary interest of this study is the use of soot volume fraction measurements to predict flame radiation. From Mie scattering theory [47], a dimensionless group which measures the radiative properties of soot is the size parameter

$$\alpha = 2\pi r/\lambda \quad (4-34)$$

where  $r$  is the particle radius and  $\lambda$  is the wavelength of radiation. A characteristic wavelength of soot emission is the wavelength of the maximum of the Planck blackbody function, which is usually 2 microns



XBL8111-12829

Fig. 4-9

or larger for fires. As a result, the characteristic size parameter,  $\alpha$ , is usually much less than unity for typical values of  $r_{\max}$  given in Chapters 2 and 3. This condition,  $\alpha \ll 1$ , allows a simplification of the general Mie scattering theory known as the Rayleigh absorption limit for small particles, for which the absorption coefficient [56,57] is given by

$$\kappa = \tau(\bar{\lambda}) = 36\pi F_a(\bar{\lambda})f_v/\bar{\lambda} \quad (4-35)$$

$$\bar{\lambda}T_s = c_2/3.6 = 0.40 \text{ cm K} \quad (4-36)$$

where  $T_s$  is the soot temperature and  $c_2$  is Planck's second constant ( $c_2 = 1.44 \text{ cm-K}$ ). All the dependence of mean optical properties,  $m=n(1-ik)$ , is contained in

$$F_a(\lambda) = \frac{n^2 k}{[n^2 - (nk)^2 + 2]^2 + 4n^4 k^2} \quad (4-37)$$

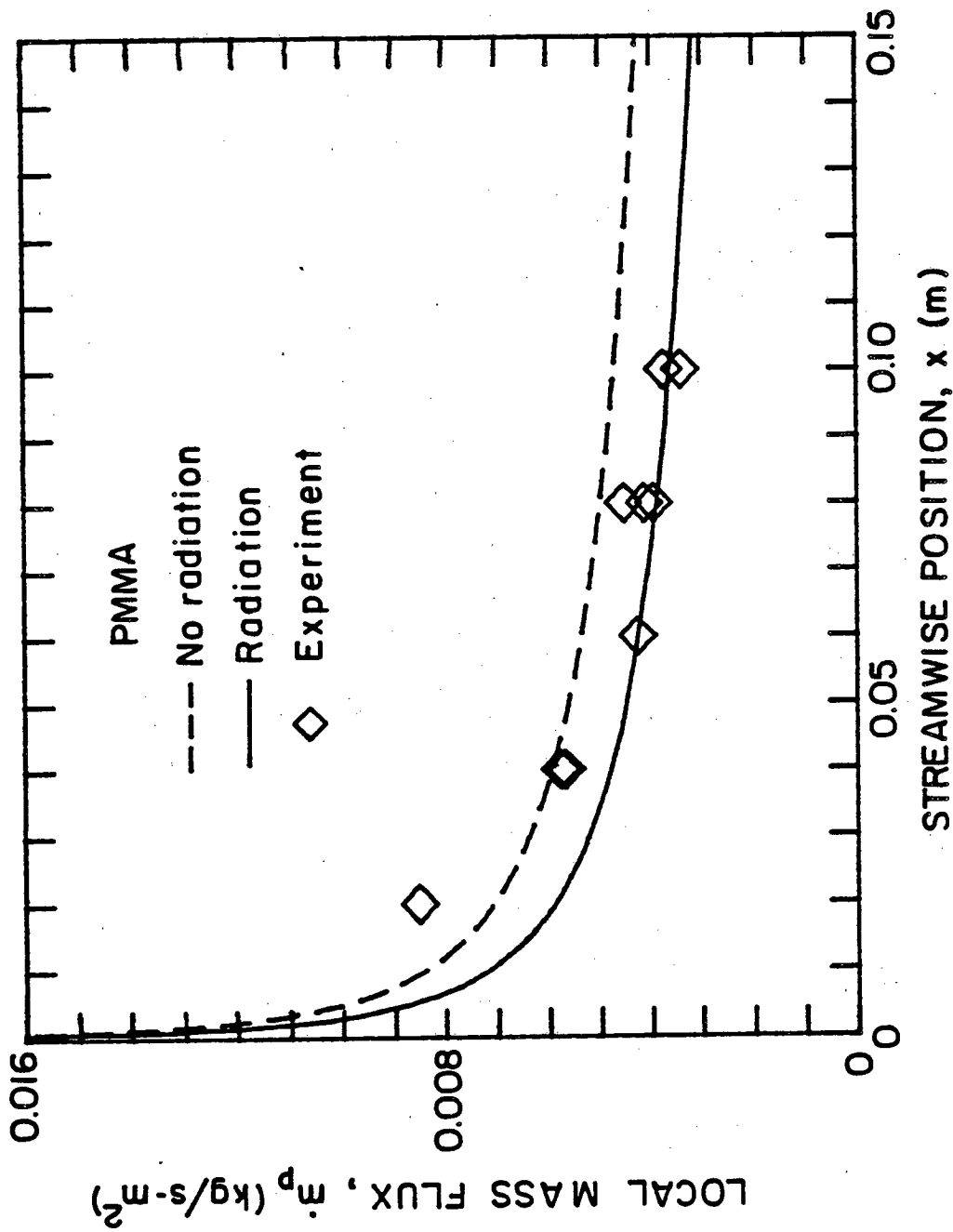
An important simplification from equation (4-35) is the distribution of particle sizes is unimportant. At the visible wavelengths of the transmission measurements, this condition,  $\alpha \ll 1$ , was not satisfied, and the complete Mie scattering theory was used in the extinction analysis in Chapters 2.

#### 4.4.2 Pyrolysis Rates

During the experiments described in Chapter 2 and 3, the regression rate of a pyrolyzing slab of PMMA can be measured for both forced and free flow. To determine the regression rate, a parallel laser beam is partially blocked by the fuel surface. As the fuel surface recedes, it blocks less of the laser beam. The regression rate is given as the rate the back surface of the fuel slab has been moved to maintain a constant reading of the transmitted intensity for the partially blocked beam. A new sample of PMMA is burned for a measurement at each height.

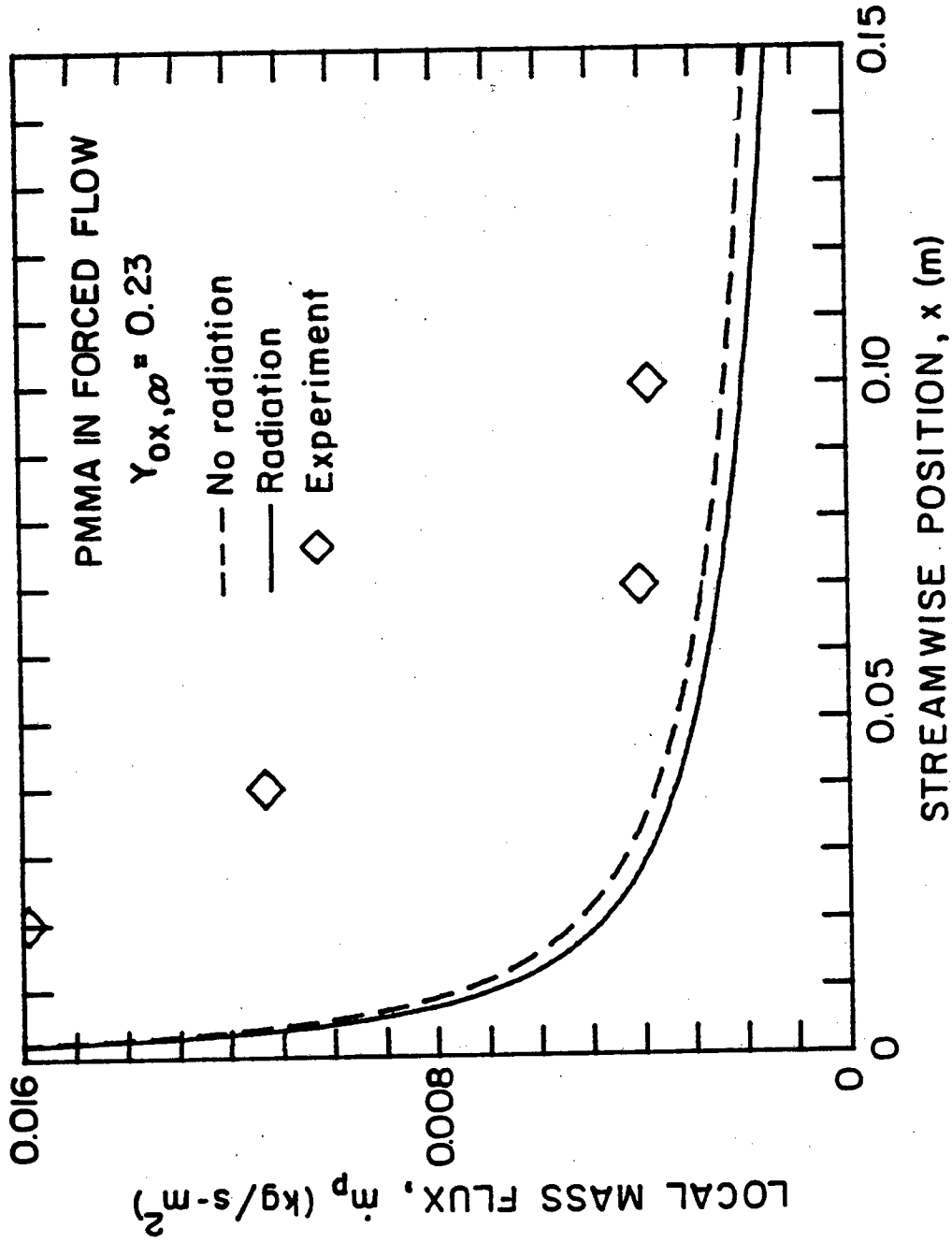
In free flow the net radiation heat transfer is away from the fuel surface for PMMA, which reduces the pyrolysis rate as shown in Fig. 4-10. The value of the product  $\rho u$  is chosen to obtain agreement between theory and experiment at  $x = 10$  cm. Fuel and transport properties used in the calculation are given in Appendix C. The temperature of the fuel surface is about 660 K, which is much higher than the temperature of the surroundings at room temperature. The fuel surface loses more radiant energy to the surroundings than it gains from the combusting layer. In forced flow the effects of surface emission are less as shown in Fig. 4-11. The same value of  $\rho u$  as in the free flow solution is used. Surface emission dominates the radiant heat transfer in PMMA fires for a free stream mass oxygen fraction of air.

The data points at  $x = 2$  and 4 cm in Fig. 4-11 are much greater than the theoretical solutions. There are several possible causes. With the large pyrolysis rates near the leading edge, the resulting



XBL 8111-12 830

Fig. 4-10



XBL 8111-12831

Fig. 4-11

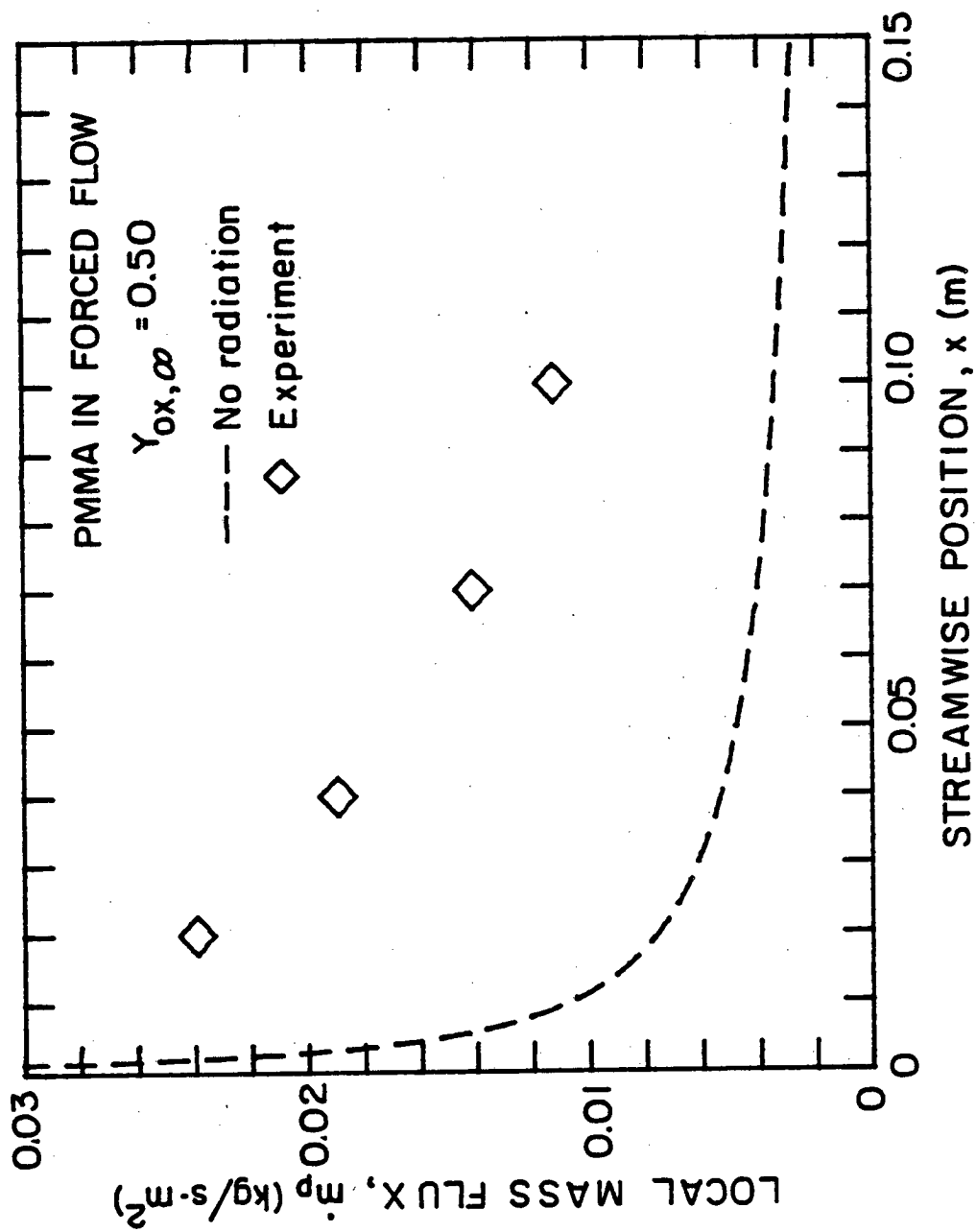
curvature of the sample surface in the streamwise direction may cause significant deviations from the flat plate solutions. Since the fuel sample is placed 5 cm behind the exit of the contraction in the wind tunnel, a hydrodynamic boundary layer forms before the leading edge of the fuel sample. Finally, the boundary layer approximations neglecting diffusion in the streamwise direction are not valid near the leading edge.

At  $Y_{\text{ox},\infty} = 0.50$ , the net radiative heat transfer is toward the fuel surface, which causes the experimental pyrolyzing surface mass flux rates to be greater than the nonradiative solution as shown in Fig. 4-12. Attempts to predict this surface mass flux with radiation failed, because convergence is not achieved at such high blowing velocities by the iterative process. In the model the blowing velocity is so large the boundary layer is blown away if  $f(\xi, 0)$  is near  $-1.05$ . For a forced flow combusting boundary layer without radiation, Emmons [26] reported the maximum blowing velocity is given by  $f(0) = -1.2386$ . The result given by Emmons does not rigorously apply with radiation.

#### 4.5 Conclusions

Nine parameters describe a combusting, laminar boundary layer in both forced and free flow: the convective mass transfer number,  $B$ ; the mass consumption number  $r_p$ ; the dimensionless heat of combustion,  $D_c$ ; the radiation parameter,  $N_R$ ; the optical thickness,  $\xi$ ; the Prandtl number,  $Pr$ ; the dimensionless fuel surface temperature,  $\theta_w$ ; the dimensionless distant wall temperature,  $\theta_{e_x}$ ; and the fuel surface





XBL8111-12832

Fig. 4-12

emissivity,  $\epsilon_w$ . The parameters  $D_c$ ,  $N_R$ , and  $\xi$  strongly influence the radiation heat transfer from the flame to the fuel surface. An increase in  $D_c$ ,  $N_R$ , or the intensity of an external radiant flux increases the pyrolysis rate. The free flow solution is more sensitive to changes in  $D_c$  and  $N_R$  than the forced flow results. As in previous studies the pyrolysis rate depends strongly on  $B$ , and the dominant parameter affecting excess pyrolyzate, combustible gases escaping downstream at the top of the top of the fuel slab, is  $r_p$ . Although the excess pyrolyzate depends on the length of the fuel surface through  $\xi$ , this dependence is weaker than the dependence on  $r_p$ .

## Chapter 5: CONCLUSIONS

5.1 Summary of Results

An experimental study of soot volume fraction and particle size in a two dimensional, laminar, combusting boundary layer has revealed the detailed structure of the soot layer. A multiwavelength laser transmission technique is used to probe a soot layer on the fuel rich side of the flame zone. The large variation of soot volume fraction among different hydrocarbon fuels indicates the chemical structure of the fuel is important. The ranking of fuels by soot volume fraction is preserved among small pool fires [15-19,53] and laminar combusting boundary layers in forced and free flow. Soot volume fraction increases monotonically with mass fraction of oxygen. For oxygen mass fractions from 0.23 to 0.50, soot volume fraction is most sensitive to a change in the ambient oxygen mass fraction at  $Y_{\text{ox},\infty} = 0.23$ . The particle size does not change significantly across the soot layer or with oxygen concentration. Since the particle size does not vary with streamwise position, little agglomeration of soot particles occurs in these small scale fires.

In an analysis of a combusting boundary layer with radiation, the pyrolysis rate depends on nine dimensionless parameters and the intensity of an external flux. Since  $D_c$ , a dimensionless heat of combustion, controls the flame temperature, the amount of radiation emitted by the combusting layer depends strongly on  $D_c$ . In addition,  $\xi$ , an optical thickness of the boundary layer, and  $N_R$ , a radiation parameter, affect emission from the combusting layer. A dimensionless wall temperature,  $\theta_w$ , and wall emissivity,  $\epsilon_w$ , control surface

emission. As in previous models without radiation, the boundary layer combustion is influenced by  $B$ , a mass transfer number,  $r_p$ , a mass consumption number, and  $Pr$ , Prandtl number. The pyrolysis rate depends strongly on  $B$ , while the amount of combustible gases escaping downstream is dominated by  $r_p$ . The dependence on  $Pr$  is weak. The effects of hot surroundings in a compartment fire has been introduced through an incident radiative flux. Since the boundary layer is optically thin, most of this incident radiation strikes the fuel surface. An increase in the radiative heat flux is partially offset by an associated decrease in the convective heat flux. The flame temperature and surface fuel mass fraction vary with streamwise position, unlike combustion without radiation.

## 5.2 Future Work

Temperature measurements by thermocouples and velocity measurements by laser Doppler anemometry are planned to give a more detailed picture of these combusting boundary layers. Temperature measurements will determine the location of the soot layer relative to the temperature distribution. From detailed velocity profiles, streamlines in the flow field may be determined.

Although the flame extended past the fuel surface all the measurements were confined to a region above the fuel surface. Measurements in the flame extended region would indicate the streamwise location where the soot formation process is overcome by soot oxidation. The extent of the combusting gas downstream of the pyrolyzing slab has been predicted by Kinoshita and Pagni [28,56]. Since the mass consumption number is small for all the fuels tested,

the excess pyrolyzate,  $\dot{M}_e(x)/\dot{M}_p(x)$ , is large. A free standing wick is preferred for measurements in the flame extended region, because soot is deposited on the inert wall following the fuel in the present study.

Numerous theories have been postulated in studies of soot formation, but the basic mechanisms are still unknown. Measurements which determine soot volume fractions for various fuels provide badly needed data. The well characterized nature of the combusting boundary layer provides an attractive system for future work in soot formation modeling.

## REFERENCES

1. Michin, S. T., "Luminous Stationary Flames: the Quantitative Relationship between Flame Dimensions at the Sooting Point and Chemical Composition, with Special Reference to Petroleum Hydrocarbons," Journal of the Institute of Petroleum Technologists, Vol. 17, 1931, pp. 102-120
2. Clarke, A. E., Hunter, T. G., and Garner, F. H., "The Tendency to Smoke of Organic Substances on Burning. Part I," Journal of the Institute of Petroleum Technologists, Vol. 32, May 1946, pp. 627-642
3. Glassman, I. and Yaccarino, P., "The Temperature Effect in Sooting Diffusion Flames," Eighteenth Symposium (International) on Combustion, pp. 1175-1183, The Combustion Institute, 1980
4. Glassman, I. and Yaccarino, P., "The Effect of Oxygen Concentration on Sooting Diffusion Flames," Combustion Science and Technology, Vol. 24, 1980, pp. 107-114
5. Kadota, T., Hiroyasu, H., and Farazandehmehr, A., "Soot Formation by Combustion of a Fuel Droplet in High Pressure Gaseous Environments," Combustion and Flame, Vol 29, pp. 67-75, 1977
6. Chakraborty, B. B. and Long, R., "The Formation of Soot and Polycyclic Aromatic Hydrocarbons in Diffusion Flames - Part One," Combustion and Flame, Vol. 12, pp. 226-236, 1968
7. Chakraborty, B. B. and Long, R., "The Formation of Soot and Polycyclic Aromatic Hydrocarbons in Diffusion Flames - Part Two," Combustion and Flame, Vol. 12, pp. 237-242, 1968
8. Jagoda, I. J., Prado, G., and Lahaye, J., "An Experimental Investigation into Soot Formation and Distribution in Polymer Diffusion Flames," Combustion and Flame, Vol. 37, 1980, pp. 261-274
9. D'Alessio, A., Di Lorenzo, A., Sarofim, A. F., Beretta, F., Masi, S., and Venitozzi, C., "Soot Formation in Methane-Oxygen Flames," Fifteenth Symposium (International) on Combustion, p. 1427, 1974
10. D'Alessio, A., Di Lorenzo, A., Borghese, A., Beretta, F., and Masi, S., Sixteenth Symposium (International) on Combustion, p. 695, 1977

11. Kent, J. H., Jander, H., and Wagner, H. Gg., "Soot Formation in Laminar Diffusion Flame," Eighteenth Symposium (International) on Combustion, The Combustion Institute, 1980. pp. 1117-1126
12. Haynes, B. S., and Wagner, H. Gg., "Sooting Structure in a Laminar Diffusion Flame," Ber. Bunsenges. Phys. Chem., Vol. 84, 1980, pp.499-506
13. Haynes, B. S., Jander, H., and Wagner, H. Gg., "Optical Studies of Soot-Formation Processes in Premixed Flames," Ber. Bunsenges. Phys. Chem., Vol. 84, 1980, pp. 585-592
14. Chang, P. H. P. and Penner, S. S., "Particle Size Measurements in Flames Using Light Scattering; Comparison with Diffusion-Broadening Spectroscopy," J. Quant. Spectrosc. Radiat. Transfer, Vol. 25, pp. 105-110, 1981
15. Pagni, P. J., and Bard, S., "Particulate Volume Fractions in Diffusion Flames," Seventeenth Symposium (International) on Combustion, pp. 1017-1028, The Combustion Institute, 1978.
16. Bard, S., and Pagni, P. J., "Comparison of Laser Induced Fluorescence and Scattering in Pool Fire Diffusion Flames," J. Quant. Spec. Rad. Trans., Vol. 25, 1981, pp.453-461
17. Bard, S., "Diffusion Flame Particulate Volume Fractions," Ph.D. Dissertation, Mechanical Engineering Dept., University of California, Berkeley, 1980
18. Bard, S., and Pagni, P. J., "Carbon Particulate in Small Pool Fire Flames," ASME Journal of Heat Transfer, Vol. 103, pp.357-362, 1981
19. Bard, S., and Pagni, P. J., "Spatial Variation of Soot Volume Fractions in Pool Fire Diffusion Flames," submitted to Combustion and Flame
20. Asano, S. and Yamamoto, G., "Light Scattering by a Spheroidal Particle." Applied Optics, Vol. 14, No. 1, p. 29, 1975
21. Palmer, H. B., and Cullis, C.F., "The Formation of Carbon From Gases," The Chemistry and Physics of Carbon, Vol. 1, Marcel Dekker, New York, p. 265
22. Wagner, H. Gg., "Soot Formation in Flames, A Review," Seventeenth Symposium (International) on Combustion, p. 3, The Combustion Institute, 1979

23. Bittner, J. D., and Howard, J. B., "Role of Aromatics in Soot Formation," in Alternative Hydrocarbon Fuels: Combustion and Kinetics, Progress in Astronautics and Aeronautics, Vol. 62, pp. 335-358, Amer. Inst. of Aero. and Astro., New York, 1978
24. Markstein, G. H., "Radiative Properties of Plastic Fires," Seventeenth Symposium (International) on Combustion, pp. 1053-1062, Combustion Institute, 1978
25. Santo, G. and Tamanini, F., "Influence of Oxygen Depletion on the Radiative Properties of PMMA Flames," Eighteenth Symposium (International) on Combustion, The Combustion Institute, 1980, pp. 619-631
26. Emmons, H. W., "The Film Combustion of Liquid Fuel," Z. angew. Math. Mech., Vol. 36, 1956, pp. 60-71
27. Pagni, P. J., and Shih, T. M., "Excess Pyrolyzate," Sixteenth Symposium (International) on Combustion, pp. 1329-1342, The Combustion Institute, 1976.
28. Kinoshita, C. M. and Pagni, P. J., "Laminar Wake Flame Heights," ASME Journal of Heat Transfer, Vol. 102, pp. 104-109, 1980
29. Kosden, F. J., Williams, F. A., and Buman, C., "Combustion of Vertical Cellulosic Cylinders in Air," Twelfth Symposium (International) on Combustion, pp. 253-264, The Combustion Institute, 1969
30. Kim, J. S., de Ris, J., and Kroesser, F. W., "Laminar Free-Convective Burning of Fuel Surfaces," Thirteenth Symposium (International) on Combustion, pp. 949-961, The Combustion Institute, 1971
31. Ahmad, T., and Faeth, G. M., "An Investigation of the Laminar Overfire Region Along Upright Surfaces," ASME Journal of Heat Transfer, Vol. 100, pp. 112-119, 1978
32. Groff, E. G., and Faeth, G. M., "Laminar Combustion of Vertical Free-Standing Fuel Surfaces," Combustion and Flame, Vol. 32, pp. 139-150, 1978
33. Cess, R. D., "Radiation Effects Upon Boundary Layer Flow of an Absorbing Gas," ASME Journal of Heat Transfer, Vol. 86, pp. 469-475, 1964
34. Viskanta, R., "Radiation Transfer and Interaction of Convection With Radiation Heat Transfer," in Advances in Heat Transfer, Vol. 3, Academic Press, New York, 1966



35. Oliver, C. C., and McFadden, P. W., "The Interaction of Radiation and Convection in the Laminar Boundary Layer," *Journal of Heat Transfer*, Vol. 88, pp. 205-213, 1966
36. Cess, R. D., "The Interaction of Thermal Radiation with Free Convection Heat Transfer," *Int. J. Heat Mass Transfer*, Vol. 9, pp. 1269-1277, 1966
37. Sparrow, E. M., and Cess, R. D., Radiation Heat Transfer, Augmented Edition, McGraw-Hill, New York, 1978
38. Arpaci, V. S., "Effect of Thermal Radiation on the Laminar Free Convection From a Heated Vertical Plate," *Int. J. Heat Mass Transfer*, Vol. 11, pp. 871-881, 1968
39. Lord, H. A., Arpaci, V. S., "Effect of Nongray Thermal Radiation on Laminar Forced Convection Over a Heated Horizontal Plate," *Int. J. Heat Mass Transfer*, Vol. 13, pp. 1737-1751
40. Tamanini, F., "A Numerical Model For the Prediction of Radiation Controlled Turbulent Wall Fires," *Seventeenth Symposium (International) on Combustion*, p. 1075, The Combustion Institute, 1978
41. Kinoshita, C. M. and Pagni, P. J., "Stagnation-Point Combustion With Radiation," *Eighteenth Symposium (International) on Combustion*, Combustion Institute, 1980, pp. 1415-1425
42. Sibulkin, M., Kulkarni, A. K., Annamalai, K., "Effects of Radiation on the Burning of Vertical Fuel Surfaces," *Eighteenth Symposium (International) on Combustion*, Combustion Institute, 1980, pp. 611-617
43. Han, James Tsung-Wu, "Boundary Layer Flow with Combustion and Thermal Radiation," Ph.D. Dissertation, Mechanical Engineering Dept., University of California, Berkeley
44. Liu, C. N., and Shih, T. M., "Laminar, Mixed-Convection, Boundary-Layer, Nongray-Radiative, Diffusion Flames," *ASME Journal of Heat Transfer*, Vol. 102, 1980, pp. 724-730.
45. Tien, C. L., and Lee, S. C., "Flame Radiation," *Progress in Energy and Combustion Science*, 1981, in press
46. de Ris, J., "Fire Radiation - A Review," *Seventeenth Symposium (International) on Combustion*, p. 1003, The Combustion Institute, 1979

47. Kerker, M., The Scattering of Light and Other Electromagnetic Radiation, Academic Press, 1969
48. Lee, S. C., and Tien, C. L., "Optical Constants of Soot in Hydrocarbon Flames," Eighteenth Symposium (International) on Combustion, Combustion Institute, 1980, pp. 1159-1166
49. Lee, S. C., and Tien, C. L., "Thermal Radiation of Spherical and Cylindrical Soot Particles," Paper No. 80-54, Western States Section of the Combustion Institute, Fall Meeting, 1980
50. Di Lorenzo, A., D'Alessio, A., Cincotti, V., Masi, S., Menna, P., and Ventitozzi, C., "UV Absorption, Laser-Excited Fluorescence and Direct Sampling in the Study of Formation of Polycyclic Aromatic Hydrocarbons in Rich CH/O Flames," Eighteenth Symposium (International) on Combustion, pp. 485-491, The Combustion Institute, 1980
51. Wersborg, B. L., Fox, L. K., and Howard, J. B., Combustion and Flame, Vol. 24, p. 1, 1975
52. Kashiwagi, T., Combustion Science and Technology, Vol. 21, p. 131, 1980
53. Lee, S. C., Ph.D. Dissertation, Mechanical Engineering Dept., University of California, Berkeley, 1981
54. Brown, G. L. and Roshko, A., "On Density Effects and Large Structures in Turbulent Mixing Layers," Journal of Fluid Mechanics, Vol. 64, 1974, pp. 775
55. Newman, J., "Numerical Solution of Coupled, Ordinary Differential Equations," Industrial and Engineering Chemistry Fundamentals, Vol 7, pp.514-517, 1968
56. Felske, J. D., and Tien, C. L., "Calculation of the Emissivity of Luminous Flames," Combustion Science and Technology, Vol. 7, pp. 25-31, 1973
57. Yuen, W. W., and Tien, C. L., "A Simple Calculation Scheme for Luminous Flame Emissivity," Sixteenth Symposium (International) on Combustion, p. 1481, The Combustion Institute, 1974
58. Kinoshita, C. M., Pagni, P. J., and Beier, R. A., "Opposed Flow Diffusion Flame Extensions," Eighteenth Symposium (International) on Combustion, pp. 1853-1860, The Combustion Institute, 1981
59. Perry, J. H., Chemical Engineers' Handbook, McGraw-Hill, New York, 1975

60. Obert, E. F., Internal Combustion Engines, International Textbook Co., Scranton, Penn., 1968
61. Varafrik, N. B., Tables of Thermophysical Properties of Liquids and Gases, Hemisphere Publishing Corp., distributed by John Wiley, 1975
62. Tewarson, A. and Pion, R. F., "A Laboratory-Scale Test Method for the Measurement of Flammability Parameters," Technical Report No. 22524, FMRC, Norwood, Mass., October 1977
63. Tewarson, A., "Experimental Evaluation of Flammability Parameters of Polymetric Materials, Technical Report No. 22524, RC79-T9, FMRC, Norwood, Mass., February 1979
64. Krishnamurthy, L. and Williams, F. A., "On The Temperatures of Regressing PMMA Surfaces," Combustion and Flame, Vol. 20, pp. 163-169, 1973

## Appendix A: EXTINCTION EFFICIENCY

For homogeneous, spherical carbon particles, the extinction efficiency,  $Q(\lambda, m, r)$  is given by the Mie scattering theory [47] as

$$Q(\lambda, m, r) = \frac{2}{\alpha^2} \sum_{n=1}^{\infty} (2n+1) [\operatorname{Re}(a_n) + \operatorname{Re}(b_n)] \quad (\text{A-1})$$

with

$$a_n = \frac{\psi_n(\alpha)\psi_n'(\beta) - \psi_n(\beta)\psi_n'(\alpha)}{\zeta_n(\alpha)\psi_n'(\beta) - m\psi_n(\beta)\zeta_n'(\alpha)}$$

and

$$b_n = \frac{m\psi_n(\alpha)\psi_n'(\beta) - \psi_n(\beta)\psi_n'(\alpha)}{m\zeta_n(\alpha)\psi_n'(\beta) - \psi_n(\beta)\zeta_n'(\alpha)}$$

where  $\beta = m\alpha$ , prime indicates derivative with respect to argument,

$$\psi(z) = \left(\frac{\pi z}{2}\right)^{\frac{1}{2}} J_{n+\frac{1}{2}}(z)$$

and

$$\zeta(z) = \left(\frac{\pi z}{2}\right)^{\frac{1}{2}} H_{n+\frac{1}{2}}^{(2)}(z)$$

with  $J_{n+\frac{1}{2}}(z)$  = half integral order Bessel functions of the first kind  
and  $H_{n+\frac{1}{2}}(z)$  = half integral order Hankel functions of the second kind.

The Mie theory extinction coefficient from equation (A-1) and the size distribution of equation (2-3) are substituted in equation (2-2). Numerical integration of equation (2-2) at fixed wavelengths yields an extinction coefficient which accounts for both scattering and absorption. The results are presented in Table A-1 in terms of a nondimensional extinction coefficient,

$$\tau'(\alpha_{\max}, \lambda, m) = \tau / N_0 r_{\max}^2 \quad (\text{A-2})$$

for the four wavelengths used in the experiments. If the characteristic size parameter is small,  $\alpha \ll 1$ , the absorption limit applies where  $\tau$  is independent of the size distribution and only depends on the optical properties of the particles. Then the ratio of  $\tau$ 's at two different wavelengths is given by

$$[\tau_i / \tau_j]_{\text{absorption}} = \lambda_j F_a(\lambda_i) / \lambda_i F_a(\lambda_j) \quad (\text{A-3})$$

where

$$F_a(\lambda) = \frac{n^2 k}{[n^2 - (nk)^2 + 2]^2 + 4n^4 k^2} \quad (\text{A-4})$$

In the large particle limit,  $\alpha \gg 1$ ,  $Q \rightarrow 2$  for all  $\lambda$ , so  $\tau_i / \tau_j \rightarrow 1$ . Pagni and Bard [15-19] suggested a normalized extinction coefficient defined as

$$\chi_{ij} = [\tau_i / \tau_j - 1] / [\tau_i / \tau_j - 1]_{\text{absorption}} \quad (\text{A-5})$$

Since the two laser beams are superimposed,  $L_i = L_j$ , so that

$$\tau_i/\tau_j = \ln(I/I_0)_i / \ln(I/I_0)_j \quad (\text{A-6})$$

Values of  $\chi_{ij}$  are listed as a function of  $r_{\max}$  in Table A-1 for the wavelength pairs used in the experiments.

From the measured ratios of transmitted and initial intensities,  $I/I_0$ , the experimental  $\chi_{ij}$  is calculated from equations (2-1), and (A-3) through (A-6). The most probable radius,  $r_{\max}$ , and  $\tau'$ , are obtained from Table A-1 based on the experimental  $\chi_{ij}$ . If  $\chi_{ij} > 1$ , two possible values of  $r_{\max}$  are found in Table A-1. For these cases, more than one wavelength pair is used to isolate the proper  $r_{\max}$ . Substitution of  $\tau'$  and the experimental  $\tau$  into equation (A-2) determines  $N_0$ . The soot volume fraction is obtained from equations (2-5). The values of  $\chi_{ij}$  and  $r_{\max}$  are known independent of the pathlength,  $L$ . Since  $L$  must be known to obtain  $\tau$ , the error in the measurement of  $L$  does affect the accuracy of  $N_0$  and  $f_v$ .

Table A-1. Nondimensional Extinction Coefficient,  $\tau'_j$ , and Normalized Extinction Coefficient Ratio,  $\chi_{ij}$ , Versus the Most Probable Radius with  $\lambda_1 = 0.4579 \mu\text{m}$ ,  $\lambda_2 = 0.4880 \mu\text{m}$ ,  $\lambda_3 = 0.5145 \mu\text{m}$ ,  $\lambda_4 = 0.6328 \mu\text{m}$ .

$\chi_{ij}$ , Versus the Most Probable Radius with  $\lambda_1 = 0.4579 \mu\text{m}$ ,  $\lambda_2 = 0.4880 \mu\text{m}$ ,  $\lambda_3 = 0.5145 \mu\text{m}$ ,  $\lambda_4 = 0.6328 \mu\text{m}$ .

$r_{\text{max}} (\mu\text{m})$	$\tau'_1$	$\tau'_2$	$\tau'_3$	$\tau'_4$	$\chi_{14}$	$\chi_{24}$	$\chi_{34}$
1.000D-03	1.501D-01	1.318D-01	1.217D-01	9.490D-02	1.002D+00	1.002D+00	1.003D+00
2.000D-03	3.014D-01	2.645D-01	2.442D-01	1.901D-01	1.007D+00	1.007D+00	1.007D+00
3.000D-03	4.554D-01	3.993D-01	3.683D-01	2.862D-01	1.018D+00	1.017D+00	1.016D+00
4.000D-03	6.136D-01	5.373D-01	4.951D-01	3.836D-01	1.033D+00	1.032D+00	1.031D+00
5.000D-03	7.777D-01	6.799D-01	6.255D-01	4.826D-01	1.053D+00	1.053D+00	1.050D+00
6.000D-03	9.496D-01	8.284D-01	7.608D-01	5.840D-01	1.078D+00	1.078D+00	1.074D+00
7.000D-03	1.131D+00	9.844D-01	9.022D-01	6.881D-01	1.109D+00	1.109D+00	1.103D+00
8.000D-03	1.325D+00	1.149D+00	1.051D+00	7.957D-01	1.146D+00	1.145D+00	1.137D+00
9.000D-03	1.532D+00	1.325D+00	1.208D+00	9.074D-01	1.187D+00	1.187D+00	1.177D+00
1.000D-02	1.756D+00	1.514D+00	1.376D+00	1.023D+00	1.233D+00	1.234D+00	1.222D+00
1.100D-02	1.999D+00	1.717D+00	1.556D+00	1.145D+00	1.283D+00	1.286D+00	1.271D+00
1.200D-02	2.261D+00	1.937D+00	1.749D+00	1.273D+00	1.335D+00	1.341D+00	1.324D+00
1.300D-02	2.544D+00	2.173D+00	1.956D+00	1.408D+00	1.389D+00	1.398D+00	1.379D+00
1.400D-02	2.849D+00	2.428D+00	2.179D+00	1.551D+00	1.442D+00	1.456D+00	1.436D+00
1.500D-02	3.177D+00	2.702D+00	2.418D+00	1.702D+00	1.493D+00	1.514D+00	1.493D+00
1.600D-02	3.527D+00	2.996D+00	2.674D+00	1.861D+00	1.541D+00	1.570D+00	1.549D+00
1.700D-02	3.898D+00	3.309D+00	2.948D+00	2.030D+00	1.584D+00	1.622D+00	1.602D+00
1.800D-02	4.288D+00	3.641D+00	3.238D+00	2.209D+00	1.621D+00	1.669D+00	1.652D+00
1.900D-02	4.697D+00	3.991D+00	3.545D+00	2.398D+00	1.652D+00	1.711D+00	1.697D+00
2.000D-02	5.122D+00	4.358D+00	3.869D+00	2.597D+00	1.675D+00	1.746D+00	1.736D+00
2.100D-02	5.561D+00	4.740D+00	4.207D+00	2.807D+00	1.690D+00	1.774D+00	1.769D+00
2.200D-02	6.010D+00	5.136D+00	4.560D+00	3.027D+00	1.697D+00	1.794D+00	1.795D+00
2.300D-02	6.469D+00	5.544D+00	4.926D+00	3.258D+00	1.697D+00	1.807D+00	1.815D+00
2.400D-02	6.933D+00	5.962D+00	5.302D+00	3.499D+00	1.690D+00	1.813D+00	1.827D+00
2.500D-02	7.401D+00	6.387D+00	5.688D+00	3.750D+00	1.677D+00	1.812D+00	1.833D+00

Table A-1 - continued

$r_{\max}(\mu\text{m})$	$\tau_1'$	$\tau_2'$	$\tau_3'$	$\tau_4'$	$\chi_{14}$	$\chi_{24}$	$\chi_{34}$
2.600D-02	7.869D+00	6.818D+00	6.082D+00	4.010D+00	1.658D+00	1.804D+00	1.832D+00
2.700D-02	8.337D+00	7.253D+00	6.482D+00	4.279D+00	1.633D+00	1.790D+00	1.826D+00
2.800D-02	8.802D+00	7.689D+00	6.887D+00	4.556D+00	1.605D+00	1.771D+00	1.814D+00
2.900D-02	9.261D+00	8.125D+00	7.295D+00	4.841D+00	1.573D+00	1.747D+00	1.797D+00
3.000D-02	9.715D+00	8.560D+00	7.703D+00	5.133D+00	1.537D+00	1.720D+00	1.776D+00
3.100D-02	1.016D+01	8.991D+00	8.112D+00	5.431D+00	1.500D+00	1.689D+00	1.751D+00
3.200D-02	1.059D+01	9.417D+00	8.519D+00	5.734D+00	1.461D+00	1.655D+00	1.723D+00
3.300D-02	1.102D+01	9.838D+00	8.923D+00	6.041D+00	1.420D+00	1.619D+00	1.692D+00
3.400D-02	1.143D+01	1.025D+01	9.324D+00	6.352D+00	1.379D+00	1.581D+00	1.659D+00
3.500D-02	1.184D+01	1.065D+01	9.719D+00	6.666D+00	1.337D+00	1.542D+00	1.624D+00
3.600D-02	1.223D+01	1.105D+01	1.010D+01	6.982D+00	1.295D+00	1.502D+00	1.588D+00
3.700D-02	1.261D+01	1.144D+01	1.049D+01	7.299D+00	1.253D+00	1.462D+00	1.551D+00
3.800D-02	1.297D+01	1.182D+01	1.086D+01	7.617D+00	1.212D+00	1.421D+00	1.513D+00
3.900D-02	1.332D+01	1.218D+01	1.123D+01	7.935D+00	1.171D+00	1.380D+00	1.475D+00
4.000D-02	1.366D+01	1.254D+01	1.159D+01	8.252D+00	1.130D+00	1.340D+00	1.436D+00
4.100D-02	1.399D+01	1.289D+01	1.194D+01	8.568D+00	1.091D+00	1.299D+00	1.398D+00
4.200D-02	1.430D+01	1.322D+01	1.228D+01	8.882D+00	1.052D+00	1.259D+00	1.359D+00
4.300D-02	1.461D+01	1.354D+01	1.261D+01	9.193D+00	1.015D+00	1.220D+00	1.321D+00
4.400D-02	1.489D+01	1.386D+01	1.294D+01	9.502D+00	9.786D-01	1.181D+00	1.283D+00
4.500D-02	1.517D+01	1.416D+01	1.325D+01	9.807D+00	9.430D-01	1.144D+00	1.246D+00
4.600D-02	1.543D+01	1.445D+01	1.355D+01	1.010D+01	9.085D-01	1.107D+00	1.209D+00
4.700D-02	1.569D+01	1.473D+01	1.385D+01	1.040D+01	8.750D-01	1.070D+00	1.173D+00
4.800D-02	1.593D+01	1.499D+01	1.413D+01	1.069D+01	8.426D-01	1.035D+00	1.138D+00
4.900D-02	1.616D+01	1.525D+01	1.440D+01	1.098D+01	8.112D-01	1.001D+00	1.103D+00
5.000D-02	1.637D+01	1.550D+01	1.467D+01	1.127D+01	7.808D-01	9.676D-01	1.069D+00



Table A-1 - continued

$r_{\max}(\mu\text{m})$	$\tau_1'$	$\tau_2'$	$\tau_3'$	$\tau_4'$	$X_{14}$	$X_{24}$	$X_{34}$
5.100D-02	1.658D+01	1.574D+01	1.492D+01	1.154D+01	7.515D-01	9.351D-01	1.036D+00
5.200D-02	1.678D+01	1.596D+01	1.517D+01	1.182D+01	7.232D-01	9.034D-01	1.004D+00
5.300D-02	1.697D+01	1.618D+01	1.540D+01	1.208D+01	6.958D-01	8.726D-01	9.729D-01
5.400D-02	1.715D+01	1.639D+01	1.563D+01	1.235D+01	6.694D-01	8.427D-01	9.421D-01
5.500D-02	1.731D+01	1.658D+01	1.584D+01	1.260D+01	6.438D-01	8.137D-01	9.121D-01
5.600D-02	1.747D+01	1.677D+01	1.605D+01	1.285D+01	6.192D-01	7.856D-01	8.829D-01
5.700D-02	1.763D+01	1.695D+01	1.625D+01	1.310D+01	5.954D-01	7.583D-01	8.545D-01
5.800D-02	1.777D+01	1.713D+01	1.645D+01	1.334D+01	5.725D-01	7.318D-01	8.268D-01
5.900D-02	1.790D+01	1.729D+01	1.663D+01	1.357D+01	5.503D-01	7.061D-01	7.999D-01
6.000D-02	1.803D+01	1.744D+01	1.681D+01	1.380D+01	5.289D-01	6.812D-01	7.737D-01
6.100D-02	1.815D+01	1.759D+01	1.697D+01	1.402D+01	5.083D-01	6.571D-01	7.482D-01
6.200D-02	1.827D+01	1.773D+01	1.714D+01	1.423D+01	4.884D-01	6.337D-01	7.234D-01
6.300D-02	1.837D+01	1.787D+01	1.729D+01	1.444D+01	4.692D-01	6.110D-01	6.993D-01
6.400D-02	1.848D+01	1.799D+01	1.744D+01	1.464D+01	4.506D-01	5.890D-01	6.758D-01
6.500D-02	1.857D+01	1.811D+01	1.758D+01	1.484D+01	4.327D-01	5.677D-01	6.531D-01
7.000D-02	1.896D+01	1.862D+01	1.818D+01	1.575D+01	3.520D-01	4.706D-01	5.485D-01
7.500D-02	1.924D+01	1.900D+01	1.865D+01	1.652D+01	2.841D-01	3.876D-01	4.579D-01
8.000D-02	1.943D+01	1.928D+01	1.901D+01	1.717D+01	2.269D-01	3.165D-01	3.793D-01
9.000D-02	1.962D+01	1.960D+01	1.946D+01	1.817D+01	1.377D-01	2.033D-01	2.522D-01
1.000D-01	1.964D+01	1.971D+01	1.967D+01	1.883D+01	7.377D-02	1.200D-01	1.569D-01
1.100D-01	1.957D+01	1.970D+01	1.972D+01	1.926D+01	2.779D-02	5.883D-02	8.560D-02
1.200D-01	1.944D+01	1.961D+01	1.968D+01	1.950D+01	-5.227D-03	1.392D-02	3.239D-02
1.300D-01	1.929D+01	1.948D+01	1.958D+01	1.962D+01	-2.883D-02	-1.885D-02	-7.069D-03
1.400D-01	1.913D+01	1.933D+01	1.945D+01	1.965D+01	-4.559D-02	-4.261D-02	-3.613D-02
1.500D-01	1.898D+01	1.917D+01	1.931D+01	1.963D+01	-5.735D-02	-5.968D-02	-5.734D-02

Table A-1 - continued

$r_{\max}(\mu\text{m})$	$\tau_1'$	$\tau_2'$	$\tau_3'$	$\tau_4'$	$X_{14}$	$X_{24}$	$X_{34}$
1.600D-01	1.882D+01	1.902D+01	1.916D+01	1.956D+01	-6.546D-02	-7.177D-02	-7.265D-02
1.700D-01	1.867D+01	1.887D+01	1.901D+01	1.947D+01	-7.090D-02	-8.017D-02	-8.352D-02
1.800D-01	1.853D+01	1.872D+01	1.887D+01	1.937D+01	-7.442D-02	-8.586D-02	-9.108D-02
1.900D-01	1.840D+01	1.858D+01	1.873D+01	1.925D+01	-7.652D-02	-8.955D-02	-9.617D-02
2.000D-01	1.827D+01	1.845D+01	1.860D+01	1.913D+01	-7.762D-02	-9.177D-02	-9.943D-02
2.500D-01	1.775D+01	1.791D+01	1.804D+01	1.857D+01	-7.566D-02	-9.171D-02	-1.014D-01
3.000D-01	1.737D+01	1.750D+01	1.762D+01	1.810D+01	-7.018D-02	-8.579D-02	-9.552D-02
4.000D-01	1.683D+01	1.694D+01	1.703D+01	1.744D+01	-6.048D-02	-7.434D-02	-8.305D-02
5.000D-01	1.646D+01	1.656D+01	1.664D+01	1.699D+01	-5.364D-02	-6.608D-02	-7.388D-02
6.000D-01	1.620D+01	1.628D+01	1.636D+01	1.667D+01	-4.866D-02	-6.001D-02	-6.713D-02
7.000D-01	1.600D+01	1.607D+01	1.614D+01	1.643D+01	-4.485D-02	-5.534D-02	-6.191D-02
8.000D-01	1.584D+01	1.590D+01	1.597D+01	1.623D+01	-4.191D-02	-5.167D-02	-5.778D-02
9.000D-01	1.570D+01	1.577D+01	1.582D+01	1.607D+01	-3.978D-02	-4.889D-02	-5.456D-02
1.000D+00	1.558D+01	1.565D+01	1.570D+01	1.594D+01	-3.850D-02	-4.703D-02	-5.227D-02
1.000D+01	3.249D-01	4.242D-01	5.266D-01	1.165D+00	-1.242D+00	-1.639D+00	-1.945D+00

## Appendix B: ERROR ANALYSIS

A detailed error analysis of the multiwavelength laser transmission technique has been given by Bard [17]. In the pool fire experiments by Bard and Pagni [15-19], the fluctuations in the width of the fire introduced more experimental error in the pathlength measurement. In this study, the width of the flame and thus the beam pathlength, do not change significantly with time. The error analysis by Bard showed that a 10% uncertainty in  $n$  or  $nk$  gives a 10% uncertainty in the soot volume fraction,  $f_v$ . In addition, the uncertainty of  $f_v$  and  $r_{\max}$  depends on the accuracy of the measured intensities and pathlengths.

The fractional uncertainty in a quantity  $S = F(x_1, x_2, \dots, x_n)$  is given by

$$\left(\frac{\Delta S}{S}\right)^2 = \left(\frac{\partial F}{\partial x_1} \frac{\Delta x_1}{S}\right)^2 + \left(\frac{\partial F}{\partial x_2} \frac{\Delta x_2}{S}\right)^2 + \dots + \left(\frac{\partial F}{\partial x_n} \frac{\Delta x_n}{S}\right)^2 \quad (\text{B-1})$$

Application of equation (B-1) to equations (2-1) and (A-6) gives the fractional uncertainties in  $\tau$  and  $\tau_{ij}$  as

$$\Delta\tau/\tau = [(\Delta I/I \ln(I/I_o))^2 + (\Delta I_o/I_o \ln(I/I_o))^2 + (\Delta L/L)^2]^{1/2} \quad (\text{B-2})$$

$$\begin{aligned} \Delta\tau_{ij}/\tau_{ij} = & [(\Delta I_i/I_i \ln(I/I_o)_i)^2 + (\Delta I_j/I_j \ln(I/I_o)_j)^2 \\ & + (\Delta I_{oi}/I_{oi} \ln(I/I_o)_i)^2 + (\Delta I_{oj}/I_{oj} \ln(I/I_o)_j)^2]^{1/2} \end{aligned} \quad (\text{B-3})$$

where  $\tau_{ij} = \tau_i/\tau_j$ . Equations (B-2) and (B-3) show that the uncertainty in the experimental extinction coefficients decreases as the

transmission,  $I/I_0$ , decreases. With the estimates of  $(\Delta L/L) = 0.05$  and  $(\Delta I/I) = 0.02$ , the fraction uncertainties of  $\tau$  and  $\tau_{ij}$  are below 0.15, if  $I/I_0 < 0.75$ . The widths of the wicks and fuel samples are chosen so that  $I/I_0$  is always less than 0.75.

The detailed error analysis by Bard [17] is applied to estimate the uncertainties of  $f_v$ ,  $r_{\max}$ , and  $N_0$ . An upper limit of the fractional uncertainties of  $\tau$  and  $\tau_{ij}$  is estimated as 0.15. The resulting uncertainties for  $f_v$  and  $r_{\max}$  are below  $\pm 15\%$ , while the uncertainty of  $N_0$  is below  $\pm 50\%$ . These error estimates are conservative and represent upper limits.

## Appendix C: Fuel Properties

The fuel properties given in Table C-1 are taken or calculated from properties listed in Perry [59], Obert [60], and Varafitik [61] for all liquid fuels, and from properties listed by Tewarson [62,63] for PMMA. The surface temperature of PMMA is based on data given by Krishnamurthy and Williams [64]. An average specific heat is chosen,  $c_p = 1.3 \text{ J/gm-K}$ , to give approximately the adiabatic flame temperature for all fuels used if radiation is neglected. The product  $\rho\mu$  must be specified in order to compare theoretical surface pyrolysis rates with experiments. The value  $\rho\mu = 2.0 \times 10^{-3} \text{ kg}^2/\text{m}^4\text{-s}^2$  is chosen to obtain agreement between theory and experiment at  $x = 10 \text{ cm}$  for PMMA in free flow as shown in Fig. 4-10. From the data presented in Figs. 2-7 and 3-9, soot volume fraction at the edge of the soot region near the flame zone is about  $3 \times 10^{-7}$  for PMMA at  $Y_{\text{ox},\infty} = 0.23$  for both forced and free flow. For a soot emission temperature of 1700 K, one half of the total emissive power lies below  $2.4 \mu\text{m}$  in Planck's distribution. The optical properties of soot from Lee and Tien [48] at this wavelength are  $n = 2.090$  and  $k = 1.103$ . With these values, a calculation of the absorption coefficient in equation (4-36) gives  $\kappa = 0.9 \text{ m}^{-1}$ , which is used in the calculations shown in Figs. 4-10 and 4-11.

Table C-1. Summary of Fuel Properties.

Fuel	s	$\Delta H_c$ (kJ/gm)	$Q_p$ (kJ/gmO <sub>2</sub> )	T <sub>w</sub> K	$\Delta H_{vap}$ (kJ/gm)	$c_{p\ell}$ (J/gmK)	L* (kJ/gm)	Y <sub>ox,∞</sub>	B	r <sub>p</sub>	D <sub>c</sub>
Toluene (C <sub>7</sub> H <sub>8</sub> )	0.319	41.0	13.1	384	0.364	1.82	0.530	0.23	5.5	0.088	26
Cyclohexene (C <sub>6</sub> H <sub>10</sub> )	0.301	43.0	12.9	356	0.376	1.85	0.493	0.23	5.9	0.082	36
Cyclohexane (C <sub>6</sub> H <sub>12</sub> )	0.292	43.9	12.8	354	0.360	1.85	0.473	0.23	6.1	0.079	37
Iso-octane (C <sub>8</sub> H <sub>18</sub> )	0.285	44.6	12.7	373	0.287	2.05	0.451	0.23	6.3	0.077	28
n-Heptane (C <sub>7</sub> H <sub>16</sub> )	0.284	45.0	12.8	372	0.317	2.40	0.507	0.23	5.6	0.078	29
Polymethyl- methacryl- ate (C <sub>5</sub> H <sub>8</sub> O <sub>2</sub> ) n	0.521	25.2	13.1	660			1.63	0.23	1.6	0.21	6.3
								0.50	3.7	0.36	14

\*L =  $\Delta H_{vap} + c_{p\ell}(T_w - T_\infty)$  for liquid fuels.

## FIGURE CAPTIONS

- 1-1 Schematic diagram of a steady, two dimensional, laminar, combusting, boundary layer on a pyrolyzing fuel slab.
- 2-1 Schematic diagram of apparatus for simultaneous multiwavelength laser transmission measurements.
- $L\lambda_i, L\lambda_j$  - Laser at  $\lambda_i$  or  $\lambda_j$   
 M - Mirror  
 B - Beamsplitter  
 P - Prism  
 FL1 - Focusing lens 1 ( $f = 550$  mm)  
 FL2 - Focusing lens 2 ( $f = 250$  mm)  
 FL3 - Focusing lens 3 ( $f = 200$  mm)  
 FL4 - Focusing lens 4 ( $f = 78$  mm)  
 F - Bandpass filter (bandwidth = 30 Å)  
 DT  $\lambda_i, DT \lambda_j$  - Detector for transmitted intensity  
 DR  $\lambda_i, DR \lambda_j$  - Detector for reference intensity  
 OS - Output signal to amplifier and computer
- 2-2 Soot volume fraction,  $f_v$ , as a function of distance from the fuel surface at a height of 40 mm in free flow for five liquid, hydrocarbon fuels and PMMA.
- 2-3 Soot volume fraction,  $f_v$ , as a function of distance from fuel surface at different heights for n-heptane in free flow. Wavelength pair numbers refer to  $\lambda_i$ . ( $\lambda_1 = 0.4579$   $\mu\text{m}$ ,  $\lambda_2 = 0.4880$   $\mu\text{m}$ ,  $\lambda_3 = 0.5145$   $\mu\text{m}$ ,  $\lambda_4 = 0.6328$   $\mu\text{m}$ ).

Symbol	x (mm)	Wavelength Pair
$\Delta$	20	1-4
$\square$	20	2-4
$\nabla$	40	1-4
$\diamond$	40	2-4
$\heartsuit$	100	1-4
$\blacklozenge$	100	2-4
$\blacktriangle$	100	3-4

- 2-4 Soot volume fraction,  $f_v$ , as a function of distance from the fuel surface at different heights for cyclohexane in free flow. The symbol definitions are those given in the caption to Fig. 2-3.
- 2-5 Soot volume fraction,  $f_v$ , as a function of distance from the fuel surface at different heights for cyclohexene in free flow. The symbol definitions are those given in caption to Fig. 2-3.
- 2-6 Soot volume fraction,  $f_v$ , as a function of distance from the fuel surface at  $x = 2$  cm for toluene. The symbol definitions are those given in the caption of Fig. 2-3.

- 2-7 Soot volume fractions,  $f_v$ , for PMMA as a function of distance from the fuel surface in free flow. The symbol definitions are those given in the caption to Fig. 2-3.
- 2-8 Most probable radius,  $r_{max}$ , as a function of distance from the fuel surface and streamwise position for cyclohexene. The symbol definitions are those given in the caption to Fig. 2-3.
- 2-9 Total particle concentration,  $N_0$ , as a function of distance from the fuel surface and downstream position for cyclohexene in free flow. The symbol definitions are those given in the caption of Fig. 2-3.
- 3-1 Schematic diagram of wind tunnel and optical equipment for simultaneous multiwavelength laser transmission measurements.
- |                               |                                       |
|-------------------------------|---------------------------------------|
| L $\lambda_i$ , L $\lambda_j$ | - Laser at $\lambda_i$ or $\lambda_j$ |
| M                             | - Mirror                              |
| B                             | - Beamsplitter                        |
| P                             | - Prism                               |
| FL1                           | - Focusing lens 1 (f = 550 mm)        |
| FL2                           | - Focusing lens 2 (f = 250 mm)        |
| FL3                           | - Focusing lens 3 (f = 200 mm)        |
| FL4                           | - Focusing lens 4 (f = 78 mm)         |
| F                             | - Bandpass filter (bandwidth = 30 Å)  |
| D $\lambda_i$ , D $\lambda_j$ | - Detector for transmitted intensity  |
| CFN                           | - Critical flow nozzle                |
| TC                            | - Thermocouple                        |
- 3-2 Contraction shape.
- 3-3 Soot volume fraction,  $f_v$ , as a function of distance from fuel surface at a height of 4 cm for five liquid, hydrocarbon fuels and PMMA in forced flow.
- 3-4 Soot volume fraction,  $f_v$ , as a function of distance from fuel surface at different downstream positions for cyclohexene in forced flow. The symbol definitions are those given in the caption to Fig. 2-3.
- 3-5 Most probable particle radius,  $r_{max}$ , as a function of distance from the fuel surface and downstream position for cyclohexene at  $Y_{Ox,\infty} = 0.23$ . The symbol definitions are those given in caption to Fig. 2-3.
- 3-6 Total particle concentration,  $N_0$ , as a function of distance from the fuel surface and downstream position for cyclohexene in forced flow at  $Y_{Ox,\infty} = 0.23$ . The symbol definitions are those given in the caption to Fig. 2-3.



3-7 Soot volume fraction,  $f_v$ , as a function of distance from the fuel surface at different oxygen mass fractions for n-heptane.

Symbol	$Y_{Ox,\infty}$
■	0.23
▲	0.25
◆	0.35
▼	0.50

3-8 Soot volume fraction,  $f_v$ , as a function of distance from the fuel surface at different oxygen mass fractions for cyclohexene,  $x = 10$  cm. The symbol definitions are those given in the caption to Fig. 3-7.

3-9 Soot volume fraction,  $f_v$ , as a function of distance from the fuel surface at different oxygen mass fractions for PMMA. The symbol definitions are those given in the caption to Fig. 3-7.

3-10 Soot volume fraction,  $f_v$ , as a function of distance from the fuel surface at different free stream velocities for n-heptane at  $x = 4$  cm and  $Y_{Ox,\infty} = 0.35$ .

4-1 Variation of surface values with intensity of the external radiative flux in forced flow, for  $B = 1.0$ ,  $r_p = 0.1$ ,  $D_c = 5.0$ ,  $\theta_w = 2.0$ ,  $N_R = 0.01$ ,  $\epsilon_w = 1$ , and  $Pr = 0.73$ .

4-2 Variation of  $J'_\gamma(\xi, 0)$  and  $J_\beta(\xi, 0)$  with intensity of the external radiative flux in forced flow, for  $B = 1.0$ ,  $r_p = 0.1$ ,  $D_c = 5.0$ ,  $\theta_w = 2.0$ ,  $N_R = 0.01$ ,  $\epsilon_w = 1.0$ , and  $Pr = 0.73$ .

4-3 Dependence of temperature profile on the intensity of the external radiative flux in forced flow, for  $B = 1.0$ ,  $r_p = 0.1$ ,  $D_c = 5.0$ ,  $\theta_w = 2.0$ ,  $N_R = 0.01$ ,  $\epsilon_w = 1$ , and  $Pr = 0.73$ .

4-4 Variation of surface values with  $D_c$  in forced flow, for  $B = 1.0$ ,  $r_p = 0.1$ ,  $\theta_w = 2.0$ ,  $N_R = 0.01$ ,  $\theta_{ex} = 1.0$ ,  $\epsilon_w = 1$ , and  $Pr = 0.73$ .

4-5 Variation of surface values with  $N_R$  in forced flow, for  $B = 1.0$ ,  $r_p = 0.1$ ,  $D_c = 5.0$ ,  $\theta_w = 2.0$ ,  $\theta_{ex} = 1.0$ ,  $\epsilon_w = 1$ , and  $Pr = 0.73$ .

4-6 Excess fraction of total pyrolyzate in forced flow, for  $B = 1.0$ ,  $D_c = 5.0$ ,  $\theta_w = 2.0$ ,  $\theta_{ex} = 1.0$ ,  $\epsilon_w = 1$ , and  $Pr = 0.73$ .

4-7 Variation of surface values with  $D_c$  for free flow, for  $B = 1.0$ ,  $r_p = 0.1$ ,  $N_R = 0.01$ ,  $\theta_w = 2.0$ ,  $\theta_{ex} = 1.0$ ,  $\epsilon_w = 1$ , and  $Pr = 0.73$ .

- 4-8 Variation of surface values with  $N_R$  in free flow, for  $B = 1.0$ ,  $r_p = 0.1$ ,  $D_c = 5.0$ ,  $\theta_w = 2.0$ ,  $\theta_{ex} = 1.0$ ,  $\epsilon_w = 1$ , and  $Pr = 0.73$  .
- 4-9 Excess fraction of total pyrolyzate in free flow, for  $B = 1.0$ ,  $D_c = 5.0$ ,  $\theta_w = 2.0$ ,  $\theta_{ex} = 1.0$ ,  $\epsilon_w = 1$ , and  $Pr = 0.73$  .
- 4-10 Experimental and theoretical local mass flux rates for a pyrolyzing slab of PMMA in free flow,  $Y_{Ox,\infty} = 0.23$  .
- 4-11 Experimental and theoretical local mass flux rates for a pyrolyzing slab of PMMA in forced flow with  $Y_{Ox,\infty} = 0.23$  .
- 4-12 Experimental and theoretical local mass flux rates for a pyrolyzing slab of PMMA in forced flow with  $Y_{Ox,\infty} = 0.50$  .

This report was done with support from the Department of Energy. Any conclusions or opinions expressed in this report represent solely those of the author(s) and not necessarily those of The Regents of the University of California, the Lawrence Berkeley Laboratory or the Department of Energy.

Reference to a company or product name does not imply approval or recommendation of the product by the University of California or the U.S. Department of Energy to the exclusion of others that may be suitable.

TECHNICAL INFORMATION DEPARTMENT  
LAWRENCE BERKELEY LABORATORY  
UNIVERSITY OF CALIFORNIA  
BERKELEY, CALIFORNIA 94720